PONTIFICIA UNIVERSIDAD CATÓLICA DEL PERÚ

FACULTAD DE CIENCIAS E INGENIERÍA

CHARACTERIZATION OF ZEOLITE MINERALS IN THE FALCHANI LITHIUM PROJECT, MACUSANI VOLCANIC FIELD, PUNO, PERU

Tesis para obtener el título profesional de Ingeniera Geóloga

AUTORA:

FIORELA LIZBETH MAXI CASA

ASESOR:

DR. LISARD TORRÓ I ABAT

Lima, Octubre, 2025

INFORME DE SIMILITUD

Yo, Lisard Torró i Abat,

docente de la Facultad de Ciencias e Ingeniería de la Pontificia Universidad Católica del Perú,

asesor de la tesis titulada "*Characterization of Zeolite Minerals in The Falchani Lithium Project, Macusani Volcanic Field, Puno, Peru*",

de la autora Fiorela Lizbeth Maxi Casa

dejo constancia de lo siguiente:

- El mencionado documento tiene un índice de puntuación de similitud de 18 %. Así lo consigna el reporte de similitud emitido por el software *Turnitin* el 31/10/2025.
- He revisado con detalle dicho reporte y la Tesis y no se advierten indicios de plagio.
- Las citas a otros autores y sus respectivas referencias cumplen con las pautas académicas.

Lugar y fecha: Lima a 31 de octubre de 2025

Apellidos y nombre del asesor: Torró i Abat, Lisard	
CE: 001833851	Firma 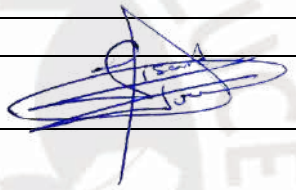
ORCID: 0000-0002-3557-8334	

ACKNOWLEDGMENTS

I dedicate this work to my family, especially my parents, Ana María and Marcelino, and my brothers, José Carlos and Ángel Gabriel. Their unconditional support, constant encouragement, and unwavering belief in me have been essential pillars that have motivated me to persevere at every stage of this journey.

A special acknowledgment goes to Dr. Lisard Torró, a distinguished professor at PUCP and my advisor, who has been a constant source of trust, patience, and motivation. His invaluable guidance and contributions throughout this process have been crucial, helping me navigate challenges and celebrate my achievements.

I would also like to express my gratitude to Macusani Yellowcake – American Lithium for their invaluable support in facilitating our visit to the study area. Special thanks go to Dr. Ulises Solís, as well as geologists Miguel Cavani and Henry Mamani, for their assistance and collaboration. Additionally, I am thankful to Johan Ramirez for his active participation and contributions during the field campaign.

I sincerely appreciate the dedication of the technical specialists responsible for the preparation and analysis of the samples, especially Pablo Valverde (PUCP), as well as Dr. Cristina Villanova (University of Barcelona) and Dr. Joaquín A. Proenza (University of Barcelona) for fruitful discussion of the results. Constructive comments from Dr. Cesar Muñoz and Dr. Diego Benites are much appreciated and helped improve the quality of this thesis.

Finally, I am deeply grateful to my friends, Leidi Condori and Ivana Cárcamo, for their invaluable support and bringing joy to my days.

This study was economically supported by the projects 122-2020 E041-2020-01-01 and PE501087814-2024 granted by the Peruvian research agency PROCIENCIA.

RESUMEN

El depósito volcanogénico de Li de Falchani en Perú alberga recursos significativos de Li y Cs. Investigaciones previas identificaron zeolitas en las unidades mineralizadas. Esta tesis documenta la mineralogía de muestras ricas en zeolitas de Falchani y discute las condiciones fisicoquímicas de su formación y su potencial económico según su contenido en Li y Cs.

Los análisis de DRX identificaron un ensamble mineralógico compuesto por fases primarias (feldespato, mica, cuarzo) y secundarias (arcillas, zeolitas, sílice amorfa). Las muestras se clasifican en cinco tipos según su paragénesis de alteración dominante: i) zeolita, ii) zeolita + esmectita/arcillas interestratificadas, iii) zeolia + esmectita/arcillas interestratificadas + caolinita, iv) esmectita/arcillas interestratificadas dominante, y v) caolinita dominante.

La mordenita y la mutinaita son las zeolitas predominantes, mientras que la clinoptilolita y la heulandita son minoritarias. Las zeolitas forman agregados radiales de cristales aciculares en amígdalas, vetillas y espacios intersticiales dentro de una matriz hipocristalina brechada, así como esferulitas y localmente cristales idiomorfos. Estas características sugieren un origen autigénico durante la alteración del vidrio riolítico en condiciones de pH alto y actividad de sílice elevada.

Las muestras ricas en zeolitas presentan altos contenidos de Li (hasta 4,700 ppm; mediana 2,300 ppm) y Cs (hasta 9,600 ppm; mediana 6,600 ppm). Su enriquecimiento en Cs es diferencial con respecto al resto de tipos mineralógicos, lo que sugiere que las zeolitas jugaron un papel clave en el enriquecimiento de este metal. En cambio, los contenidos de Li son muy similares, estadísticamente, entre las muestras pertenecientes a todos los tipos mineralógicos. Si bien esto resalta que las muestras ricas en zeolitas son atractivas en cuanto a su potencial aporte al volumen de mena, no las identifica claramente como minerales portadores de Li. Se requieren estudios más especializados, como intercambio catiónico, para definir cuál es la expresión mineralógica del Li dentro de las muestras ricas en zeolitas de Falchani.

ABSTRACT

The Falchani volcanogenic Li deposit in Peru hosts significant Li and Cs resources. Previous investigations identified zeolites within the mineralized units. This thesis documents the mineralogy of zeolite-rich samples from Falchani and discusses the physicochemical conditions of their formation and their economic potential based on their Li and Cs contents.

XRD analyses identified a mineral assemblage composed of primary (feldspar, mica, quartz) and secondary (clays, zeolites, amorphous silica) phases. The samples are classified into five types based on their dominant alteration paragenesis: i) zeolite type; ii) zeolite + smectite/mixed-layer clay type; iii) zeolite + smectite/mixed-layer clay + kaolinite subgroup type; iv) smectite/mixed-layer clay dominant type; and v) kaolinite subgroup dominant type.

The predominant zeolites are mordenite and mutinaite, while clinoptilolite and heulandite are minor. Zeolites form radial aggregates of acicular crystals in amygdales, veinlets, and interstitial spaces within a brecciated hypocrystalline matrix, as well as spherulites and local euhedral crystals. These characteristics suggest an authigenic origin during the alteration of rhyolitic glass under high pH and silica activity conditions.

Zeolite-rich samples exhibit high contents of Li (up to 4,700 ppm; median 2,300 ppm) and Cs (up to 9,600 ppm; median 6,600 ppm). Their enrichment in Cs is differential compared to the other mineralogical types, which would suggest that zeolites played a key role in the enrichment of this metal. In contrast, Li contents are statistically very similar among samples belonging to all mineralogical types. While this highlights that zeolite-rich samples are attractive in terms of their potential contribution to the volume of extractable and processable ore, it does not clearly identify zeolites as Li host minerals. More specialized studies, such as cation exchange experiments, are required to define the mineralogical expression of Li within the zeolite-rich samples from Falchani.

Table of Contents

1. INTRODUCTION 1
1.1. Natural zeolites: Characteristics, applications, and their potential for Li and Cs sorption 1
1.2. Lithium and cesium: Economic importance and uses 3
1.3. The Falchani Lithium Project: Discovery, significance, and recent research 7
1.4. Conundrum 9
1.5. Objectives 10
1.6. Hypothesis/hypotheses 11
1.7. Justification 11
2. METHODOLOGY 12
2.1. Sampling 12
2.2. Analytical methods 14
2.2.1. X-ray diffraction (XRD) 14
2.2.2. Optical microscopy 15
3. GEOLOGICAL SETTING 16
3.1. The Central Andes in southern Peru: The Oriental Cordillera 16
3.2. The Macusani Structural Zone 18
3.3. The Macusani Volcanic Field 21
3.4. The Falchani Lithium Project 24
4. RESULTS 26
4.1. Macroscopic description of the samples 26
4.2. Mineralogy 29
4.3. Textures 33
5. DISCUSSION 35
5.1. Crystallochemistry of zeolites in the Falchani Lithium Project 35
5.2. Genesis of zeolites in the Macusani Volcanic Field 35
5.3. Economic potential of zeolite minerals in the Falchani Lithium Project 42
6. CONCLUSIONS 43
7. REFERENCES 44
APPENDICES

List of figures

Figure 1. Location of the Falchani Lithium Project, which covers an area of 1,700 ha, in the Macusani Volcanic Field (GEOCATMIN 2024). 9

Figure 2. Sampling of drill cores. **A)** Aspect of drill cores from the Falchani Lithium Project from which samples were collected. **B)** The samples were stored in labelled plastic bags. 13

Figure 3. Location of the surface sample (2021-MAC-26) and of the collars of drill cores from which the remaining 25 samples were collected within the Falchani Lithium Project, which is owned by Macusani Yellowcake S.A.C. (GEOCATMIN 2024). 13

Figure 4. Manual sample preparation for XRD analysis. **A)** Agate mortar and pestle used to prepare rock powder. **B)** Labelled plastic vials with the powdered samples..... 15

Figure 5. Geomorphotectonic units of the Central Andes, highlighting the location of the study area within the Eastern Cordillera. Modified from Kontak et al. (1990). 16

Figure 6. Geological map of the Macusani Volcanic Field, modified from Pichavant et al. (1988), Sandeman et al. (1998), and Kontak et al. (1990). 22

Figure 7. Aspect of representative hand samples. **A)** Fine-grained clayey material. **B)** Highly altered material with a light brown patina on the right surface edge; the sample is soft to the tact, and easy to be disintegrated. **C)** Whitish clayey material, a little rough to the tact, with a conspicuous dark brown patina all over its upper face. **D)** White, consolidated rock, with a smooth surface and containing small lithic fragments and dark mica randomly distributed within the clayey matrix. **E)** White, fine-grained sample with scattered dark brown subhedral dark mica crystal clasts (arrow). **F-G)** Massive, hard clay-rich material with a light brown coating over most of its surface, which contrasts with the white color of the freshly-cut rock sample. **H)** Anastomosed light and dark banding. **I)** Laminar to anastomosed alternating white and brownish-grayish layers bands; the brownish-gray bands are discontinuous with internal brecciated texture. **J)** Banded rock with intercalation of levels rich in translucent to gray glass clasts defining a blocky texture. **K)** Very fine-grained gray material with a pinkish stain in sharp contact with a very fine-grained white host rock; acute triangle terminations of the gray material might indicate unidirectional solidification textures. **L)** Brecciated texture with rounded to angular and irregular clasts embedded in a very fine-grained dark gray matrix. The clast in the lower central area of the sample is split into three sub-clasts depicting a local jig-saw fit texture..... 28

Figure 8. XRD patterns grouped by dominant alteration mineral paragenesis (see text for details). When available, the Li (ppm) and Cs (ppm) contents, as provided by Macusani Yellowcake for 1.5-m-long segments of drill cores from which the samples were taken, are given. For sample 2021-MAC-026, the Cs content is taken from Ramirez-Briones et al. (2025), while its Li content was not analyzed by these authors in this sample. Abbreviations: clinoptilolite (Cpt), heulandite (Hul), illite-montmorillonite (Ilt-Mnt), kaolinite (Kln), K-feldspar (Kfs), mica (Mca), mordenite (Mor), mutinaite (Mut), opal (Opl) plagioclase (Pl), quartz (Qz), rectorite (Rec), smectite (Sme), tridymite (Trd), and virgilite (Vir). 33

Figure 9. Microphotographs of zeolite-rich samples using plane-polarized (PPL) and crossed-polarized (XPL) transmitted light. **A)** Brecciated texture with rounded to subangular clasts of volcanic glass and a 300 μm-long biotite lath in a fine-grained matrix of silica, clays, and zeolites (zeolite + smectite/mixed-layer clay type). **B)** Perlitic texture in devitrified glass clasts (zeolite + smectite/mixed-layer clay type). **C)** Zeolites as radial aggregates of acicular crystals with lengths of ~300 µm (zeolite type). **D)** Spherulitic aggregates of zeolite (~ 200 µm) in an altered matrix (zeolite + smectite/mixed-layer clay type). **E)** Irregular micro-veins cutting the very fine-grained and altered matrix (zeolite type). **F)** Fine-grained matrix composed of clays, silica, and zeolites

cementing small and irregular clasts of devitrified glass (zeolite type). **G)** Micro-veins filled with subhedral zeolite radial aggregates (zeolite type). **H)** Radial (fan shaped) acicular zeolite crystals filling cavities and interstitial space (zeolite type). **I)** Detail of spherulitic zeolite showing Brewster crosses (zeolite + smectite/mixed-layer clay type). **J**) Vesicle filled with radial zeolite coated with possible clays in a glass matrix (zeolite + smectite/mixed-layer clay type). **K)** Detail of equant (pseudo rhombododecahedral and pseudo trapezohedral) zeolite crystals ~50 μm in size (zeolite type). **L)** Detail of idiomorphic pseudo rhombododecahedral zeolite crystals within cavities in the matrix (zeolite + smectite/mixed-layer clay type). 34

Figure 10. Stability diagrams including zeolites and other authigenic minerals found in the studied samples from the Falchani Lithium Project. **A)** Phase stability diagram for the Si-Al-K-O-H_2O system at 25°C, illustrating the equilibrium conditions of potassium-bearing minerals (microcline, illite/smectite mixed-layer clay, montmorillonite, gibbsite, and kaolinite) as functions of dissolved silica concentration (log a SiO_2(aq)) and potassium-to-hydrogen ion activity ratio (log (aK^+/aH^+)). Modified from Aagaard and Helgeson (1983). **B)** Stability diagram for the Si-Al-Ca-K-Na-H_2O system at 125 °C showing the stability of Ca-zeolites (laumontite, clinoptilolite, and mordenite), as a function of silica activity and the Ca^{2+}/H^+ ratio in solution. Modified from Benning et al. (2000). **C)** Detail of mineral stability fields in the K_2O-Na_2O-CaO-Al_2O_3-SiO_2-H_2O system at 25°C, showing equilibrium phase relations under fixed cation activities (K^+ defined by K-feldspar, Ca^{2+} by tobermorite, and Al^{3+} by kaolinite solubility). Modified from Savage et al. (2007)..... 39

Figure 11. Box-and-whisker plots showcasing Li (ppm) and Cs (ppm) contents for the different mineralogical types. 41

List of Tables

Table 1. Estimation of measured, indicated, and inferred resources as of October 31, 2023. (Loveday and Karstick 2023). 8

Table 2. Minerals identified in samples from the Falchani Lithium Project using XRD including rock forming minerals (Pl: plagioclase, Mca: mica, Qz: quartz, and Kfs: K-feldspar), zeolite group minerals (Mor: mordenite, Mut: mutinaite, Cpt: clinoptilolite, and Hul: heulandite), clay minerals (Kln: kaolinite subgroup minerals, Sme: smectite, mixed-layer clay group minerals (Ilt-Mnt: illite-montmorillonite, Rec: rectorite), and other minerals (Vir: virgilite, Opl: opal, and Trd: tridymite). 31

1. INTRODUCTION

1.1. Natural zeolites: Characteristics, applications, and their potential for Li and Cs sorption

Zeolites are aluminosilicate minerals of the tectosilicate group characterized by being microporous and hydrated (Hey 1930). They have relatively low densities (~2.0-2.3 g/cm^3) and moderate hardness (~3.5-5.5 on the Mohs scale). Zeolites can exhibit prismatic, acicular (e.g., natrolite), tabular (e.g., heulandite, stilbite), or equidimensional (e.g., chabazite) habits depending on their structural arrangement (Klein et al. 1982). They possess a unique three-dimensional structure, formed by tetrahedra of silicon (SiO_4) and aluminum (AlO_4) oxides linked together by shared oxygen vertices (Smith 1984; Coombs et al. 1998; Hay 1978), that creates an open crystalline network with molecular-size channels and cavities in the range of ~3.5-8 Å (Flanigen 1991). These channels and cavities act as molecular sieves, allowing the selective passage of small molecules.

The isomorphic substitution of Si^{4+} by Al^{3+} in the structure of zeolites generates a charge defect that is compensated by the presence of alkaline and alkaline-earth cations, such as Na^+, K^+, Ca^{2+}, and Mg^{2+}, which become trapped in the channels and cavities (Hey 1930). This configuration provides them with a high cation exchange capacity (Pabalan and Bertetti 2001). Another distinctive characteristic is their reversible dehydration capability, which allows them to lose and regain water molecules without collapsing their porous crystalline structure (Armbruster and Gunter 2001).

In general terms, natural zeolites follow the chemical formula:

$$(Li, Na, K)_p\,(Mg, Ca, Sr, Ba)_q\,[Al_{(p+2q)}\,Si_{n-(p+2q)}\,O_{2n}]\,.\,mH_2O$$

Where “p” and “q” are the numbers of monovalent and divalent ions, respectively, “n” is half the number of oxygen atoms, and “m” is the number of water molecules (Singh and

Kolay 2002). In this formula, group IA and IIA cations compensate for the negative charge resulting from the substitution of Si by Al.

Thanks to their unique structural and compositional properties, zeolites have numerous applications as adsorbents, catalysts, and ion exchangers in various industrial processes (Giannetto et al. 2000). These applications include their use as adsorbents in separation processes (Inglezakis et al. 2023), purification of industrial gases (Hernandez et al. 2015), and in lithium-ion batteries (Nunes-Pereira et al. 2012 and references therein). They act as catalysts in numerous petrochemical industry processes (Corma 2003). As ion exchangers, they are used in the softening of industrial and domestic waters (e.g., removal of Ca^{2+} and Mg^{2+}; Giannetto et al. 2000), removal of heavy metals in industrial effluents (e.g., Cu^{2+}, Ni^{2+}, Co^{2+}, and Fe^{2+}; Belova 2019), and the treatment of radioactive wastes (e.g., Cs^{+}; Johan et al. 2015; Jiménez-Reyes et al. 2021). Additionally, they are used in medicine (e.g., for gastrointestinal issues, dental problems, protection against radionuclides, among others), agriculture (e.g., as a fertilizer supplement), livestock feed, and aquaculture (Rocher 1995). Natural zeolite and other materials, such as silica, fly ash, and metakaolin, are used to reduce the cement content in concrete, thereby decreasing its carbon footprint (Shekarchi 2023).

Natural zeolites can exchange ions in their structure with other ions in solution at the cation exchange sites (Sherry 1969; Pabalan and Bertetti 2001). This replacement is controlled by several factors, such as the nature of the cationic species, the size and charge of the cation (anhydrous or hydrated), temperature, ion concentration in solution, solvent, and structural characteristics of the zeolites (Giannetto et al. 2000), all of them subordinated to zeolite composition, since the lower the Si/Al ratio, the higher the exchange capacity (Breck 1974).

The fact that zeolites can adsorb molecules and ions into their pores and surfaces creates a dual screening effect where sodium ions (Na^+) are completely exchanged for lithium ions (Li^+). In contrast, cesium ions (Cs^+) are only partially exchanged (Breck 1974). Studies have reported that natural zeolites, such as mordenite and clinoptilolite, have high selectivity for Cs^+ in aqueous environments (Johan et al. 2015). The pH of the solution influences Cs^+ adsorption. Under acidic conditions, the high concentration of H^+ competes with Cs^+ for negatively charged sites, reducing Cs^+ adsorption. As the pH increases, the negatively charged surface layer in some zeolites becomes enriched in Cs, as the amount and rate of adsorption of this cation gradually increase. However, in ultra-basic environments, with a pH above 8, Cs^+ associates with the OH^- groups present, and the strong alkalinity can deteriorate the zeolite structure, thereby decreasing its adsorption capacity (Ferreira et al. 2021). Conte et al. (2022) found that the sorption of Li in certain types of zeolites, particularly in those with Si/Al molar ratios <1.5, was a fast process and that up to 70 % of the dissolved Li was removed at pH of 10 to 11. However, Li removal was significantly reduced in bimetallic aqueous solution due to competition for the sorption sites between the different cations.

1.2. Lithium and cesium: Economic importance and uses

Lithium is the lightest and least dense solid metal, with an atomic mass of 6.94 amu. It belongs to the alkali metal group. Lithium is a moderately incompatible, highly mobile, lithophile element (Goldschmidt 1954; Brenan et al. 1998; Aral and Vecchio-Sadus 2008). Its concentration varies from 1.39 ppm in the silicate Earth to 5.5 ppm in MORB and 30.5 ppm in the upper continental crust (Sauzéat et al. 2015; Marschall et al. 2017; Pogge von Strandmann et al. 2020). In some granitic rocks found in the upper continental crust, such as rare metal-rich granites and Li-Ta-Cs (LTC) pegmatites, the contents can reach much higher levels (London 2017; Michaud et al. 2021). In contrast, it is much less abundant in

water reservoirs, such as the ocean water, with a mean Li content of 0.18 ppm (Tomascak et al. 2016). The human body contains approximately 7 mg of lithium (Aral and Vecchio-Sadus 2008).

Nowadays, lithium is primarily exploited from granitic pegmatites of the Li-Cs-Ta (LCT) family, which have high lithium contents (~>1 wt% Li_2O) but low tonnage (~10 Mt). The main ore mineral in LCT pegmatites is spodumene (London 2008; Bradley and Jaskula 2014; Grew 2020; Groves et al. 2022). Hydromorphic deposits, specifically salars and geothermal fields, exhibit low lithium grades but high tonnage (Evans 2014; Bowell et al. 2020). Volcanogenic deposits contain lithium in clays such as hectorite and tainiolite within volcanogenic sequences, exhibiting low grades and high tonnages (Benson et al. 2017; Bowell et al. 2020; Putzolu et al. 2025a, b). Industrial lithium compounds include lithium carbonate (Li_2CO_3), lithium chloride (LiCl), lithium bromide (LiBr), and lithium hydroxide ($LiOH \cdot H_2O$; Evans 2014; Bradley et al. 2017b; Bibienne et al. 2020). Lithium carbonate is the dominant compound in the market, and resources are measured in lithium carbonate equivalents (LCEs; Evans 2014; Bradley et al. 2017a).

Lithium has numerous applications in technology and medicine. In battery technology, it functions as the active material in electrolytes and electrodes, facilitating ion transfer during battery charging and discharging cycles. Due to this, lithium-ion batteries are crucial for electronic devices, electric vehicles, and energy storage systems, owing to their high energy capacity and efficiency (Evans 2014; Watari et al. 2020; IEA 2021; Jowitt and McNulty 2021). It is also used in drugs for bipolar disorder and as an essential element in medicine for its anti-suicidal effect (Garrett 2004; Bibienne et al. 2020). Historically, Li was used in nuclear weapons (Bradley et al. 2017a).

Lithium is considered a critical metal by several countries, including the United States (IEA 2023), Canada (Government of Canada 2024), and the European Union (European

Commission 2023). Several factors are associated with the future demand for lithium, primarily related to population growth and the expansion of technologies that require lithium (Bibienne et al. 2020), as well as efforts to combat climate change (Kesler et al. 2012; Watari et al. 2020). According to the International Energy Agency (2021), lithium demand is projected to grow 13 to 51 times between 2020 and 2040. In November 2022, the price had soared to ~$83,500/ton, reflecting a significant upward trajectory for lithium prices driven by the increasing adoption of electric vehicles (Trading Economics 2023). However, lithium carbonate prices in China reached $14,500/ton in January 2024, falling to $9,400/ton in November of the same year. Meanwhile, the USA contract market maintained an annual average of $14,000/ton, representing a 66% decrease from 2023 prices (USGS 2025). In August 2025, the lithium carbonate price was ~$11,772/ton (Trading Economics 2025).

By contrast, cesium is one of the heaviest and most dense solid metals, with an atomic mass of 132.91 amu. It is also part of the alkali metal group. Cesium is highly reactive with water, halogens, air, acids, and bases. Geochemically, Cs is highly incompatible due to its large ionic radius and concentrates in the liquid during magma crystallization (London 2005). Cesium is an ultra-trace element in the silicate Earth (0.021 ppm; McDonough 2003), MORB (0.53 ppm), and bulk continental crust (1 ppm; Hofmann 1988).

The most important cesium deposits are LCT pegmatites (Černý and Ercit 2005), such as Tanco in Canada and Bikita in Zimbabwe (Trueman et al. 2020). Its main ore is pollucite (~30 wt.% Cs_2O; Linnen et al. 2012), a mineral of the zeolite group (Norton 1973). Rare metal granites, such as the Yichun granite in China, may also serve as a source of Cs (Huang et al. 2002; Trueman et al. 2020). Geyserites, i.e., epithermal fluids leaching rhyolites, are another cesium deposit type (Trueman et al. 2020), including Targejia in

China, Taron in Argentina, and Yellowstone in the USA (White et al. 1975; Christiansen 2001). Industrial cesium compounds are the metal itself, formate ($HCOOCs^{+1}$), bromide (CsBr), carbonate (Cs_2CO_3), chloride (CsCl), hydroxide (CsOH), iodide (CsI), nitrate ($CsNO^3$), and sulfate (Cs_2SO_4; USGS 2025).

The primary application of cesium is in the form of cesium formate, a product used in the exploration and production of oil and gas through high-pressure and high-temperature well drilling fluids (Schlumberger Corporation 2002; Cabot Specialty Fluids 2003). Other cesium compounds have industrial applications in spectrophotometers and scintillation counters, medical radioisotopes, organic compound alkylation, energy conversion, battery electrolytes, fluoroscopy and X-ray equipment, phosphors and pyrotechnics, water treatment, and scientific instruments (Butterman et al. 2004). The Time Center of the United States Naval Observatory features a cesium atomic clock with an accuracy of up to 1 second in 1.4 billion years. These clocks are also used in aircraft, satellites, and ground systems that track the space shuttle (Breakiron 2003). The isotope ^{137}Cs plays an important role in agriculture, food sterilization, surgical equipment, and cancer treatment (Jensen 1985; National Safety Council 2003). According to the International Atomic Energy Agency and other reports, radioactive substances, including ^{137}Cs, can be employed in Radiological Dispersion Devices, which are weapons that use conventional explosives to disperse radioactive material (Charbonneau 2003).

Cesium is considered a critical element by Canada (Government of Canada 2024), but not by the United States or the European Union (IEA 2023). Global pollucite reserves are estimated to be less than 200,000 tons, and existing stockpiles could be depleted in a few years. The future demand for this metal is expected to increase due to its multiple uses in industry, technology, and medicine (USGS 2025). Cesium is available in three purity grades: 99%, 99.5%, and 99.9%, with main compounds being chloride and nitrate

(Butterman et al. 2004). In 2024, 1-gram ampules of 99.8% cesium cost $98.00 and 99.98% cesium cost $124, representing increases of 7% and 6% from 2023, respectively. Prices for 50 g of 99.9% cesium compounds ranged from $104 to $173.60, with a 5% to 6% increase. The standard cesium plasma solution was $93.40/50 mL and $142/100 mL, up 4%. Cesium formate 98% was $52.40/25 g, a 6% increase from the previous year (USGS 2025). In August 2025, the price of cesium carbonate is ~$135.14/kg (Shanghai Metals Market 2025).

1.3. The Falchani Lithium Project: Discovery, significance, and recent research

The Falchani Lithium Project is geologically situated in the Macusani Volcanic Field, located in the Eastern Cordillera of the Central Andes (Fig. 1). Geographically, it is situated in the province of Carabaya, ~50 km north of Lake Titicaca, in the Department of Puno, in southeastern Peru. The lithium mineralization in the Falchani Lithium Project was discovered in November 2017. Macusani Yellowcake S.A.C., a subsidiary of the Canadian company American Lithium Corporation, owns this project. Table 1 presents the measured, indicated, and inferred resources of the project as of 2023. The total resources amount to 9.52 Mt LCE (Loveday and Karstick 2023). This figure suggests that the Falchani Lithium Project may become one of the world's largest hard-rock lithium mines.

The lithium ore at the Falchani Lithium Project is distributed among three lithologic units, labeled as Upper Breccia, Lithium-rich Tuff, and Lower Breccia, as described in the technical report by Nupen (2019). These units are described in more detail in the "Geological Setting" section below. A few recent studies on the mineralogy and geochemistry of the Li-ore units have been developed. Segovia-More et al. (2023) and Segovia-More (2024) studied the mineralogy of these units through X-ray Diffraction (XRD), Scanning Electron Microscopy with Energy Dispersive Spectroscopy (SEM-

EDS), and Transmission Electron Microscopy (TEM) and concluded that Li is associated with primary micas and secondary dioctahedral smectites and, potentially, zeolites. Ramírez-Briones et al. (2025) studied the whole rock chemical composition of the Li-ore units and found that some zeolite-dominated samples are rich in Li (up to 5,000 ppm) and Cs (up to 8,993 ppm). Torró et al. (2025) performed a detailed characterization of mica crystal clasts in the Lithium-rich Tuff, comprising cores of zinnwaldite and narrow rims of lepidolite, which yielded $^{40}Ar/^{39}Ar$ plateau dates of ca. 8.9 Ma (see also Sanandres-Flores 2023).

Table 1. Estimation of measured, indicated, and inferred resources as of October 31, 2023. (Loveday and Karstick 2023).

TONNES (Mt)	LITHIUM (ppm)	CESIUM (ppm)	POTASSIUM (wt.%)	RUBIDIUM (ppm)
MEASURED				
69	2,792	631	2.74	1,171
68	2,832	641	2.72	1,194
65	2,915	647	2.71	1,208
61	3,024	616	2.74	1,228
57	3,142	547	2.78	1,250
INDICATED				
378	2,251	1,039	2.92	1,055
357	2,342	1,058	2.90	1,070
327	2,472	1,095	2.87	1,104
310	2,549	1,086	2.86	1,146
288	2,646	1,041	2.88	1,166
INFERRED				
506	1,481	778	3.31	736
443	1,597	837	3.24	762
348	1,785	886	3.18	796
276	1,961	942	3.10	850
201	2,211	1,022	3.01	926

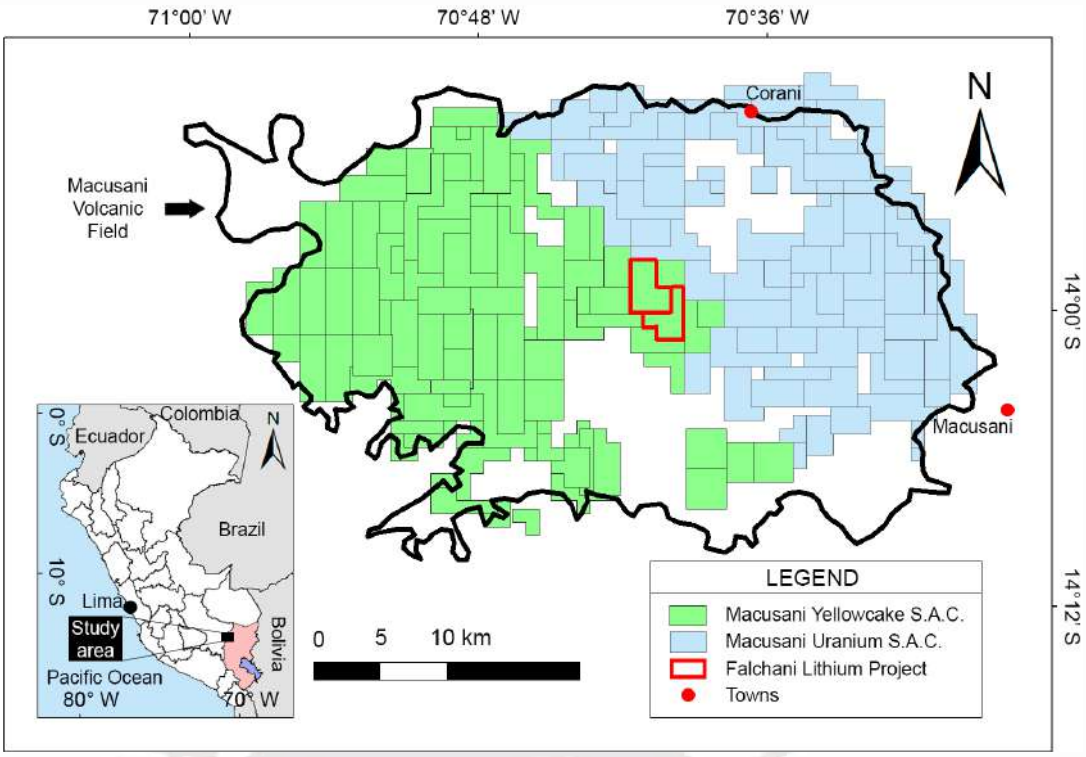

Figure 1. Location of the Falchani Lithium Project, which covers an area of 1,700 ha, in the Macusani Volcanic Field (GEOCATMIN 2024).

1.4. Conundrum

The current demand for lithium and cesium is expected to increase over the following decades. Lithium is considered a critical raw material by the United States (IEA 2023), Canada (Government of Canada 2024), and the European Union (European Commission 2023), and cesium is considered a critical raw material by Canada (Government of Canada 2024). This is largely driven by the energy transition towards electric mobility and the adoption of renewable energy resources to achieve carbon neutrality (Jowitt and McNulty 2021; European Commission 2023). This transition, crucial for combating climate change, has generated increased demand for raw materials of mineral origin and raised concerns over their availability (Lee et al. 2020; Jowitt and McNulty 2021).

In particular, lithium is essential for the production of rechargeable batteries, particularly in electric vehicles. The demand for lithium is projected to grow significantly, with

estimates suggesting a 13– to 51–fold increase between 2020 and 2040 (IEA 2020). Exploration and prospecting for new sources are vital to ensure the future supply of lithium. On the other hand, cesium demand is increasing due to its multiple uses in medicine, industry, and technology, including photoelectric cells and battery storage (Butterman et al. 2004). This underscores the need for further investigation into their primary mineral deposits and their mineralogical expression, which may enhance discovery and optimize metallurgical processes for their benefit (Frenzel et al. 2024).

The study of lithium and cesium deportment in zeolite-rich rocks in volcanogenic deposits presents a significant challenge due to the lack of prior research. The scarcity of studies addressing the presence and characteristics of these zeolites in volcanogenic lithium deposits creates a knowledge gap that limits our understanding and potential exploitation of these resources. Research in this area would not only fill a critical gap in geological literature but also potentially open new opportunities for the exploitation of valuable mineral resources.

1.5. Objectives

Main Objective:

- To study the mineralogy of zeolite-rich samples in lithium-ore units from the Falchani Lithium Project with a particular focus on their Li and Cs uptake.

Specific Objectives:

- To identify the zeolite group minerals that are present in the lithium-ore units and their textural relationship with other mineral phases;
- To constrain the physicochemical conditions under which the zeolites formed and to explore how this may enhance our understanding of the formation conditions of the deposit.

- To assess the economic potential of the zeolite-rich samples, particularly in relation to their contents of lithium and cesium.

1.6. Hypotheses

According to the limited previous research, several zeolite-rich horizons occur in lithium-ore units from the Falchani Lithium Project (Segovia-More et al. 2023; Segovia-More 2024). The zeolite group minerals there are expected to have high lithium and cesium contents (Ramírez-Briones et al. 2025). These elements are likely incorporated in the zeolites as exchangeable cations adsorbed onto their surfaces and cavities (Sherry 1969; Pabalan and Bertetti 2001; Hoyer et al. 2015).

1.7. Justification

Lithium and cesium are essential elements for the energy transition towards a decarbonized economy, and their demand is increasing due to their multiple uses in industry, technology, and medicine (USGS 2025). Therefore, it is important to identify and characterize new primary sources. The Falchani Lithium Project, situated in the Macusani Volcanic Field, of southeastern Peru, presents high contents of both elements.

The technical report and mineral resource estimate (Loveday and Karstick 2023) indicate that the Falchani Lithium Project is one of the most economically significant potential sources of lithium, as well as other elements that may be benefited as by-products (Table 1). However, the mineralogy of the rocks is poorly constrained, particularly with respect to the occurrence of zeolites. The investigation of the mineralogy of zeolite-rich rocks from the volcanogenic Falchani Lithium Project may serve as a model for future volcanogenic lithium discoveries (cf. Benson et al. 2017; Bowell et al. 2020; Putzolu et al. 2025a) in which zeolites are important mineral constituents. The accurate identification of zeolite minerals and their relationship with lithium and cesium during the exploration

stage will be pivotal to optimizing recovery processes through quantitative mineral characterization and spatial variability modeling, thereby reducing uncertainties (Frenzel et al. 2024), and enabling more efficient exploitation of these strategic resources. Moreover, the identification and characterization of unconventional deposits, such as volcanogenic lithium deposits, represent a significant opportunity to mitigate supply risks and stabilize the market amid the growing demand for these strategic metals.

2. METHODOLOGY

2.1. Sampling

In order to support this study, a total of 22 drill core samples (Fig. 2) and one surface sample were collected during several field campaigns in the Macusani Volcanic Field. High contents of both lithium and cesium and the guidance of Macusani Yellowcake's geologists were used for the selection of the samples. Appendix A contains a list of the samples, including sample codes, geologic units (i.e., Lower Breccia, Lithium-rich Tuff, and Upper Breccia), diamond drill hole code, depth, geographical coordinates, and brief field descriptions. Appendix B contains hand sample photographs and more detailed descriptions. The locations of the surface sample and the collars of the drill cores from which the other samples were collected are shown in Figure 3.

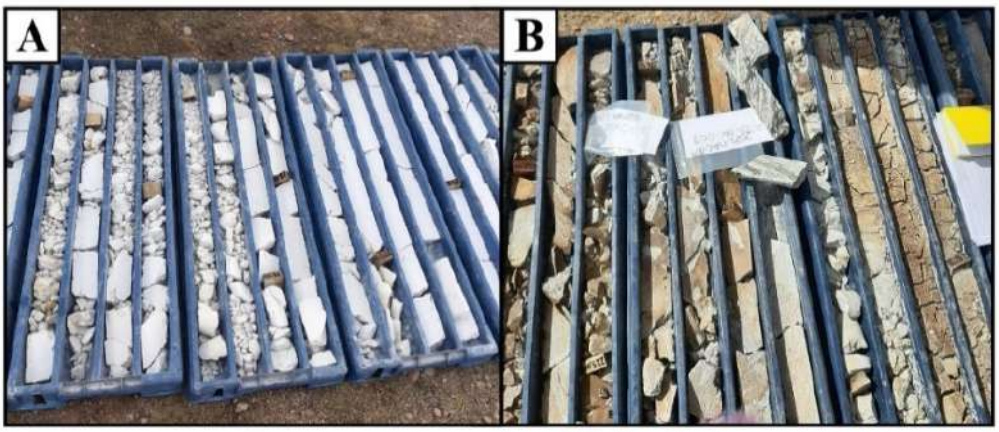

Figure 2. Sampling of drill cores. **A)** Aspect of drill cores from the Falchani Lithium Project from which samples were collected. **B)** The samples were stored in labelled plastic bags.

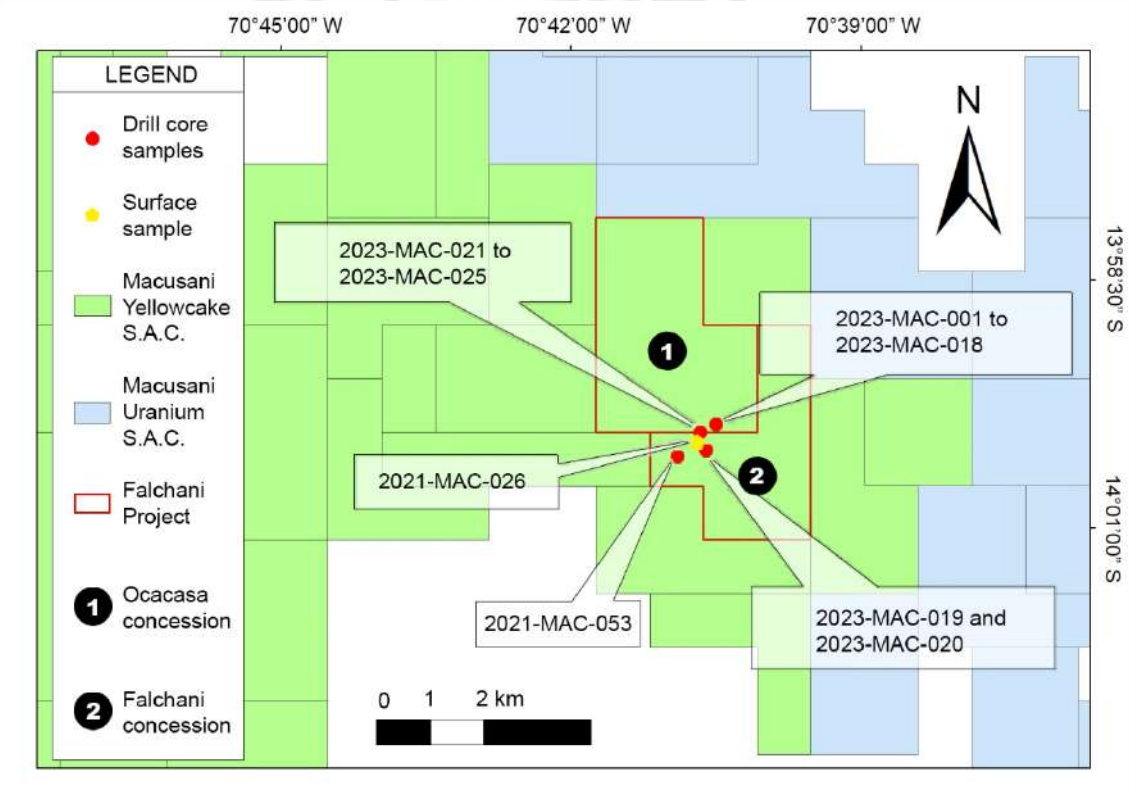

Figure 3. Location of the surface sample (2021-MAC-26) and of the collars of drill cores from which the remaining 25 samples were collected within the Falchani Lithium Project, which is owned by Macusani Yellowcake S.A.C. (GEOCATMIN 2024).

2.2. Analytical methods

2.2.1. X-ray diffraction (XRD)

The rock samples were prepared for bulk and separate mineral analysis. When required, paper-covered rock fractions and separates were initially broken into smaller pieces with a hammer. To separate specific components of the rocks (e.g., brown coatings), a meticulous procedure was followed, utilizing tweezers and other sharp tools. Subsequently, the bulk or separate materials were placed on a bond sheet for storage. Following this process, a total of 36 rock fractions and separates were obtained for XRD analysis. All the fractions and separates were then manually ground in an agate mortar and pestle (Fig. 4A) to a grain size smaller than 35 μm, with the resulting powder stored in labelled plastic vials (Fig. 4B).

For the XRD analysis, I followed the procedure described in Segovia-More (2024). The fine powder material was compacted on standard cylindrical holders (16 mm diameter, 2.5 mm height) to form a smooth surface. XRD data collection was conducted using a PANalytical X'Pert PRO MPD alpha1 powder diffractometer at Scientific and Technological Centers of the University of Barcelona (CCiTUB) and a Bruker D8 Discover diffractometer at Centro de Caracterización de Materiales of the Pontificia Universidad Católica del Perú (CAM-PUCP). Both diffractometers operate in Bragg-Brentano θ/2θ geometry with 280 mm radius using Ni-filtered Cu Kα radiation (λ = 1.5418 Å) and 40 kV–40 mA conditions. Scanning was performed from 4 to 100 º (2θ) at a step size of 0.017° with a scan duration of 1 second per step.

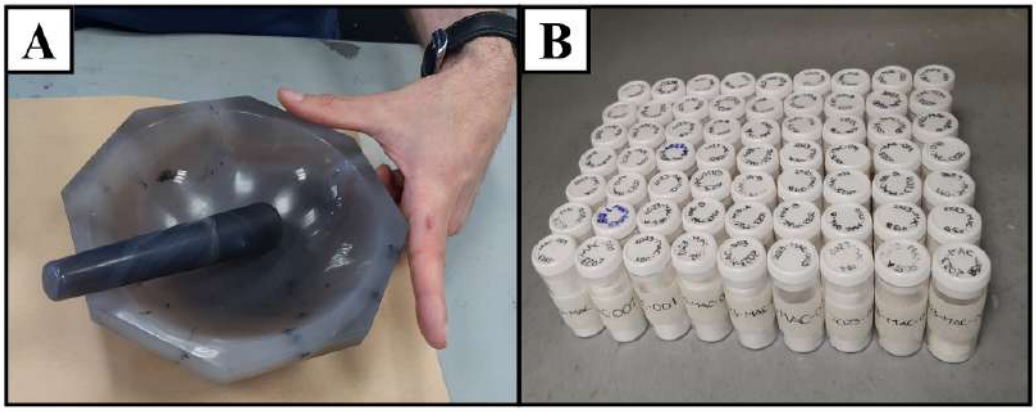

Figure 4. Manual sample preparation for XRD analysis. **A)** Agate mortar and pestle used to prepare rock powder. **B)** Labelled plastic vials with the powdered samples.

Utilizing the PANalytical X'Pert Highscore 2.0.1 software, background noise was subtracted from the diffractogram patterns, peaks were identified, and mineral phases were attributed to each peak. A semi-quantification of the mineral phases was performed using the full-pattern summation (FPS) method, which utilizes full-pattern aggregation based on a reference library of pure diffraction standards. The results of the XRD analyses are detailed in Appendix C.

2.2.2. Optical microscopy

Nine polished thin sections were prepared at the Thin Section Laboratory of the University of Barcelona for subsequent microscopic study. Petrographic analyses were conducted using transmitted and reflected light on a Zeiss Primotech polarizing microscope at the Geology Laboratory of the PUCP. Photomicrographs and detailed microscopic petrographic descriptions of the polished sections analyzed are provided in Appendix D.

3. GEOLOGICAL SETTING

3.1. The Central Andes in southern Peru: The Oriental Cordillera

The Andes Cordillera of South America, shaped by the subduction of the Nazca oceanic plate under the South American continent, is classically divided into the Northern (0-15°S), Central (15-33°S), and Southern (33-56°S) domains (Kay and Mpodozis 2020). The Central Andes have an extension of ~4,000 km, and at the latitudes of southern Peru, they comprise the Western Cordillera, the Altiplano-Puna Plateau, the Eastern Cordillera, and the Subandean fold and thrust belt as major geomorphotectonic units (Fig. 5; Wörner et al. 2018; Kay and Mpodozis 2020).

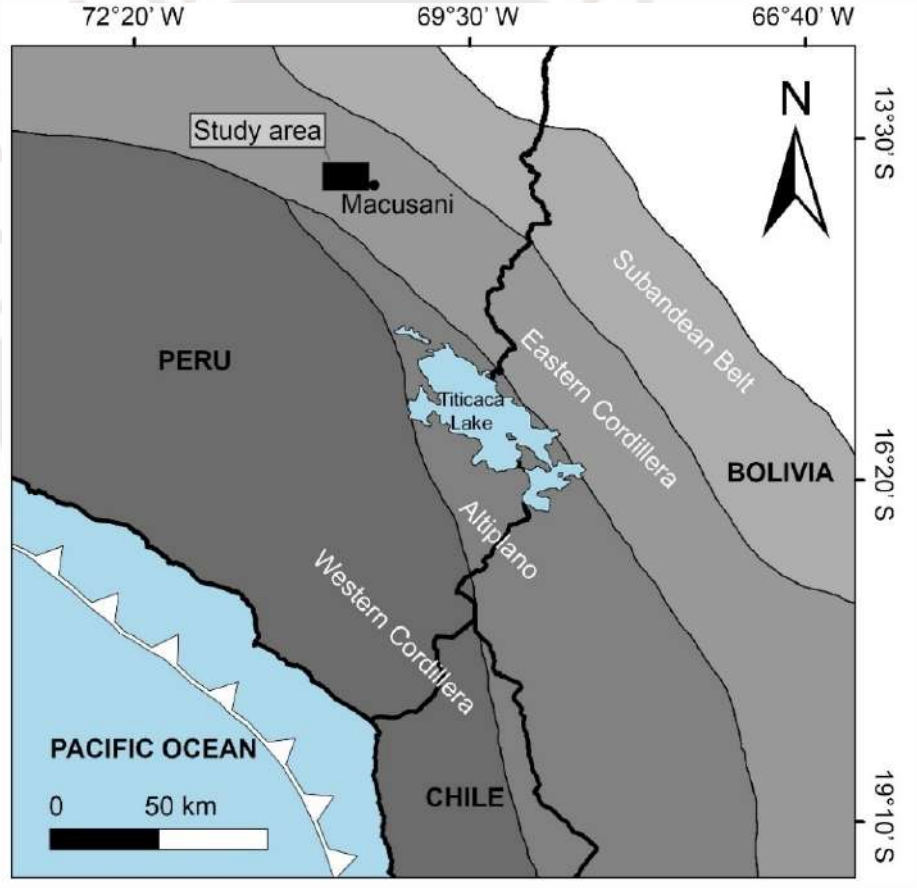

Figure 5. Geomorphotectonic units of the Central Andes, highlighting the location of the study area within the Eastern Cordillera. Modified from Kontak et al. (1990).

The study area is located in the Eastern Cordillera of the Central Andes in southeastern Peru (Fig. 5). The Eastern Cordillera stands as a high-elevation range that separates the Altiplano from the Sub-Andean thrust and fold belt and foreland basin. The axis of present-day Eastern Cordillera in southern Peru and northern Bolivia coincides with the axis of the Mitu rift system, which was associated with the breakup of Pangea in the late Permian and Triassic (Sempere et al. 2002; Mišković et al. 2009; Spikings et al. 2016). The igneous and sedimentary rocks deposited within the Mitu rift system are grouped under the Mitu Group and unconformably overlie dominantly Paleozoic metasedimentary rocks of marine origin (for a review of proto-Andean geodynamics, see Chew et al. 2007, 2016). Mitu Group rocks in Peru include Triassic molasse facies, alkaline-subalkaline basalts, and basaltic andesites deposited between ca. 240 to 220 Ma (Reitsma 2012; Spikings et al. 2016). The volcanic rocks, predominantly basaltic to andesitic in composition, exhibit intraplate alkaline signatures (Kontak et al. 1990). The Late Triassic and Early Jurassic marked the end of rifting and the onset of subduction-related arc magmatism between the Jurassic and Early Cretaceous in the Central Andes (Mišković et al. 2009; Kay and Mpodozis 2020). Since the Late Oligocene, the Central Andes have been characterized by a high rate of plate convergence, intense orogenic uplift, and significant magmatism, which have shaped the topography of the region and geological structure (Perez and Horton 2014; Carlotto et al. 2023; Falkowski et al. 2023).

The Eastern Cordillera in southeastern Peru comprises three morphotectonic provinces, which frow the southwest to the northeast include i) the Central Andean Backthrust Belt, which is a southwest-verging system formed by tectonic inversion of a Mesozoic back-arc basin; ii) the Macusani Structural Zone, which is described in detail below; and iii) the Cordillera de Carabaya, where are exposed Neoproterozoic to Mesozoic volcanic, sedimentary, and metamorphic sequences, as well as Triassic-Jurassic and Paleogene-

Neogene volcanic and intrusive rocks (Laubacher 1978; Kontak et al. 1990; Sandeman et al. 1997; Perez et al. 2016a).

3.2. The Macusani Structural Zone

The Macusani Structural Zone, also known as the “Precordillera de Carabaya” (Kontak et al. 1990; Sandeman et al. 1997) or "Late Hercynian" fold domain (Laubacher 1978), is characterized by its high, uniform structural elevation along strike resulting in the exposure of Carboniferous, Permian, and Triassic rock units. As summarized by Perez et al. (2016b), it records a complex geologic history that includes three major phases of deformation. The first, the Eohercynian deformation phase, occurred in the Late Devonian to Early Carboniferous, forming NW-trending folds in Ordovician–Devonian rocks, which are overlain by Carboniferous–Permian sedimentary rocks. During the Late Permian, the second phase, known as “Late Hercynian”, produced faults and folds in upper Paleozoic strata with sigmoidal orientations, interpreted as NW-trending, in échelon folds formed in a left-lateral shear zone and later refolded. The third phase, associated with the Andean orogeny, involved the reactivation of pre-existing structures as thrust faults, with the Triassic Mitu Group being cut by NW-trending thrust faults parallel to those of the late Permian structures.

The Lower Paleozoic sedimentary sequences in the Macusani Structural Zone, which can be up to 7,000 m thick, consist mainly of the Middle Ordovician San José Formation and the Upper Ordovician Sandia Formation (Laubacher 1978). The San José Formation is characterized by a flysch-like sequence of fossiliferous black shale interspersed with minor layers of sandstone. The Sandia Formation comprises a detrital sequence of quartzite alternating with gray-black shale. Above these units lies the Ananea Formation, a Silurian-Devonian sequence over 2,500 m in thickness, composed of black shale interbedded with quartzite in its upper part (Laubacher 1978).

The Upper Paleozoic lithologies include carbonate and detrital facies that discordantly overlie the Lower Paleozoic series. They correspond to the Mississippian Ambo Group and the Pennsylvanian Tarma Group, which consist of siliceous-calcareous marine deposits of sandstone, shale, and limestone (Laubacher 1978). In the early Permian, the Copacabana Group was deposited in an epicontinental sea and is characterized by fossiliferous limestone intercalated with sandstone, black shale, and cherty limestone (Sempere et al. 2002).

The sedimentary continuity observed between the early Permian Copacabana Group and the Upper Triassic Mitu Group reflects Middle Triassic continental rifting that facilitated the accumulation of sedimentary and volcanic rocks (Laubacher 1978; Sempere et al. 2002; Spikings et al. 2016). In the Macusani Structural Zone, the Triassic Mitu Group is characterized by the predominance of volcanic facies over detrital ones. This distinctive characteristic is attributed to the proximity to emission centers (Laubacher 1978; Panca et al. 2024).

Jurassic and Cretaceous rock units in the Macusani Structural Zone have more restricted exposure compared to the Paleozoic and Triassic rocks, and include the Muni, Huancané, Viluyo, Ayabacas, and Vilquechico formations (Rodríguez et al. 2021). The Upper Jurassic and Lower Cretaceous Muni Formation was deposited in fluvial and aeolian environments and consists of alternating siltstone, mudstone, and fine-grained arkosic sandstone, all of which exhibit characteristic reddish-brown hues (López 1996; Rodríguez et al. 2021). The Lower Cretaceous Huancané Formation consists of massive white sandstone with occasional intercalations of shale, deposited in a fluvial and eolian environment (Newell 1949; Rodríguez et al. 2021). The Lower Cretaceous Viluyo Formation consists of a sequence of arkosic or quartzitic sandstone and forms an angular unconformity with the overlying Ayabacas Formation (López 1996; Rodríguez et al.

2021). The Turonian-Coniacian Ayabacas Formation is composed of gray packstone deposited in an unstable shelf marine environment (Callot 2008; Rodríguez et al. 2021). The Coniacian-Maastrichtian Vilquechico Formation (also known as the Hanchipacha Formation; e.g., Newell 1949) consists of green or grey pelitic sequences deposited in a fluvial floodplain environment (Newell 1949; Rodríguez et al. 2021). The last three formations are part of the Moho Group.

The Macusani Structural Zone encompasses significant Tertiary volcanic fields, including Macusani (also known as Quenamari), Cayconi, and Picotani (Sandeman et al. 1996, 1997). Volcanic and volcaniclastic units in these fields were grouped under the Crucero Supergroup by Sandeman et al. (1996; 1997). The Crucero Supergroup encompasses two distinct groups: i) the older Picotani Group and ii) the younger Quenamari Group. The Picotani Group consists of a sequence of Late Oligocene to Early Miocene (ca. 22-26 Ma) rhyodacitic volcanic rocks interbedded with mafic flows (Sandeman et al. 1997; Sandeman and Clark 2003). Specifically, the (sub)volcanic rocks include rhyodacite, S-type rhyolite, lamprophyre, medium- to high-K calc-alkaline basalt, and shoshonite. This group is subdivided into the Cerro Queuta, Cerro Huancahuancane, Cerro Sumpiruni, Pucalacaya, Lago Perhuacarca, Cerro Moromoroni, Cerro Cancahuine, Pachachaca, Jama Jama, and Suratira formations. The Quenamari Group comprises Miocene (ca. 17-6.5 Ma) strongly peraluminous rhyolitic ash flow-tuff and is subdivided into the Huacchane, Quebrada Escalera, and Macusani formations. While the Huacchane and Quebrada Escalera formations are found in the Picotani Field, the Macusani Formation occurs in the Macusani Volcanic Field (Sandeman et al. 1997). Tertiary intrusive suites in the area were grouped by Sandeman et al. (1997) into the Crucero Intrusive Supersuite, which comprises i) the older Picotani Intrusive Suite and ii) the younger Quenamari Intrusive Suite, which are co-genetic with the homonymous volcanogenic rocks of the Crucero Supergroup.

3.3. The Macusani Volcanic Field

The Macusani Volcanic Field comprises a sequence of rhyolitic ash-flow tuff exposed in the Quenamari Plateau at 4,400 m.a.s.l. and covers an area of ~860 km² (Cheilletz et al. 1992). The exposed volcanic rocks of the Crucero Supergroup belong to both the Picotani and Quenamari groups (Fig. 6). The first group is represented by the Lago Perhuacarca, Pucalacaya, and Cerro Sumpiruni formations. These formations are exposed in Nevado Ollo Quenamari (near the Perhuacarca Lake), the Ninahuisa Valley (near the Ninahuisa River), and Cerro Sumpiruni Mountain, respectively, all located on the southeastern margin of the volcanic field. The second group is represented by the Macusani Formation, which is the youngest unit of the Crucero Supergroup (Sandeman et al. 1997). It covers most of the volcanic field area and is described in more detail below, as it is the unit that hosts the lithium-ore units in the Falchani Lithium Project (Nupen 2019). Intrusive units of the Crucero Supersuite are exposed along the central and southern areas of the Macusani Volcanic Field and include the Quebrada Centilla Stock, the Ninahuisa Stock, and the Revancha Dike of the Picotani Suite, and the Chacacuniza Stock and the Nevado Ollo Quenamari Plug of the Quenamari Suite (Sandeman et al. 1997).

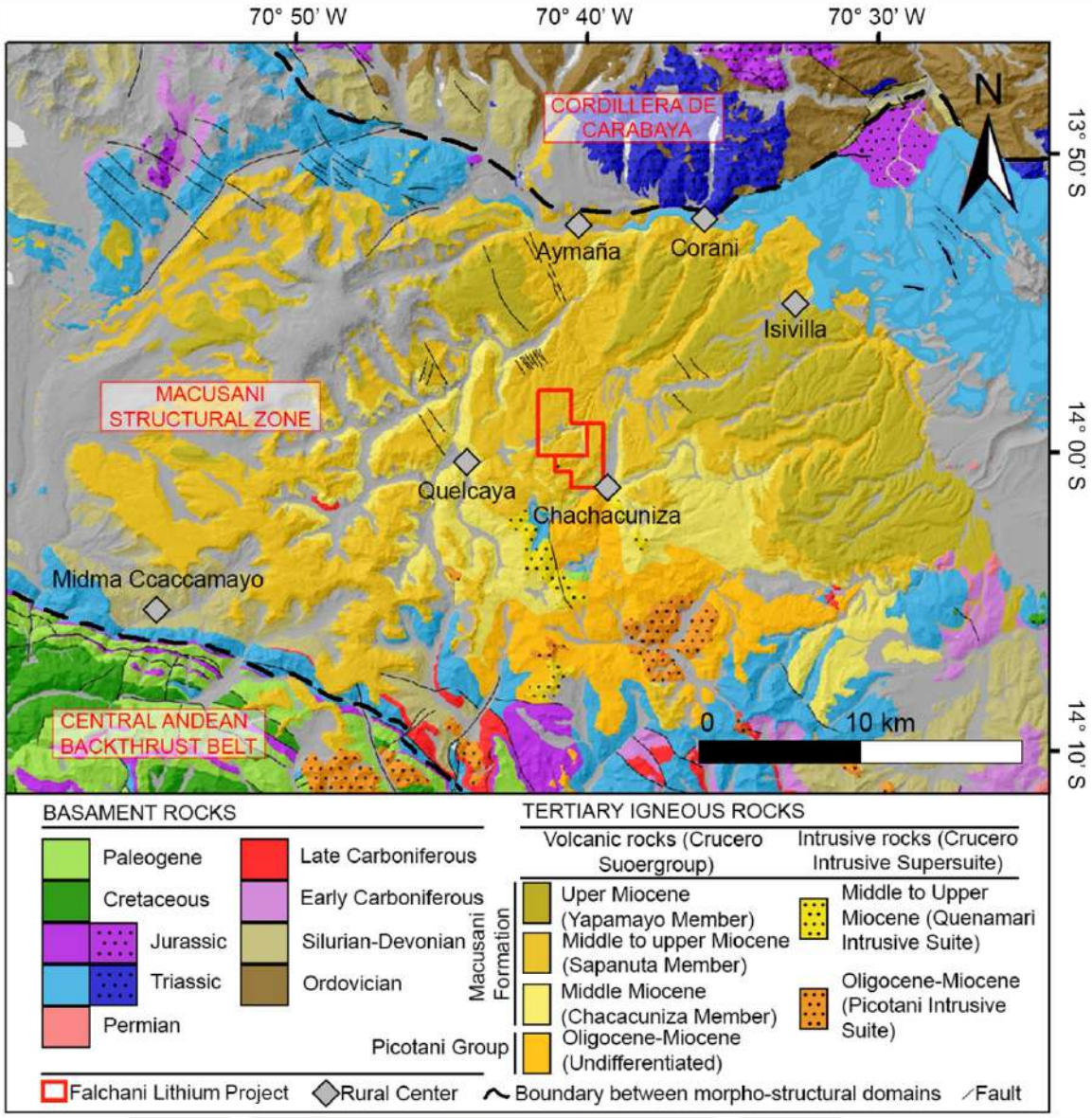

Figure 6. Geological map of the Macusani Volcanic Field, modified from Pichavant et al. (1988), Sandeman et al. (1998), and Kontak et al. (1990).

The Macusani Formation (a.k.a. Quenamari Formation; e.g., López 1996) is a 340 to 440 m-thick sequence of poorly stratified, moderately welded, whitish gray, crystal-rich, rhyolitic ash- and lapilli-flow tuff (Cheilletz et al. 1992; Sandeman et al. 1997). Valencia and Arroyo (1985) described the formation as consisting of alternating tuff and ignimbrite. Juvenile pumice and shard fragments are more common than lithic fragments of pelite, andesite, granite, and quartzite (Cheilletz et al. 1992). Li (2016) identified quartz (7–15%), sanidine (15–20%), plagioclase (10–15%), biotite (2–4%), and muscovite (0–1%) as the

main minerals in the Macusani Formation. Pichavant et al. (1988) noted two crystallization stages: an early magmatic stage with plagioclase, biotite, tourmaline, spinel, cordierite, sillimanite, and other accessory minerals, followed by a main stage marked by quartz, sanidine, plagioclase, muscovite, and andalusite, along with some biotite, and accessory ilmenite, apatite, monazite, and zircon. Geochemically, the Macusani Formation consists of strongly peraluminous, felsic volcanic rocks associated with S-type reduced magmas (Pichavant et al. 1988) and is enriched in lithophile incompatible elements like Li, Rb, Cs, Be, B, Sn, F, P, and U (Noble et al. 1984; Pichavant et al. 1988; Ramirez-Briones et al. 2025).

$^{40}Ar/^{39}Ar$ dating of biotite from the Macusani Formation revealed two eruptive cycles at 10 ± 1 Ma and 7 ± 1 Ma (Cheilletz et al. 1992). Additionally, a $^{40}Ar/^{39}Ar$ biotite plateau date of 10.357 ± 0.080 Ma from the Corani mining area (Ullrich 2006) supports early eruptions in the southwestern portion of the field (Cheilletz et al. 1992).

The Macusani Formation has been divided into the Chacacuniza, Sapanuta, and Yapamayo members (Fig. 6) by López (1996). According to this author, the Chacacuniza Member consists of poorly stratified rhyolitic tuff with lapilli fragments and crystal clasts of quartz, plagioclase, K-feldspar, and biotite, which appear alongside volcanic glass in a crypto-crystalline matrix. It overlies angular unconformity rocks of the Mitu Group and underlies the Sapanuta Member. In the NE sector of the 29u sheet (Payacucho-Quisco Punco), it underlies the Yapamayo Member. The Sapanuta Member consists of a thick succession of rhyolitic tuff with distinctive columnar jointing. It comprises quartz, K-feldspar, plagioclase, and biotite crystal clasts and lithic fragments embedded in a cryptocrystalline matrix. Amygdales are filled with calcedony. It lies unconformably over the Mitu Group and the Ananea, Muni, Huancané, Viluyo, and Vilquechico formations and conformably over the Chacacuniza Member. Finally, the Yapamayo Member is a crystal-rich rhyolitic

tuff sequence with lapilli and lithoclasts. Crystals include quartz, albite, sanidine, and biotite, all ser within a cryptocrystalline matrix. It unconformably overlies the Sapanuta Member.

3.4. The Falchani Lithium Project

The Falchani Lithium Project comprises five units as described by Nupen (2019) and Loveday and Karstick (2023), which, from bottom to top, are the Coarse Felsic Intrusion (formerly named as Lower Rhyolite by Nupen 2019), the Lower Breccia, the Lithium-rich Tuff, the Upper Breccia, and the Upper Rhyolite. The Coarse Felsic Intrusion is a non-mineralized unit characterized by the presence of rhyolitic rocks underlying the tuff and breccia levels (Nupen 2019). The Lower Breccia is up to 175 m thick and contains large blocks (~20 m) of tuff with high lithium contents (mean values of 2,134 ppm Li and 1,457 ppm Cs; Loveday and Karstick 2023). Its characteristic pervasive alteration to smectite has obliterated most primary textures, resulting in distinctive low hardness and clayey, saccharoidal textures (Segovia-More 2024). Scarce, medium ash-sized dark mica crystal clasts are locally observed within the unit. The 50 to 140 m-thick Lithium-rich Tuff is a very fine-grained rock, light gray to white in color, with prominent bedding. This level is the main ore unit at the Falchani Lithium Project, with mean values of 3,093 ppm Li and 517 ppm Cs (Loveday and Karstick 2023). It comprises finely laminated or, in some areas, massive volcanic mudstone with alternating white and gray laminae, containing fairly abundant Li-F micas in the matrix and as crystal clasts (Ramírez-Briones et al. 2025; Torró et al. 2025). The lamination is often strongly folded and contorted, although it is occasionally planar. Loveday and Karstick (2023) propose that the Lithium-rich Tuff was subaerially deposited in a lacustrine environment. The Upper Breccia, which is mineralized with a mean of 1,672 ppm Li and 684 ppm Cs contents, is approximately 10 to 20 m thick and includes angular clasts in a fine-grained matrix (Loveday and Karstick

2023). This unit comprises brecciated volcaniclastic facies that are extensively altered to smectite (Segovia-More 2024). The rocks of the Upper Breccia are predominantly non-cohesive, clay-rich, and exhibit white to grayish-white tones. The breccia is largely clast-supported, with angular clasts ranging in size from 2 to 5 cm in size. Within the clasts, occasional medium- to coarse-sized fragments of mica, K-feldspar, and translucent quartz crystals are observed (Segovia-More 2024). Finally, the Upper Rhyolite, which is non-mineralized, forms prominent outcrops on the surface with poorly defined stratification that slightly dips to the north-northeast (Nupen 2019).

$^{40}Ar/^{39}Ar$ dating on Li-F mica crystal clasts from the Lithium-rich Tuff yielded plateau dates ranging from 8,978 ± 73 ka to 8,717 ± 44 ka (Sanandres-Flores 2024, later published in Torró et al. 2025). The youngest of these dates constrains the time of deposition of the tuffaceous units containing the lithium mica crystal clasts, which coincided with the volcanic gap between the two previously documented eruptive events in the Macusani Formation at 10 ± 1 Ma and 7 ± 1 Ma (Cheilletz et al. 1992).

The Li-ore units are primarily composed of quartz, plagioclase, K-feldspar, and variable proportions of Li-F mica, clay minerals (kaolinite-group and smectite), and zeolites (Segovia-More et al. 2023; Segovia-More 2024; Torró et al. 2025). Based on mineralogical composition of alteration assemblages, Segovia-More et al. (2023) and Segovia-More (2024) divided the ore-samples into three main groups: i) mica with kaolinite, ii) smectite ± mica, and iii) zeolite with mica. Micas from the Lithium-rich Tuff are classified within the zinnwaldite and lepidolite series (Torró et al. 2025). Smectite is Mg-poor and dioctahedral (Segovia-More et al. 2023), ruling out the presence of hectorite, a Li-bearing trioctahedral smectite commonly found in other volcanogenic lithium deposits (Bowell et al. 2020; Grew et al. 2020; Putzolu et al. 2025a). Cation exchange

analyses show that Li is adsorbed onto, or occupies interlayer positions within, smectite (Segovia-More 2024).

The Li-ore units are primarily composed of SiO_2 (60.4–73.9 wt.%), Al_2O_3 (14.0–20.1 wt.%), K_2O (1.3–6.8 wt.%), and Na_2O (1.3–4.6 wt.%), with other minor oxides jointly contributing ~1.2 wt.% on average (Ramirez-Briones et al. 2025). Smectite-dominant samples show higher LOI values (8.2–13.5 wt.%) compared to kaolinite-dominant ones (1.7–4.4 wt.%). Geochemically, most samples are classified as rhyolite; however, some samples of Upper and Lower Breccia samples with high smectite contents exhibit coupled alkali and silica depletion with increasing LOI, which these authors have interpreted as post-depositional alteration under alkaline pH conditions (Ramirez-Briones et al. 2025). The contents of fluid-mobile, lithophile incompatible elements like Li (up to 4,160 ppm), F (up to ~2 wt. %), Cs (up to 8,993 ppm), Rb (up to 2,177 ppm), and Sn (up to 274 ppm) are notably high, which is interpreted by Ramirez-Briones et al. (2025) as due to high degrees of crystal fractionation and fluid-saturated magma conditions in a pre-eruptive stage.

4. RESULTS

4.1. Macroscopic description of the samples

The studied rocks display a variety of textures and colors at the hand sample scale. Most of the samples exhibit a conspicuous white color in freshly cut surfaces and a homogeneous, very fine-grained granularity (Figs. A-G). Some of these exhibit widespread dark brown patinas (Figs. 7 B-C, E-G). While some appear as soft, clayey masses (Figs. 7A-B), most are consolidated and hard (Figs. 7 C-G). Mineral identification is challenging both macroscopically and under loupe magnification (10x-20x) due to the very fine-grained nature of the samples. Amorphous silica ± quartz (<0.4 mm) with gray, milky, or smoky colors is locally identifiable along with anhedral whitish plagioclase (<0.5 mm) and

sparse dark, brown to greenish brown micas (<1 mm). Soft clay minerals show smooth textures and typical adhesion when tested by tongue.

Another set of samples exhibits more complex textures with well-preserved primary features (Figs. 7 G-L). These textures include laminar to irregular anastomosing patterns characterized by alternating brighter and darker bands (Figs. 7G-H), which grade into brecciated to blocky patterns (Figs. 7I-J). Possible directional solidification structures, defined by centimeter-scale domains of grayish material in sharp, rectilinear contact with the white host rock and displaying acute triangular terminations, have also been identified locally (Fig. 7K). In addition, a few samples contain consolidated breccias with subangular to rounded white clasts cemented in a dark gray matrix (Fig. 7K).

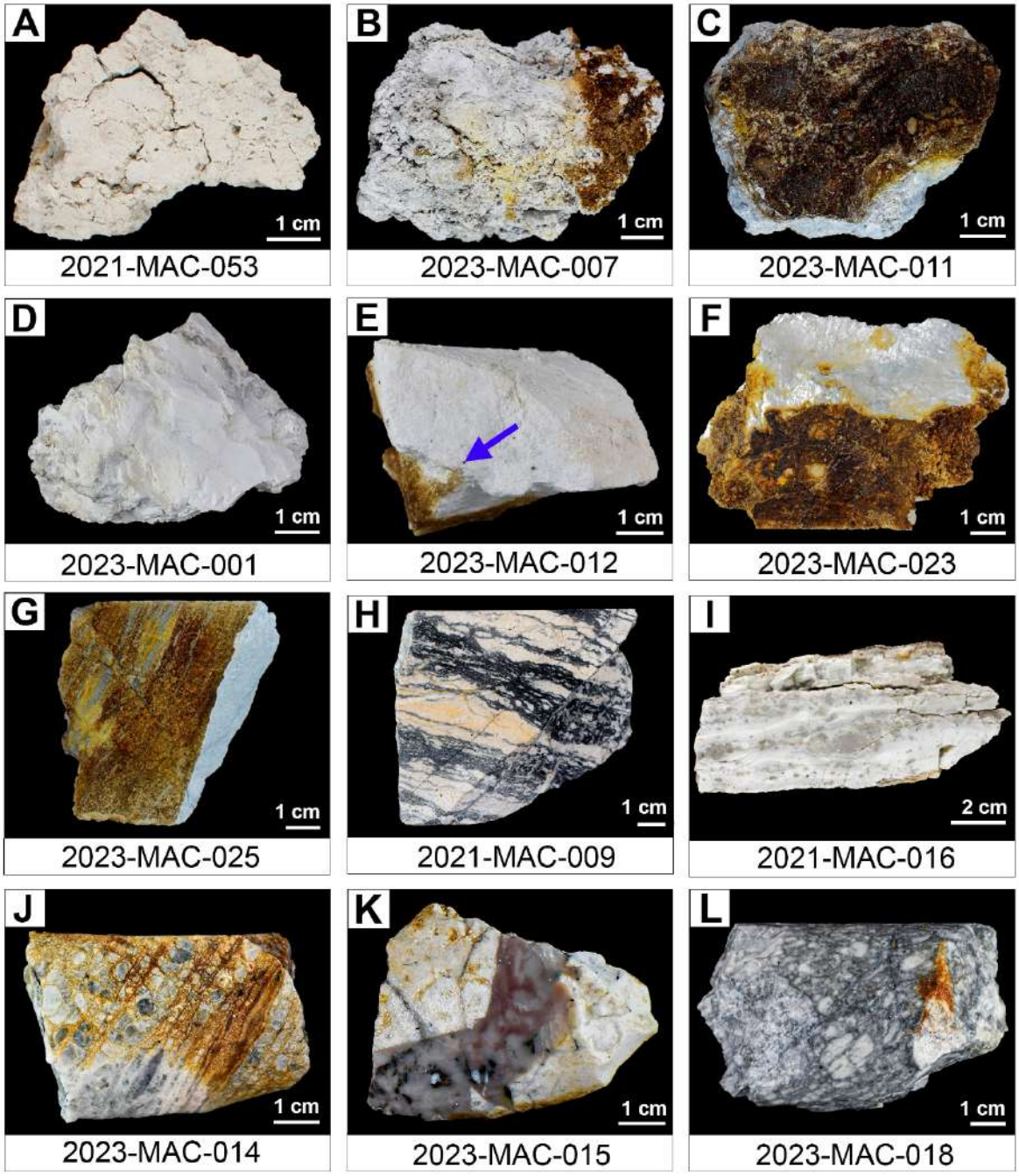

Figure 7. Aspect of representative hand samples. **A)** Fine-grained clayey material. **B)** Highly altered material with a light brown patina on the right surface edge; the sample is soft to the touch and easy to disintegrate. **C)** Whitish clayey material, a little rough to the touch, with a conspicuous dark brown patina all over its upper face. **D)** White, consolidated rock, with a smooth surface and containing small lithic fragments and dark mica randomly distributed within the clayey matrix. **E)** White, fine-grained sample with scattered dark brown subhedral dark mica crystal clasts (arrow). **F-G)** Massive, hard clay-rich material with a light brown coating over

most of its surface, which contrasts with the white color of the freshly-cut rock sample. **H)** Anastomosed light and dark banding. **I)** Laminar to anastomosed alternating white and brownish-grayish layers bands; the brownish-gray bands are discontinuous with internal brecciated texture. **J)** Banded rock with intercalation of levels rich in translucent to gray glass clasts defining a blocky texture. **K)** Very fine-grained gray material with a pinkish stain in sharp contact with a very fine-grained white host rock; acute triangle terminations of the gray material might indicate unidirectional solidification textures. **L)** Brecciated texture with rounded to angular and irregular clasts embedded in a very fine-grained dark gray matrix. The clast in the lower central area of the sample is split into three sub-clasts, depicting a local jigsaw-fit texture.

4.2. Mineralogy

According to the XRD results obtained in this thesis, most samples comprise quartz, feldspar, and mica, likely representing primary phases, along with secondary minerals, mainly clays and zeolites (Table 2; Fig. 9). Low-crystallinity silica phases such as "opal" [$SiO_2 \cdot nH_2O$] and tridymite [SiO_2] were identified as possibly present. Petrographic observations (see below) indicate that the amount of quartz is very limited and that, instead, more amorphous varieties of silica are dominant. The relatively high diffraction peak at ~26.5 º (2θ) from which quartz is often identified is also shared by other silicate minerals present in the samples, such as feldspar and mica, and therefore their intensity might reflect the addition of these minerals as well; as a result, the abundance of quartz can be overestimated. On the other hand, there are several overlapping diffraction peaks between opal/cristobalite and silicate minerals such as quartz and feldspars, which further complicates their identification and proper quantification. The assemblage of low crystallinity silica phases species at Falchani was defined as chalcedony—micro- and nano-scale intergrowths of polycrystalline quartz, cristobalite/opal-C, and amorphous silica/opal-A according to TEM results by Torró et al. (2025). Additionally, the diffraction patterns suggest the presence of virgilite [$LiAlSi_2O_6$] in two samples. Noteworthy, the

Macusani Volcanic Field is the type locality for virgilite, a mineral which has not been described in any other locality (French et al. 1978). The analyses also indicate that brown patinas show similar mineralogical compositions to their white counterparts (Appendix C).

Identified clay minerals belong to the kaolinite subgroup and smectites of the montmorillonite [$(Na,Ca)_{0.33}(Al,Mg)_2(Si_4O_{10})(OH)_2 \cdot nH_2O$] – beidellite [$(Na,Ca_{0.5})_{0.3}Al_2((Si,Al)_4O_{10})(OH)_2 \cdot nH_2O$] series (see also Segovia-More et al. 2023). Mixed-layer clay minerals (cf. MacEwan and Ruiz-Amil 1975; Reynold 1980), such as illite-montmorillonite (including rectorite—a 1:1 regular interstratification of muscovite/illite and montmorillonite) were also noted. Smectite and mixed-layer clay minerals occur in most of the samples (n = 28), whereas kaolinite is present in identifiable proportions in a few samples (n = 10).

Zeolite minerals are present in most, but not all, the studied samples. The most common identified zeolite is mordenite [$(Na_2,Ca,K_2)_4(Al_8Si_{40})O_{96} \cdot 28H_2O$], which has been identified in 23 of the 36 analyzed samples. Other identified zeolite minerals include mutinaite [$Na_3Ca_4Si_{85}Al_{11}O_{192} \cdot 60H_2O$], which has been detected in 12 samples, and clinoptilolite [$(Na/Ca/K)_{3-6}(Si_{30}Al_6)O_{72} \cdot 20H_2O$] and heulandite [$(Na/Ca/K)_{5-6}(Al_{8-9}Si_{27-28}O_{72}) \cdot nH_2O$], which have only been found in two samples each (Table 2). In most samples, more than one zeolite mineral is commonly identified. However, it should be noted that distinguishing between zeolite minerals through XRD may be challenging due to their similar framework structures, overlapping characteristic peaks, variable crystallinity, and the presence of mixed mineral phases in natural samples. Small variations in cation content and degree of hydration can also cause subtle shifts in peak positions, which hinder an unambiguous identification (Bish and Ming 2001).

According to the dominant secondary minerals, the samples can be classified into i) zeolite type (n = 7 samples); ii) zeolite + smectite/mixed-layer clay type (n = 16); iii) zeolite + smectite/mixed-layer clay + kaolinite subgroup type samples (n = 6); iv) smectite/mixed-layer clay dominant type (n = 4); and v) kaolinite subgroup dominant type (n = 3; Fig. 8).

Table 2. Minerals identified in samples from the Falchani Lithium Project using XRD including rock forming minerals (Pl: plagioclase, Mca: mica, Qz: quartz, and Kfs: K-feldspar), zeolite group minerals (Mor: mordenite, Mut: mutinaite, Cpt: clinoptilolite, and Hul: heulandite), clay minerals (Kln: kaolinite subgroup minerals, Sme: smectite, mixed-layer clay group minerals (Ilt-Mnt: illite-montmorillonite, Rec: rectorite), and other minerals (Vir: virgilite, Opl: opal, and Trd: tridymite).

Sample code	UNIT	Rock forming minerals				Zeolite group minerals				Clay group minerals		Mixed-layer clay group minerals		Other minerals		
		Pl	Mca	Qz	Kfs	Mor	Mut	Cpt	Hul	Kln	Sme	Ilt-Mnt	Rec	Vir	Opl	Trd
2021-MAC-026	LRT	XX	X	XXX		XXX	X			X						
2021-MAC-053	LRT	XX	XX	XXX		XXX	X									
2023-MAC-001	UBX	XX	XX	XXX	XX					XXX	XX					
2023-MAC-002	LBX	XX	X	XXX	XX					XX		X		XXX		
2023-MAC-005A	LBX		X				X			XX	X					
2023-MAC-005B	LBX						X			XX	X					
2023-MAC-005C	LBX		X				XX			XXX	X					
2023-MAC-006A	LBX												XX			XX
2023-MAC-006B	LBX												XXX			XX
2023-MAC-007A	LBX	XX		XXX		X	XX						X			
2023-MAC-007B	LBX	XXX	X	XXX								XX				
2023-MAC-008A	LBX		X	XX		XXX				X	XX					
2023-MAC-008B	LBX	XXX		XXX		XX						XX				
2023-MAC-009	LBX		XX	XXX	XXX	X										
2023-MAC-011A	LBX		X	XXX		XX			XX			XX				
2023-MAC-011B	LBX			XXX		XX			XX			X				
2023-MAC-012	LBX		X	X	X	X					X					
2023-MAC-013A	LBX		X						X	X	XX					
2023-MAC-013B	LBX		X	X						XX			XX			
2023-MAC-014	LBX		X			XXX							XX	XXX		
2023-MAC-015A	LBX	XXX				XXX					XX					
2023-MAC-015B	LBX	XX				XXX					XXX					
2023-MAC-016	LBX					XXX		XXX					XX			
2023-MAC-017A	LBX			XXX	XX	XXX					XX					
2023-MAC-017B	LBX		XX	XXX	XXX	XX	X		X							
2023-MAC-018	LBX			XXX		XXX	X				XX					
2023-MAC-020	LRT	XX	XX		XXX					XX						
2023-MAC-021A	LBX	XX				XXX			X				XX			
2023-MAC-021B	LBX		X			XXX			XX		XX				XX	
2023-MAC-022A	LBX	XX			XX			XXX			XX				XX	
2023-MAC-022B	LBX	XX			XXX			XXX			XXX				XX	
2023-MAC-023A	LBX			XXX	XXX	XX					XX					
2023-MAC-023B	LBX	XX		XX		XXX					XX					
2023-MAC-024A	LBX		XX	XXX	XXX	XXX	X									
2023-MAC-024B	LBX		XX	XXX	XXX	XXX	X									
2023-MAC-025	LBX		XX	XXX		XXX	X									

Note: A value of X indicates a score less than or equal to 20%, XX indicates a score greater than 20% and less than or equal to 40%, and XXX indicates a score greater than 40%.

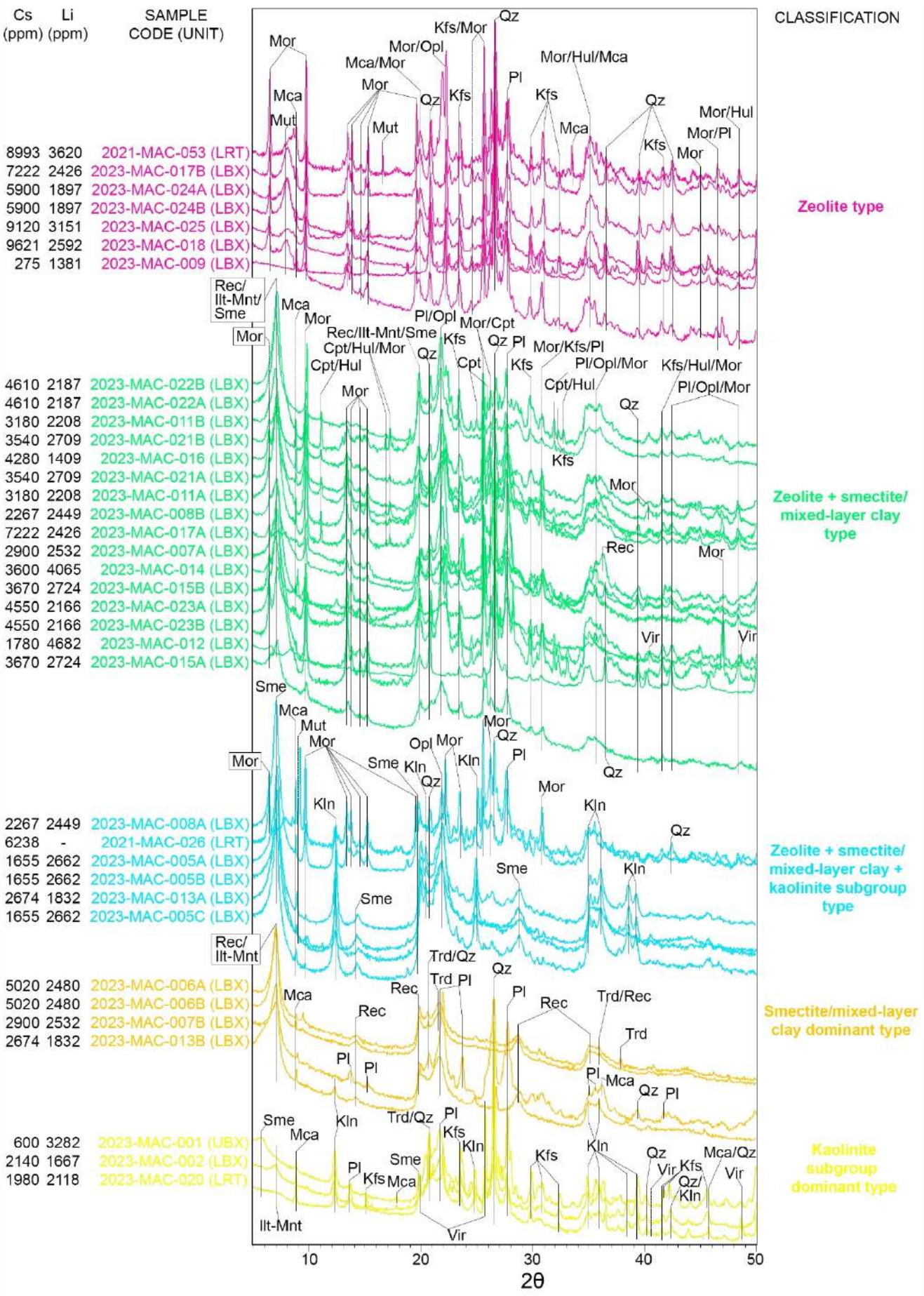
Cs (ppm)
Li (ppm)
SAMPLE CODE (UNIT)
CLASSIFICATION
8993 3620 2021-MAC-053 (LRT)
7222 2426 2023-MAC-017B (LBX)
5900 1897 2023-MAC-024A (LBX)
5900 1897 2023-MAC-024B (LBX)
9120 3151 2023-MAC-025 (LBX)
9621 2592 2023-MAC-018 (LBX)
275 1381 2023-MAC-009 (LBX)
Zeolite type
4610 2187 2023-MAC-022B (LBX)
4610 2187 2023-MAC-022A (LBX)
3180 2208 2023-MAC-011B (LBX)
3540 2709 2023-MAC-021B (LBX)
4280 1409 2023-MAC-016 (LBX)
3540 2709 2023-MAC-021A (LBX)
3180 2208 2023-MAC-011A (LBX)
2267 2449 2023-MAC-008B (LBX)
7222 2426 2023-MAC-017A (LBX)
2900 2532 2023-MAC-007A (LBX)
3600 4065 2023-MAC-014 (LBX)
3670 2724 2023-MAC-015B (LBX)
4550 2166 2023-MAC-023A (LBX)
4550 2166 2023-MAC-023B (LBX)
1780 4682 2023-MAC-012 (LBX)
3670 2724 2023-MAC-015A (LBX)
Zeolite + smectite/ mixed-layer clay type
2267 2449 2023-MAC-008A (LBX)
6238 - 2021-MAC-026 (LRT)
1655 2662 2023-MAC-005A (LBX)
1655 2662 2023-MAC-005B (LBX)
2674 1832 2023-MAC-013A (LBX)
1655 2662 2023-MAC-005C (LBX)
Zeolite + smectite/ mixed-layer clay + kaolinite subgroup type
5020 2480 2023-MAC-006A (LBX)
5020 2480 2023-MAC-006B (LBX)
2900 2532 2023-MAC-007B (LBX)
2674 1832 2023-MAC-013B (LBX)
Smectite/mixed-layer clay dominant type
600 3282 2023-MAC-001 (UBX)
2140 1667 2023-MAC-002 (LBX)
1980 2118 2023-MAC-020 (LRT)
Kaolinite subgroup dominant type
Mor
Mca
Mut
Qz
Kfs
Kfs/Mor
Mor/Opl
Mca/Mor
Pl
Mor/Hul/Mca
Mor/Hul
Mor/Pl
Rec/ Ilt-Mnt/ Sme
Pl/Opl
Mor/Cpt
Rec/Ilt-Mnt/Sme
Cpt/Hul/Mor
Cpt/Hul
Cpt
Mor/Kfs/Pl
Pl/Opl/Mor
Kfs/Hul/Mor
Rec
Vir
Sme
Opl
Kln
Rec/ Ilt-Mnt
Trd/Qz
Trd
Trd/Rec
Ilt-Mnt
10
20
30
40
50
2θ

Figure 8. XRD patterns grouped by dominant alteration mineral paragenesis (see text for details). When available, the Li (ppm) and Cs (ppm) contents, as provided by Macusani Yellowcake for 1.5-m-long segments of drill cores from which the samples were taken, are given. For sample 2021-MAC-026, the Cs content is taken from Ramirez-Briones et al. (2025), while its Li content was not analyzed by these authors in this sample. Abbreviations: clinoptilolite (Cpt), heulandite (Hul), illite-montmorillonite (Ilt-Mnt), kaolinite (Kln), K-feldspar (Kfs), mica (Mca), mordenite (Mor), mutinaite (Mut), opal (Opl), plagioclase (Pl), quartz (Qz), rectorite (Rec), smectite (Sme), tridymite (Trd), and virgilite (Vir).

4.3. Textures

Under the microscope, most samples show a brecciated texture with glass clasts, zeolites, and other observable mineral elements such as mica crystal clasts embedded within a hypocrystalline matrix composed of volcanic glass, clays, silica, and zeolites (Fig. 9A). Some samples exhibit a perlitic texture within glass clasts, with concentric structures defined by fine-grained silica, clays, and zeolites as products of devitrification (Fig. 9B).

At the microscopic scale, zeolites commonly appear as radial aggregates of acicular crystals with lengths comprised between 100 and 350 μm (Fig. 9C) and spherulites with sizes mostly comprised between 100 and 200 μm (Fig. 9D). Zeolite aggregates often occur in the rock matrix (Figs. 9A, D) as well as filling micro-veins (Figs. 9E-G), interstitial spaces, and cavities (Figs. 9H-J). Spherulitic zeolites typically show Brewster crosses (Fig. 9D, I). In Figure 9J, an amygdala defined by multiple, intergrown radial zeolite aggregates is rimmed by a thin (<10 μm) coating of possible clay minerals, with the entire assemblage surrounded by glass. Finally, well-developed idiomorphic crystals with pseudo-rhombic dodecahedral and trapezohedral forms and sizes comprised in the range between 40 and 100 μm are locally observed (Figs. 9K-L).

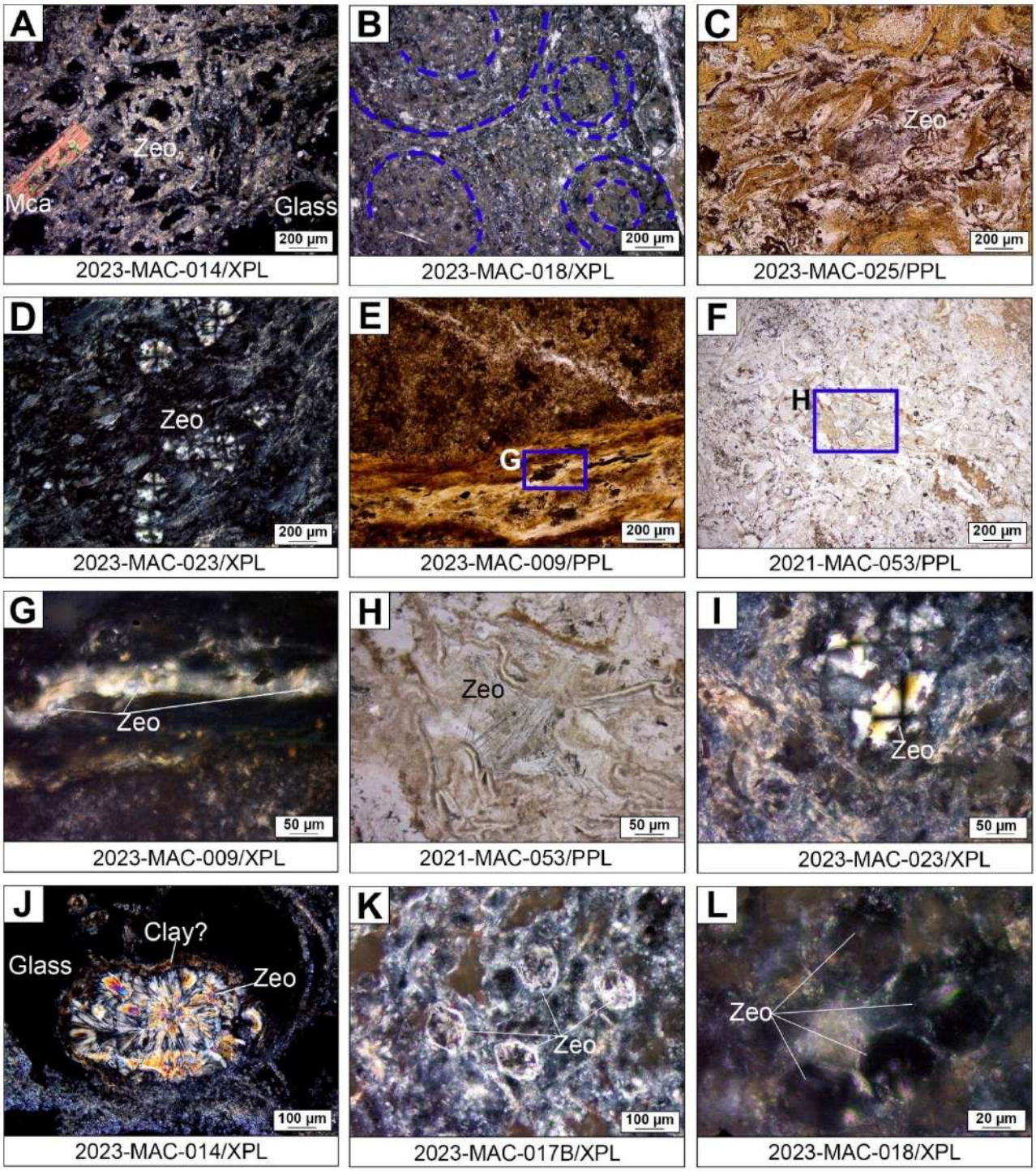

Figure 9. Microphotographs of zeolite-rich samples using plane-polarized (PPL) and crossed-polarized (XPL) transmitted light. **A)** Brecciated texture with rounded to subangular clasts of volcanic glass and a 300 µm-long biotite lath in a fine-grained matrix of silica, clays, and zeolites (zeolite + smectite/mixed-layer clay type). **B)** Perlitic texture in devitrified glass clasts (zeolite + smectite/mixed-layer clay type). **C)** Zeolites as radial aggregates of acicular crystals with lengths of ~300 µm (zeolite type). **D)** Spherulitic aggregates of zeolite (~ 200 µm) in an altered matrix

(zeolite + smectite/mixed-layer clay type). **E)** Irregular micro-veins cutting the very fine-grained and altered matrix (zeolite type). **F)** Fine-grained matrix composed of clays, silica, and zeolites cementing small and irregular clasts of devitrified glass (zeolite type). **G)** Micro-veins filled with subhedral zeolite radial aggregates (zeolite type). **H)** Radial (fan-shaped) acicular zeolite crystals filling cavities and interstitial space (zeolite type). **I)** Detail of spherulitic zeolite showing Brewster crosses (zeolite + smectite/mixed-layer clay type). **J**) Vesicle filled with radial zeolite coated with possible clays in a glass matrix (zeolite + smectite/mixed-layer clay type). **K)** Detail of equant (pseudo rhombododecahedral and pseudo trapezohedral) zeolite crystals ~50 µm in size (zeolite type). **L)** Detail of idiomorphic pseudo rhombododecahedral zeolite crystals within cavities in the matrix (zeolite + smectite/mixed-layer clay type).

5. DISCUSSION

5.1. Genesis of zeolites in the Macusani Volcanic Field

The mineralogical analysis of rock samples from the Falchani Lithium Project, as presented in this thesis, has confirmed the presence of zeolites. Potential zeolites identified through XRD analysis include mordenite, mutinaite, clinoptilolite, and heulandite. Of these, mordenite is the zeolite mineral most widely distributed among the studied samples, followed by mutinaite, while clinoptilolite and heulandite have only been identified in a few samples (Table 2). According to textural observations, zeolite minerals are authigenic in origin since they occur filling voids, amygdales, and veinlets (Fig. 10). In addition, clay minerals (kaolinite, smectite, and mixed-layer clays) were found to be also common in many of the analyzed samples. Of these, kaolinite and dioctahedral smectite (beidellite-montmorillonite) had been previously reported by Segovia-More et al. (2023) and Segovia-More (2024); in contrast, these authors did not report the presence of mixed-clays (illite-montmorillonite, rectorite). Segovia-More et al. (2023) and Segovia-More (2024) also determined an authigenic origin for the clay minerals at Falchani, based on key textural

features, such as rose-shaped aggregates of smectite formed replacements of feldspar grains.

Authigenic secondary minerals in volcanogenic sedimentary deposits can form through various processes including diagenesis, hydrolysis/hydrothermal alteration, and/or combinations thereof (e.g., Wohletz and Heiken 1992; Dill et al. 2000; Galán 2006; Reinoso-Carbonell et al. 2022; Fagel et al. 2024; Emproto et al. 2025). Zeolites represent some of the most commonly occurring authigenic silicates found in sedimentary rocks, particularly in altered vitric tuffs (Hay 1978; Weisenberger and Selbekk 2009; Suliman et al. 2025). Natural zeolites typically form through the alteration of volcanic glass and tuff by saline fluids (Jha and Singh 2016) and their crystallization is controlled by environmental temperature, pH, and chemical composition (Qinhua and Aizhen 1991). Mariner and Surdam (1970) found that zeolites such as mordenite and clinoptilolite developed from the alteration of volcanic glass in marine and lake environments with a pH between 7 and 9. The stability of zeolites is also strongly dependent on silica activity in the solution, such that most zeolites cannot form at low silica activities. Higher silica activity is related to a higher stability of these minerals (Fig. 10; Coombs et al. 1959).

Different genetic models have been proposed for the formation of zeolite minerals in lacustrine environments and depositional sequences, primarily aimed at explaining the occurrence of alkaline pH fluids and their interaction with glass-rich volcanogenic material. One commonly invoked model is the so-called closed hydrologic system diagenesis (CHSD), which operates in two main environments based on their tectonic and hydrogeological context (Surdam 1977): i) basins in arid/semi-arid block-faulted regions, where evaporation concentrates saline-alkaline fluids in playa-lake systems, promoting volcanic glass hydrolysis and zeolite formation through cation-exchange reactions that increase pH (Langella et al. 2001); and ii) rift valleys, characterized by lakes fed by

subsurface springs with high salinity and minimal sediment load, where deep water-rock interactions generate alkaline brines (Eugster 1970; Hardie and Eugster 1970; Langella et al. 2001). In both cases, evaporation exceeding precipitation leads to solute saturation, while the destabilization of volcanic glass produces an aluminosilicate gel phase that evolves into zeolites (de' Gennaro et al. 1988; Langella et al. 2001).

In closed hydrologic systems, evaporative concentration creates concentric salinity and pH gradients from basin margins to center, reflected in mineral zonation (Langella et al. 2001). As water volume decreases, progressive alteration of tephra occurs. Unaltered ash persists in peripheral dry areas, while inward, glass reacts forming aluminosilicate gels and eventually zeolites (Mariner and Surdam 1970; Langella et al. 2001). If salinity and alkalinity continue to increase, zeolites may transition to potassium feldspar in the most central zones (Langella et al. 2001).

In volcanogenic sedimentary Li deposits, the formation of zeolite through CHSD has been proposed as a key process in the development of secondary Li(B)-bearing minerals (Castor and Henry 2020; Putzolu et al. 2025a, b). Diagenetic alteration of intrabasinal volcanic glass under closed-hydrologic conditions led to the crystallization of Na zeolites and secondary K-feldspar in the McDermitt Caldera and Jadar volcanogenic sedimentary Li (Kadir et al. 2023; Putzolu et al. 2023a, 2025b). For instance, in the McDermitt Caldera, Li smectites are associated with nodular analcime, preserving relict volcanic glass textures (Benson et al. 2023). In contrast, the Jadar Deposit, jadarite formation follows hectorite alteration, accompanied by extensive zeolitization (Putzolu et al. 2025). These paragenetic sequences reflect the evolution of pore fluids from near-neutral to high-pH conditions, consistent with the CHSD model (Castor and Henry 2020).

In this line, zeolites from the Falchani Lithium Project likely formed during diagenetic or hydrothermal alteration of rhyolitic glass, leading to the deposition of amorphous silica as

metastable gels. These gels crystallized into smectites and zeolites (de' Gennaro et al. 1988; Langella et al. 2001; Castor and Henry 2020; Putzolu et al. 2025 a, b). The phases formed mostly in open spaces such as amygdales (Fig. 9J), veinlets (Figs. 9E, G), and more locally, in the form of replacement. The occurrence of zeolite as spherulites agrees with formation upon devitrification ("de-glassing") or recrystallization of poorly-crystalline, metastable silica polymorphs (Cox et al. 1979; Putzolu et al. 2025b).

The occurrence of different zeolite species and other authigenic minerals, in addition to zeolites, in the samples from the Falchani Lithium Project suggests varying post-deposition physicochemical conditions (Fig. 10A-C) along the volcanogenic sedimentary sequence and/or the time of formation. In this context, zeolites would have formed at higher pH and SiO_2 activities relative to kaolinite, smectite, and mixed-layer clays involving muscovite/illite (Fig. 10B-C). However, no clear temporal relationship between the authigenic phases can be established at this stage. Therefore, a precise trajectory in the evolution of post-depositional physicochemical conditions is hard to determine.

Regarding the various zeolite minerals, the stability and transformation of clinoptilolite to mordenite, or vice versa, are primarily controlled by alkalinity and temperature. According to Benning et al. (2000), clinoptilolite is more stable than mordenite when silica activity in the solution is low while mordenite predominates when there is more calcium in the solution and when silica is in an amorphous state (Fig. 10B). When clinoptilolite has more silicon compared to aluminum than mordenite, its stability fields shift; however, in most natural cases, mordenite tends to have more Si per formula unit than clinoptilolite (Tschernich 1992). Likewise, Figure 10C illustrates that the stability of mordenite is dictated by high SiO_2 activity at variable Na^+/Ca^{2+} ratios, in equilibrium with amorphous silica. In contrast, clinolptiloite, philipsite, heulandinte, and analcime are stable at progressively decreasing SiO_2 activities partially coinciding with chalcedony and quartz

saturation. On the other hand, higher Na^{+}/Ca^{2+} will favor the stability of philipsite and analcime over clinoptilolite and heulandite (Fig. 10C). The prevalence of mordenite over the other zeolite minerals such as clinoptilolite and heulandite in the studied samples from Falchani and its association with amorphous silica-saturated conditions indicate a very high SiO_2 activity ($\log(aSiO_2) > -3$) during zeolitization. This high availability of silica is likely related to the extreme high-silica and evolved nature of the volcanic material in the Falchani Lithium Project (Ramírez-Briones et al. 2025).

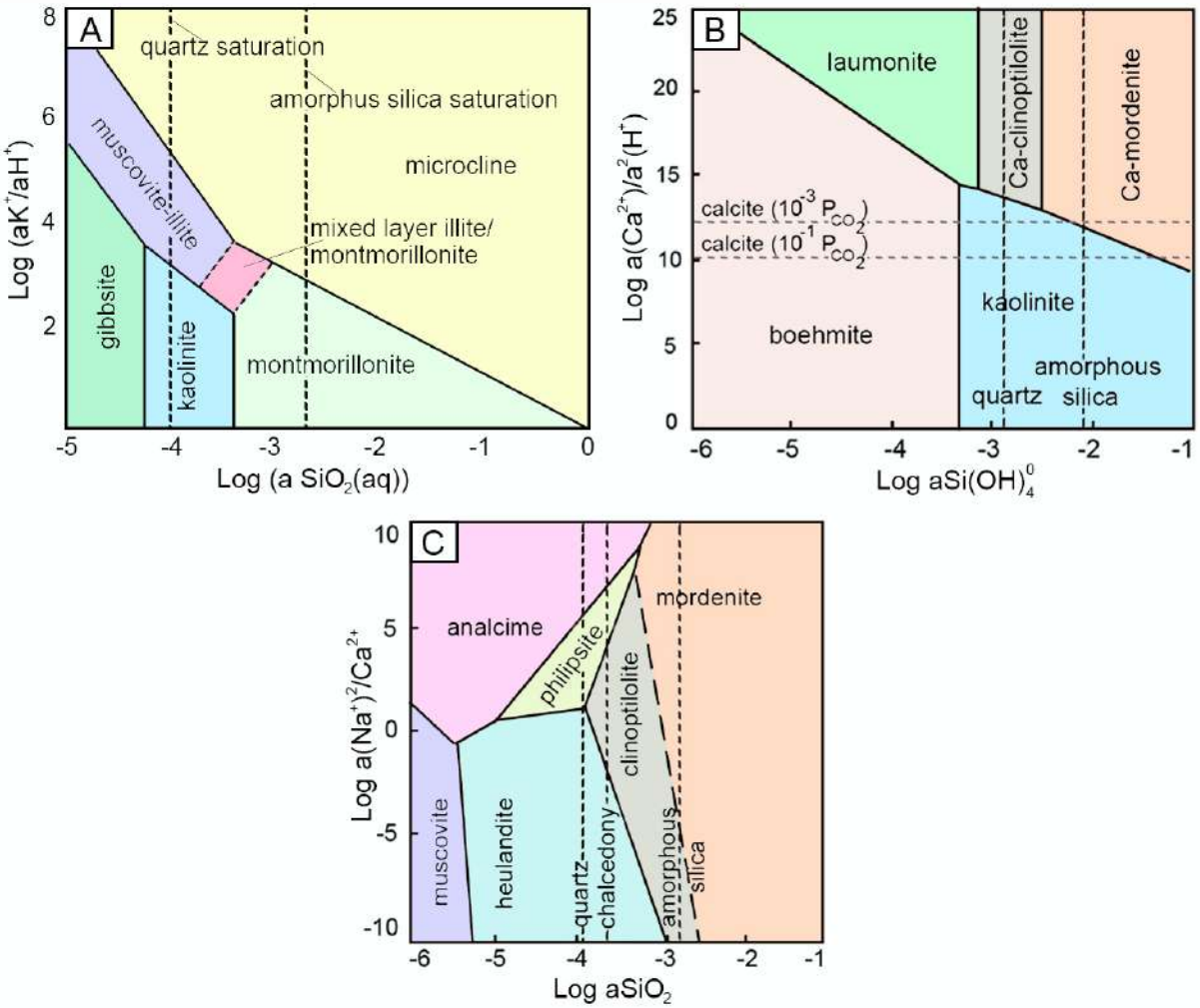

Figure 10. Stability diagrams including zeolites and other authigenic minerals found in the studied samples from the Falchani Lithium Project. **A)** Phase stability diagram for the Si-Al-K-O-H_2O system at 25°C, illustrating the equilibrium conditions of potassium-bearing minerals (microcline, illite/smectite mixed-layer clay, montmorillonite, gibbsite, and kaolinite) as functions of dissolved silica concentration (log a SiO_2(aq)) and potassium-to-hydrogen ion

activity ratio (log (aK^+/aH^+)). Modified from Aagaard and Helgeson (1983). **B)** Stability diagram for the Si-Al-Ca-K-Na-H_2O system at 125 °C showing the stability of Ca-zeolites (laumontite, clinoptilolite, and mordenite), as a function of silica activity and the Ca^{2+}/H^+ ratio in solution. Modified from Benning et al. (2000). **C)** Detail of mineral stability fields in the K_2O-Na_2O-CaO-Al_2O_3-SiO_2-H_2O system at 25°C, showing equilibrium phase relations under fixed cation activities (K^+ defined by K-feldspar, Ca^{2+} by tobermorite, and Al^{3+} by kaolinite solubility). Modified from Savage et al. (2007).

5.2. Are zeolites from the Falchani Lithium Project potentially enriched in Li and Cs*?*

The different secondary mineral associations identified in this thesis (Table 2; Fig. 8) are analyzed in relation to Li and Cs contents of the respective rock samples (Fig. 11). Across the sample set, Li contents (1,400-4,700 ppm) are in general less variable than Cs contents (300-9,600 ppm), which vary by nearly two orders of magnitude. Zeolite-smectite mixed-layer clay type samples show the widest ranges for both Li (1,400-4,700 ppm) and Cs (1,800-4,600 ppm) contents, including outliers, followed by zeolite type samples (Li = 1,400-3,600 ppm; Cs = 300-9,600 ppm). Zeolite + smectite/mixed layer + kaolinite subgroup type samples show wider dispersion for Cs (1,700-6,200 ppm) than for Li (1,800-2,700 ppm), similar to smectite/mixed layer clay dominant type (Li = 1,800-2,500 ppm; Cs = 2,700-5,000 ppm). In contrast, kaolinite subgroup dominant type samples show similar dispersion for Li (1,700-3,200 ppm) than for Cs (600-2,100 ppm).

Median Li values range from 2,100 ppm (kaolinite subgroup dominant type samples) to 2,700 ppm (zeolite + smectite/mixed-layer clay + kaolinite subgroup type samples). Median Cs values show a more significant variation from 1,960 ppm (zeolite + smectite/mixed-layer clay + kaolinite subgroup type samples) to 6,600ppm (zeolite type samples).

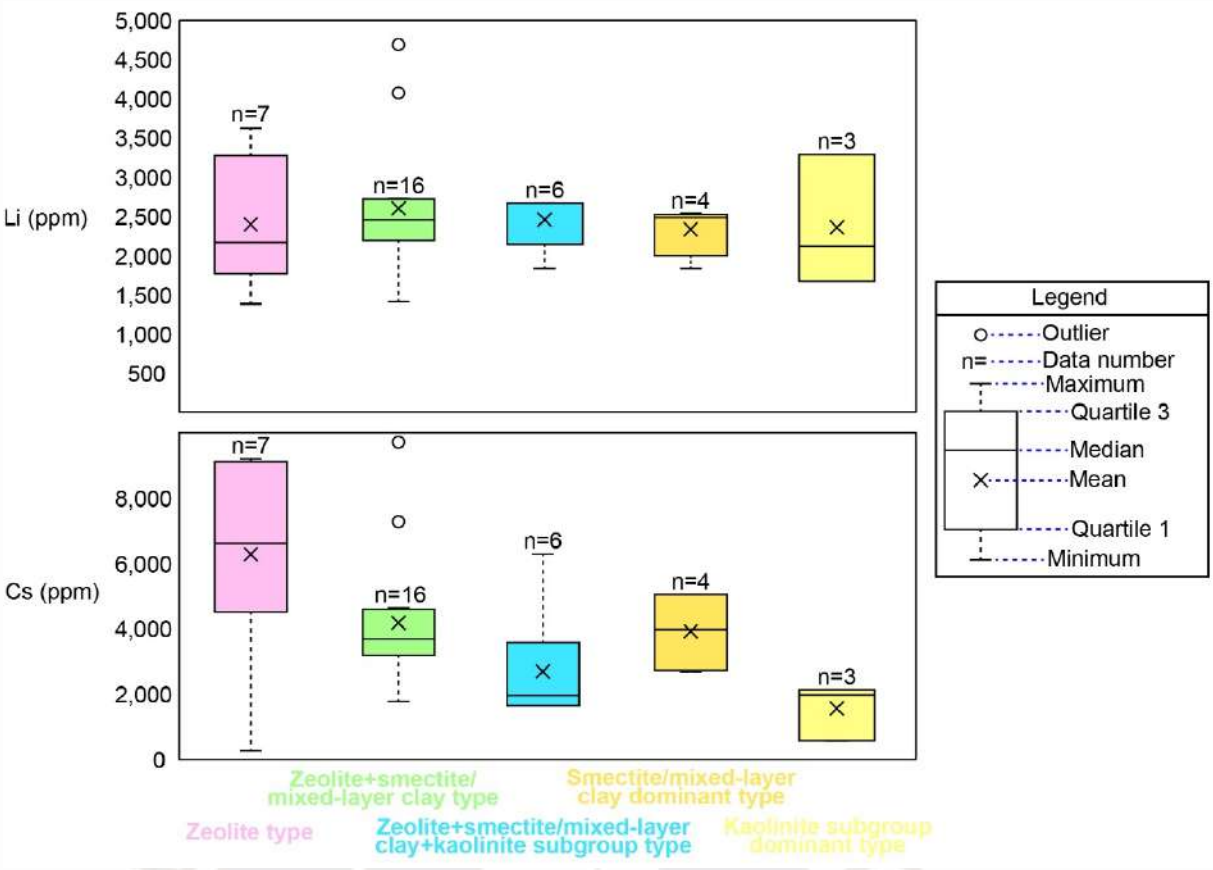

Figure 11. Box-and-whisker plots showcasing Li (ppm) and Cs (ppm) contents for the different mineralogical types.

The observed trends suggest that zeolite-rich samples have a stronger affinity for Cs than for Li, as expected (Flanigen 1991; Colella 1999; Munthali et al. 2015). The facts that zeolite-type samples have a distinctively high Cs contents regarding to the other mineralogical types strongly suggests that zeolites exerted a strong control on Cs enrichment at Falchani. This observation is also supported by the fact that Cs minerals have not been identified at Falchani neeither in this thesis nor in previous work (Segovia-More et al. 2023; Segovia-More 2024; Torró et al. 2025). The data also demonstrate that zeolite-rich samples are attractive for Li, with values that are comparable to samples dominated by clay minerals. Importantly, however, this does not establish a clear paragenetic control on Li grades, since the studied samples may contain Li minerals, as discussed below.

5.3. Economic potential of zeolite minerals in the Falchani Lithium Project and future research

In volcanogenic sedimentary Li deposits, the primary ore minerals are typically phyllosilicates (e.g., hectorite, tainiolite, cookeite) and, less frequently, borosilicates (e.g., jadarite) and phosphates (Putzolu et al. 2025a). However, at the Falchani Lithium Project, Li is mostly hosted in Li-F micas in samples in which this mineral is preserved, as well as associated to dioctahedral smectites (Segovia-More et al. 2023; Segovia-More 2024; Torró et al. 2025). The results in this thesis also usher in the possibility that Li could be associated to with zeolite minerals as well as mixed-layer clay minerals involving illite/muscovite and smectite interstratifications (Figs. 8, 11). Importantly, illitic, tainiolite-like clays are related with a twofold Li enrichment compared to precursor hectorite in the Thacker Pass deposit (Benson et al. 2023; Emproto et al. 2025). A more detailed study of the mixed-layer clays in the Falchani Lithium Project including XRD on oriented aggregates and TEM determinations is advised to constrain their exact nature and potential Li deportment.

The fact that zeolite-rich samples are, in general, Li-rich, with values comparable to the rest of the secondary mineralogical types (Fig. 11), does not directly imply that zeolites are major carriers of this metal. As determined by Segovia-More et al. (2023) and Torró et al. (2025), in samples of the kaolinite type, Li-F micas are the main lithium-bearing phases, as demonstrated by the insignificant proportion of Li exchanged during cation exchange analyses. In contrast, in smectite-rich samples, in which Li-F micas are almost absent, a dominant proportion of the Li (up to ~90 %) is exchanged under the same conditions, supporting the conclusion that Li is adsorbed onto or within the interlayer spaces in smectites (Segovia-More 2024). Equivalent cation exchange analyses should be performed on zeolite-rich samples to determine the Li and Cs uptake by these minerals, evaluate their

selectivity for different alkali metals, and assess their suitability for efficient extraction during metallurgical processing.

6. CONCLUSIONS

Five mineralogical types based on alteration assemblages have been defined in the studied samples from the Falchani Lithium Project: i) zeolite type; ii) zeolite + smectite/mixed-layer clay type; iii) zeolite + smectite/mixed-layer clay + kaolinite subgroup type samples; iv) smectite/mixed-layer clay dominant type; and v) kaolinite subgroup dominant type. Mordenite is the most abundant zeolite, followed by mutinaite, while clinoptilolite and heulandite have been identified only locally. Zeolites occur primarily as fillings of voids and fractures, and less commonly as spherulites and euhedral crystals.

The samples dominated by zeolite alteration are significant hosts for Li and Cs. In particular, the Li contents are comparable to those of samples with an alteration mineralogy dominated by clay minerals. However, further studies, likely involving cation exchange analysis, are required to determine whether Li is related to zeolites and/or to other minerals in the same samples, namely Li-F micas. In contrast, zeolite-type samples are strongly enriched in Cs compared to samples from the other mineralogical types, which strongly suggests that zeolites exerted a strong control on Cs enrichment at Falchani. In any case, the significant grades of Li and Cs in zeolite-bearing rocks confirm their economic relevance and enhance the overall resource value.

The crystallization of zeolite assemblages indicates that the original volcanic glass-rich tuffaceous sediments were altered by saline waters under alkaline pH conditions in a lacustrine environment. The prevalence of mordenite over other zeolite minerals, such as clinoptilolite and heulandite, in the studied samples indicates a very high SiO_2 activity during zeolitization, likely reflecting equilibrium conditions with amorphous silica. More

detailed studies are needed to determine textural relationships between authigenic minerals at Falchani to constrain the evolution of the alteration conditions.

7. REFERENCES

Aagaard P, Helgeson HC (1983) Activity/composition relations among silicates and aqueous solutions: II. Chemical and thermodynamic consequences of ideal mixing of atoms on homological sites in montmorillonites, illites, and mixed-layer clays. Clays Clay Miner 31(3):207-217. https://doi.org/10.1346/CCMN.1983.0310306

Aral H, Vecchio-Sadus A (2008) Toxicity of lithium to humans and the environment. A literature review. Ecotoxicol and Environ Saf 70(3):349–356. https://doi.org/10.1016/j.ecoenv.2008.02.026

Armbruster T, Gunter ME (2001) Crystal structures of natural zeolites. Rev Miner Geochem 45(1):1–67. https://doi.org/10.2138/rmg.2001.45.1

Barnes VE, Edwards G, Mclaughlin WA, Friedman I, Joenssu O (1970) Macusanite Occurrence, Age, and Composition, Macusani, Peru. Geol Soc Am Bull 81(5):1539–1546. https://doi.org/10.1130/0016-7606(1970)81[1539:MOAACM]2.0.CO;2

Belova TP (2019) Adsorption of heavy metal ions (Cu^{2+}, Ni^{2+}, Co^{2+} and Fe^{2+}) from aqueous solutions by natural zeolite. Heliyon 5(9):e02320. https://doi.org/10.1016/j.heliyon.2019.e02320

Benning LG, Wilkin RT, Barnes HL (2000) Solubility and stability of zeolites in aqueous solution: II. Calcic clinoptilolite and mordenite. Am Mineral 85(3-4):495–508. https://doi.org/10.2138/am-2000-0411

Benson TR, Coble MA, Dilles JH (2023) Hydrothermal enrichment of lithium in intracaldera illite-bearing claystones. Sci Adv 9(35):8183. https://doi.org/10.1126/sciadv.adh8183

Benson TR, Coble MA, Rytuba JJ, Mahood GA (2017) Lithium enrichment in intracontinental rhyolite magmas leads to Li deposits in caldera basins. Nat Commun 8(1):270. https://doi.org/10.1038/s41467-017-00234-y

Bibienne T, Magnan J-F, Rupp A, Laroche N (2020) From mine to mind and mobiles: Society's increasing dependence on lithium. Elements 16(4):265–270. https://doi.org/10.2138/GSELEMENTS.16.4.265

Bish DL, Ming DW (2001) Natural zeolites: Occurrence, properties, applications. Mineralogical Society of America, Washington

Bowell RJ, Lagos L, de los Hoyos CR, Declercq J (2020) Classification and characteristics of natural lithium resources. Elements 16(4):259–264. https://doi.org/10.2138/gselements.16.4.259

Bradley D, Jaskula B (2014) Lithium: for harnessing renewable energy. US Geological Survey. Mineral Resources Program Fact Sheet 2014-3035. https://doi.org/10.3133/fs20143035

Bradley DC, Stillings LL, Jaskula BW, Munk L, McCauley AD (2017a) Critical mineral resources of the United States—Economic and environmental geology and prospects for future supply. US Geological Survey Professional Paper 1802-K:K1–K21, Reston, Virginia. https://doi.org/10.3133/pp1802K

Bradley DC, McCauley AD, Stillings LM (2017b) Mineral-deposit model for lithium-cesium-tantalum pegmatites. US Geological Survey, Virginia, pp 1-48. https://doi.org/10.3133/sir20105070O

Breakiron LA, (2003) Cesium atomic clocks. http://www.tycho.usno.navy.mil.cesium.html. Accessed 27 May 2024

Breck DW (1974) Zeolite Molecular Sieves: Structure, Chemistry and Use. John Wiley and Sons, New York

Brenan JM, Neroda E, Lundstrom CC, Shaw HF, Ryerson FJ, Phinney DL (1998) Behaviour of boron, beryllium, and lithium during melting and crystallization constraints from mineral-melt partitioning experiments. Geochim Cosmochim Acta 62(12):2129–2141. https://doi.org/10.1016/S0016-7037(98)00131-8

Butterman WC, Brooks WE, Reese RG (2005) Mineral commodity profiles: Cesium. US Geological Survey. Open-File Report 2004-1432. https://doi.org/10.3133/ofr20041432

Cabot Specialty Fluids (2003) Statoil to Use Cabot Cesium Formate Fluids on Two Major High Pressure Gas Field https://investor.cabot-corp.com/news-releases/news-release-details/statoil-use-cabot-cesium-formate-fluids-two-major-high-pressure. Accessed 17 May 2024

Callot P (2008) La Formation Ayabacas (limite Turonien-Coniacien, Sud-Pérou): collapse sous-marin en réponse àl'amorce de l'orogenèse andine. Doctorat thesis, Université de Toulouse, Toulouse, France

Carlotto V, Carlier G, Van Heiningen P, Blake Hodgin E, Cárdenas J, Ligarda R, Cerpa L, Maqquera V (2023) Andean evolution, orogenic deformation and uplift of the Western Cordillera and Altiplano of southern Peru, northern Bolivia and Chile: Eocene-Oligocene lithospheric delamination. J South Am Earth Sci 128:104423. https://doi.org/10.1016/j.jsames.2023.104423

Castor SB, Henry CD (2020) Lithium-rich claystone in the McDermitt caldera, Nevada, USA: Geologic, mineralogical, and geochemical characteristics and possible origin. Minerals 10(1):68. https://doi.org/10.3390/min10010068

Černý P, Ercit TS (2005) The classification of granitic pegmatites revisited. Can Mineral 43(6):2005-2026. http://dx.doi.org/10.2113/gscanmin.43.6.2005

Charbonneau L (2003) IAEA director warns of "dirty bomb" risk: The Washington Post. https://www.washingtonpost.com/archive/politics/2003/03/12/iaea-director-warns-of-dirty-bomb-risk/fe1acca4-398a-454f-ba3b-1ee05f01cf04/. Accessed 17 May 2024

Cheilletz A, Clark AH, Farrar E, Arroyo Pauca G, Pichavant M, Sandeman HA (1992) Volcano stratigraphy and $^{40}Ar/^{39}Ar$ geochronology of the Macusani ignimbrite field: Monitor of the Miocene geodynamic evolution of the Andes of southeast Peru. Tectonophysics 205(1-3):307–327. https://doi.org/10.1016/0040-1951(92)90433-7

Chew DM, Pedemonte G, Corbett E (2016). Proto-andean evolution of the eastern Cordillera of Peru. Gondwana Res 35:59–78.http://dx.doi.org/10.1016/j.gr.2016.03.016

Chew DM, Schaltegger U, Košler J, Whitehouse MJ, Gutjahr M, Spikings RA, Miskovic A (2007) U-Pb geochronologic evidence for the evolution of the Gondwanan margin of the north-central Andes. Geol Soc Am Bull 119(5-6):697–711. https://doi.org/10.1130/B26080.1

Christiansen RL (2001) The Quaternary and Pliocene Yellowstone Plateau volcanic field of Wyoming, Idaho, and Montana. US Geological Survey Professional Paper 729-G, 145 p

Colella C (1999) Environmental applications of natural zeolitic materials based on their ion exchange properties. In: Natural Microporous Materials in Environmental Technology. Springer Netherlands, Dordrecht, pp 207–224

Conte N, Gómez JM, Díez E, Sáez P, Monago JI, Espinosa A, Rodríguez A (2022) Sequential separation of cobalt and lithium by sorption: Sorbent set selection. Sep Purif Technol 303:122199. https://doi.org/10.1016/j.seppur.2022.122199

Coombs DS, Alberti A, Armbruster T, Artioli G, Colella C, Galli E, Grice JD, Liebau F, Mandarino JA, Minato H, Nickel EH, Passaglia E, Peacor DR, Quartier S, Rinaldi R, Ross M, Sheppard RA, Tillmanns E, Vezzalini G (1998) Recommended nomenclature for zeolite minerals: report of the subcommittee on zeolites of the International Mineralogical Association, Commission on New Minerals and Mineral Names. Mineral Mag 62(4):533–571. https://doi.org/10.1180/002646198547800

Coombs DS, Ellis AJ, Fyfe WS, Taylor A (1959) The zeolite facies, with comments on the interpretation of hydrothermal syntheses. Geochim Cosmochim Acta 17(1-2):53-107. https://doi.org/10.1016/0016-7037(59)90079-1

Corma A (2003) State of the art and future challenges of zeolites as catalysts. J Catal 216(1-2):298–312. https://doi.org/10.1016/S0021-9517(02)00132-X

Cox KG, Bell JD, Pankhurst RJ (1979) The interpretation of igneous rocks. Chapman and Hall, London, England https://doi.org/10.1007/978-94-017-3373-1

de'Gennaro M, Colella C, Franco E, Stanzione D (1988) Hydrothermal conversion of trachytic glass into zeolite. 1. Reactions with deionized water. Neues Jahrb Mineral Monatsh 149–158

Dill HG, Bosse HR, Kassbohm J (2000) Mineralogical and chemical studies of volcanic-related argillaceous industrial minerals of the Central American Cordillera (Western El Salvador). Econ Geol 95(3):517–538. https://doi.org/10.2113/gsecongeo.95.3.517

Emproto C, Benson TR, Gagnon CA, Baek W, Ibarra D, Simon AC (2025) Clay chemistry of the Thacker Pass deposit, Nevada: implications for the formation of high-grade volcano-sedimentary lithium resources. Econ Geol *in press*. https://doi.org/10.5382/econgeo.5155

Eugster HP (1970) Chemistry and origin of the brines of Lake Magadi, Kenya. Mineral Soc Am Spec Pap 3:215-235

European Commission (2023) Study on the critical raw materials for the EU (final report). European Commission, Brussels, 158p. https://data.europa.eu/doi/10.2873/725585

Evans K (2014) Lithium. In: Gunn G (ed) Critical Metals Handbook. John Wiley & Sons, Nottingham, pp 230–260. https://doi.org/10.1002/9781118755341.ch10

Fagel N, Israde-Alcántara I, Safaierad R, Rantala M, Schmidt S, Lepoint G, Pellenard P, Mattielli N, Metcalfe S (2024) Environmental significance of kaolinite variability over the last centuries in crater lake sediments from Central Mexico. Appl Clay Sci 247:107211. https://doi.org/10.1016/j.clay.2023.107211

Falkowski S, Ehlers TA, McQuarrie N, Glover CO, Perez ND, Parks VMB (2023) Exhumation and incision of the eastern Central Andes, southern Peru: Low-temperature thermochronology observations. Earth Planet Sci Lett 620:118299. https://doi.org/10.1016/j.epsl.2023.118299

Ferreira DR, Phillips GD, Baruah B (2021) A comparison of the adsorption of cesium on zeolite minerals vs vermiculite. Clays Clay Miner 69(6):663–671. https://doi.org/10.1007/s42860-021-00150-9

Flanigen EM (1991) Zeolites and molecular sieves: A historical perspective. In: Van Bekkum H, Flanigen EM, Jansen JC (eds) Introduction to Zeolite Science and Practice. Elsevier, Amsterdam. https://doi.org/10.1016/S0167-2991(08)63599-5

French, Bevan M, Jezek, PA, Appleman DE (1978) Virgilite: A new lithium aluminum silicate mineral from the Macusani glass, Peru. Am Mineral 63(5-6):461–465

Frenzel M, Baumgartner R, Tolosana-Delgado R, Gutzmer J (2024) Geometallurgy: Present and future. Elements 19(6):345–351. https://doi.org/10.2138/gselements.19.6.345

Frost CD, Frost BR, Beard JS (2016) On silica-rich granitoids and their eruptive equivalents. Am Mineral 101(6):1268–1284. https://doi.org/10.2138/am-2016-5307

Galán E (2006) Genesis of clay minerals. In: Bergaya F, Theng BKG, Lagaly G (eds) Handbook of clay science, 1st edn. Elsevier, Amsterdam, pp 1129–1161

Garrett DE (2004) Part 1 – Lithium. In: Garrett DE (ed) Handbook of Lithium and Natural Calcium Chloride. Their Deposits, Processing, Uses and Properties. Academic Press, Elsevier, Amsterdam, pp 1–235 https://doi.org/10.1016/B978-012276152-2/50037-2

GEOCATMIN (2024) Consulta al Sistema de Información Geológico y Catastral Minero. In: INGEMMET. https://geocatmin.ingemmet.gob.pe/geocatmin_v3/. Accessed 1 Jun 2024

Giannetto G, Montes A, Rodríguez G (2000) Zeolitas: Características, Propiedades y Aplicaciones. Editorial Innovación Tecnológica, Facultad de Ingeniería, UCV, Caracas

Goldschmidt VM (1954) Geochemistry. Oxford University Press, London

Government of Canada (2024) The Canadian critical minerals strategy, from exploration to recycling: powering the green and digital economy for Canada and the world. https://www.canada.ca/en/campaign/critical-minerals-in-canada/canadian-critical-minerals-strategy.html. Accessed 27 May 2024

Grew ES (2020) The minerals of lithium. Elements 16(4):235–240. https://doi.org/10.2138/gselements.16.4.235

Groves DI, Zhang L, Groves IM, Sener AK (2022) Spodumene: The key lithium mineral in giant lithium-cesium-tantalum pegmatites. Acta Petrol Sin 38(1):1–8. https://doi.org/10.18654/1000-0569/2022.01.01

Hardie LA, Eugster HP (1970) The evolution of closed basin brines. Mineral Soc Am Spec Pap 3:273- 290

Hay RL (1978) Zeolites in sedimentary rocks. In: Middleton GV, Church MJ, Coniglio M, Hardie LA, Longstaffe FJ (eds) Encyclopedia of Earth Science. Springer Netherlands, Dordrecht, pp 1281–1283. https://doi.org/10.1007/978-1-4020-3609-5_251

Hernandez MA, Pestryakov A, Portillo R, Salgado MA, Rojas F, Rubio E, Ruiz S, Petranovskii V (2015) CO_2 Sequestration by natural zeolite for greenhouse effect control. Procedia Chem 15:3–41. https://doi.org/10.1016/j.proche.2015.10.006

Hey MH (1930) Studies on the zeolites. Part I. General review. Mineral Mag J M Soc 22(131):422–437. https://doi.org/10.1180/minmag.1930.022.131.04

Hofmann AW (1988) Chemical differentiation of the earth: the relationship between mantle, continental crust, oceanic crust. Earth Planet Sci Lett 90(3):297–314. http://dx.doi.org/10.1016/0012-821X(88)90132-X

Hoyer M, Kummer NA, Merkel B (2015) Sorption of lithium on bentonite, kaolin and zeolite. Geosciences 5(2):127-140. https://doi.org/10.3390/geosciences5020127

Huang XL, Wang RC, Chen XM, Hu H, Liu CS (2002) Vertical variations in the mineralogy of the Yichun topazlepidolite granite, Jiangxi Province southern China. Can Mineral 40(4):1047–1068. https://doi.org/10.2113/gscanmin.40.4.1047

IEA (2021) The Role of Critical Minerals in Clean Energy Transitions. Paris, International Energy Association. https://www.iea.org/reports/the-role-of-critical-minerals-in-clean-energy-transitions. Accessed 26 May 2024

IEA (2023) 2023 DOE Critical Materials List. https://www.iea.org/policies/17976-2023-doe-critical-materials-list. Accessed 27 June 2024

Inglezakis VJ, Kudarova A, Guney A, Kinayat N, Tauanov Z (2023) Efficient mercury removal from water by using modified natural zeolites and comparison to commercial adsorbents. Sustain Chem Pharm 32:101017. https://doi.org/10.1016/j.scp.2023.101017

Jensen NL (1985) Cesium. In: Knoerr AW (ed) Mineral Facts and Problems. US Bureau of Mines Bulletin, Washington, pp 133–138

Jha B, Singh DN (2016) Basics of Zeolites. In: Advanced Structured Materials. Springer Singapore, Singapore, pp 5–31

Jiménez-Reyes M, Almazán-Sánchez PT, Solache-Ríos M (2021) Radioactive waste treatments by using zeolites. A short review. J Environ Radioact 233:106610. https://doi.org/10.1016/j.jenvrad.2021.106610

Johan E, Toshio Y, Moses WM, Ponyadira KC, Hiromichi A, Naoto M (2015) Natural zeolites as potential materials for decontamination of radioactive cesium. Procedia Environ Sci 28:52–56. https://doi.org/10.1016/j.proenv.2015.07.008

Jowitt SM, McNulty BA (2021) Battery and energy metals: Future drivers of the minerals industry? SEG Discovery (127):11–18. https://doi.org/10.5382/2021-127.fea-01

Kadir S, Külah T, Erkoyun H, Helvacı C, Eren M, Demiral B (2023) Mineralogy, geochemistry, and genesis of lithium-bearing argil laceous sediments associated with the Neogene Bigadiç borate deposits, Balıkesir, western Anatolia, Türkiye. Appl Clay Sci 242:107015. https://doi.org/10.1016/j.clay.2023.107015

Kay SM, Mpodozis C (2020) The Andes. In: Alderton D, Elias SA (eds) Encyclopedia of Geology, 2nd edn. Academic Press, Elsevier, pp 1–15. https://doi.org/10.1016/B978-0-08-102908-4.00173-9

Kesler SE, Gruber PW, Medina PA, Keoleian GA, Everson MP, Wallington, TJ (2012) Global lithium resources: Relative importance of pegmatite, brine, and other deposits. Ore Geol Rev 48:55–69. https://doi.org/10.1016/j.oregeorev.2012.05.006

Klein C, Hurlburt CS, Dana JD (1982) Manual de Mineralogía. Basado en la obra de J. D. Dana. Reverté, Barcelona

Kontak DJ, Clark AH, Farrar E, Archibald DA, Baadsgaard H (1990) Late Paleozoic-early Mesozoic magmatism in the Cordillera de Carabaya, Puno, southeastern Peru: Geochronology and petrochemistry. J South Am Earth Sci 3(4):213–230. https://doi.org/10.1016/0895-9811(90)90004-K

Langella A, Cappelletti P, de Gennaro R (2001) Zeolites in closed hydrologic systems. Rev Mineral Geochem 45(1):235-260. https://doi.org/10.2138/rmg.2001.45.7

Laubacher G (1978) Estudio geológico de la región norte del lago Titicaca. Instituto Geológico, Minero y Metalúrgico, 120 pp

Lee J, Bazilian M, Sovacool B, Hund K, Jowitt SM, Nguyen TP, Månberger A, Kah M, Greene S, Galeazzi C, Awuah-Offei K, Moats M, Tilton J, Kukoda S (2020) Reviewing the material and metal security of low-carbon energy transitions. Renew Sustain Energy Rev 124:109789. https://doi.org/10.1016/j.rser.2020.109789

Linnen RL, Lichtervelde MV, Černý P (2012) Granitic Pegmatites as Sources of Strategic Metals. Elements 8(4):275–280. https://doi.org/10.2113/gselements.8.4.275

London D (2005) Geochemistry of alkali and alkaline earth elements in ore-forming granites, pegmatites and rhyolites. In: Linnen RL, Samson IM (eds) Rare Element Geochemistry and Mineral Deposits. Geological Association of Canada Short Course Notes 17, pp 17-43

London D (2008) Pegmatites. Canadian Mineralogist, Canada

London D (2017) Reading Pegmatites: Part 3—What Lithium Minerals Say. Rocks Miner 92(2):144–157. https://doi.org/10.1080/00357529.2017.1252636

López JC (1996) Geología del cuadrángulo de Nuñoa. Hoja 29-u. Instituto Geológico, Minero y Metalúrgico, 171 pp

Loveday D, Kasrtick M (2023) Technical Report and Mineral Resource Estimate - Falchani Property. https://americanlithiumcorp.com/wp-content/uploads/2025/05/Falchani-NI43-101_Technical_Report_Final_12-14-23.pdf. Accessed 26 May 2024

MacEwan DMC, Ruiz-Amil A (1975) Interstratified clay minerals. In: Gieseking JE (ed) Soil Components. Springer, Berlin, Heidelberg, pp 265–334. https://doi.org/10.1007/978-3-642-65917-1_8

Mariner RH and Surdam RC (1970) Alkalinity and formation of zeolites in saline, alkaline lakes. Science 170:977–980. https://doi.org/10.1126/science.170.3961.977

Marschall HR, Wanless VD, Shimizu N, Pogge von Strandmann PAE, Elliott T, Monteleone BD (2017) The boron and lithium isotopic composition of mid-ocean ridge basalts and the mantle. Geochim Cosmochim Acta 207:102–138. https://doi.org/10.1016/j.gca.2017.03.028

McDonough WF (2003) Compositional model for the earth's core. In: Holland HD, Turekian KK (eds) Treatise on Geochemistry, 2nd edn. Elsevier, pp 547–568. https://doi.org/10.1016/B0-08-043751-6/02015-6

Michaud JAS, Pichavant M, Villaros A (2021) Rare elements enrichment in crustal peraluminous magmas: insights from partial melting experiments. Contrib Mineral Petrol 176(11):96. https://doi.org/10.1007/s00410-021-01855-9

Mišković A, Spikings RA, Chew DM, Košler J, Ulianov A, Schaltegger U (2009) Tectonomagmatic evolution of Western Amazonia: Geochemical characterization and

zircon U-Pb geochronologic constraints from the Peruvian Eastern Cordilleran granitoids. Geol Soc Am Bull 121(9-10):1298–1324. https://doi.org/10.1130/B26488.1

Munthali MW, Johan E, Aono H, Matsue N (2015) Cs^{+} and Sr^{2+} adsorption selectivity of zeolites in relation to radioactive decontamination. J Asian Ceram Soc 3(3):245–250. https://doi.org/10.1016/j.jascer.2015.04.002

National Safety Council (2003) Major uses of radioisotopes. https://hhs.iowa.gov/media/7493/download?inline. Accessed 26 May 2024

Newell ND (1949) Geology of the Lake Titicaca region, Peru and Bolivia. In: Geological Society of America Memoirs, Geological Society of America, Baltimore, 111 p

Noble DC, Vogel TA, Peterson PS, Landis GP, Grant NK, Jezek P, McKee EH (1984) Rare-element-enriched, S-type ash-flow tufts containing phenocrysts of muscovite, andalusite, and sillimanite, southeastern Peru. Geology 12(1):35-39. https://doi.org/10.1130/0091-7613(1984)122.0.CO;2

Norton JJ (1973) Lithium, cesium, and rubidium. In: Brobst DA, Pratt WP (eds) The rare alkali metals. US Geological Survey Professional, pp 365–378

Nunes-Pereira J, Lopes AC, Costa CM, Silva M.M, Lanceros-Méndez S (2012) Microporous poly (vinylidene fluoride – trifluoroethylene)/zeolite membranes for lithium-ion battery applications. Procedia Eng 44:983–984. https://doi.org/10.1016/j.proeng.2012.08.645

Nupen S (2019) Mineral Resource Estimates for the Falchani Lithium Project in the Puno District of Peru. Bryanston, 72 pp

Pabalan RT, Bertetti FP (2001) Cation-exchange properties of natural zeolites. Rev Miner Geochem 45(1):453–518. https://doi.org/10.2138/rmg.2001.45.14

Panca F, Bahlburg H, Cárdenas J, Berndt J, Lünsdorf NK, Gerdes A (2024) Sedimentology, geochronology and provenance of the late Permian and Triassic Mitu Group in Peru—The evolution of continental facies along a transform margin. Basin Res 36(2):e12864. https://doi.org/10.1111/bre.12864

Perez ND, Horton BK (2014) Oligocene-Miocene deformational and depositional history of the Andean hinterland basin in the northern Altiplano plateau, southern Peru. Tectonics 33(9):1819–1847. https://doi.org/10.1002/2014TC003647

Perez ND, Horton BK, Carlotto V (2016a) Structural inheritance and selective reactivation in the central Andes: Cenozoic deformation guided by pre-Andean structures in southern Peru. Tectonophysics 671:264–280. https://doi.org/10.1016/j.tecto.2015.12.031

Perez ND, Horton BK, McQuarrie N, Stübner K, Ehlers TA (2016b) Andean shortening, inversion and exhumation associated with thin- and thick-skinned deformation in southern Peru. Geol Mag 153(5-6):1013–1041. https://doi.org/10.1017/S0016756816000121

Pichavant M, Erdmann S, Kontak DJ, Michaud JAS, Villaros A (2024) Trace element partitioning in strongly peraluminous rare-metal silicic magmas – Implications for fractionation processes and for the origin of the Macusani Volcanics (SE Peru) Geochim Cosmochim Acta 365:229-252. https://doi.org/10.1016/j.gca.2023.11.021

Pichavant M, Kontak DJ, Briqueu L, Valencia Herrera J, Clark AH (1988) The Miocene-Pliocene Macusani Volcanics, SE Peru - II. Geochemistry and origin of a felsic peraluminous magma. Contrib Mineral Petrol 100(3):325–338. https://doi.org/10.1007/BF00379742

Pichavant M, Valencia Herrera J, Boulmier S, Briqueu L, Joron JL, Juteau M, Marin L, Michard A, Sheppard AMF, Treuil M, Vernet M (1987) The Macusani glasses, SE Peru:

evidence of chemical fractionation in peraluminous magmas. In: Mysen BO (ed) Magmatic processes, physicochemical principles. Geochem Soc Special Publ 1:359–373.

Pogge von Strandmann PAE, Kasemann SA, Wimpenny JB (2020) Lithium and lithium isotopes in Earth's surface cycles. Elements 16(4):253–258. https://doi.org/10.2138/gselements.16.4.253

Putzolu F, Armstrong RN, Benson TR, Boutt DF, Butler KL, Dolgopolova A, Herrington RJ, Ibarra DE, Munk LA (2025a) Volcano-sedimentary deposits: Overview of an emerging type of lithium resource. Econ Geol 120(3):541–573 https://doi.org/10.5382/econgeo.5135

Putzolu F, Armstrong RN, Boyce AJ, Hepburn LE, Bompard N, Najorka J, Lefebvre-Desanois M, Milton AJ, Salge T, Erak D, Abad I, Herrington RJ (2025b) Origin of the Jadar Volcano-Sedimentary Li-B Deposit, Serbia. Econ Geol 120(3):599–625. https://doi.org/10.5382/econgeo.5132

Qinhua X, Aizhen Y (1991) Hydrothermal synthesis and crystallization of zeolites. Prog Cryst Growth Charact Mater 21(1-4):29–70. https://doi.org/10.1016/0960-8974(91)90007-Y

Ramirez-Briones JS, Torró, L, Chiaradia M, Laurent O, Mandrou S, Tavazzani L, Chelle-Michou C, Vallance J, Baby P (2025) Petrogenesis of volcanogenic sedimentary lithium ore in the Neogene Macusani Volcanic Field, Puno, Peru. J Petrol 66(5): egaf041. https://doi.org/10.1093/petrology/egaf041

Reinoso Carbonell VV, Collo G, Wunderlin CA, Alasino PH, Ciccioli PL, Rocher S, Maza S (2022) Clay mineral assemblages as indicators of paleoenvironmental and diagenetic dynamics in the Neogene Fiambalá Basin, NW Argentina. J South Am Earth Sci 118:103949. https://doi.org/10.1016/j.jsames.2022.103949

Reynold RC (1980) Interstratified clay minerals. In: Brindley GW, Brown G (eds) Crystal structures clay minerals X-ray identification. Mineralogical Society, London, pp 249–303

Rocher P (1995) Mémento roches et minéraux industriels. Zéolites naturelles. Bureau de Recherches Géologiques et Minières Rapport BRGM R 38759, 72 pp. https://www.mineralinfo.fr/sites/default/files/documents/2021-03/zeolite_rr-38759-fr_1995.pdf

Rodríguez R, Choquehuanca S, Sánchez E, Fabián C, del Castillo B (2021) Geología de los cuadrángulos de Macusani (hojas 29v1, 29v2, 29v3, 29v4) y Limbani (hojas 29-1, 29-2, 29-3, 29-4). Instituto Geológico, Minero y Metalúrgico, Boletin Serie L4, 82 pp

Sanandres-Flores MK (2024) $^{40}Ar/^{39}Ar$ geochronology of the Lithium-rich Tuff in the Macusani Volcanic Field, Oriental Cordillera, Peru. Undergraduated thesis, Pontificia Universidad Católica del Perú, Facultad de Ciencias e Ingeniería, Lima, Peru. http://hdl.handle.net/20.500.12404/28843

Sandeman HA, Clark AH (2003) Glass-rich, cordierite–biotite rhyodacite, Valle Ninahuisa, Puno, SE Peru: Petrological evidence for hybridization of 'Lachlan S-type' and potassic mafic magmas. J Petrol 44(2):355–385. https://doi.org/10.1093/petrology/44.2.355

Sandeman HA, Clark AH, Farrar E, Arroyo-Pauca G (1996) A critical appraisal of the Cayconi Formation, Crucero Basin, southeastern Peru. J South Am Earth Sci 9(5-6):381–392. https://doi.org/10.1016/s0895-9811(96)00021-1

Sandeman HA, Clark AH, Farrar E, Arroyo-Pauca G (1997) Lithostratigraphy, petrology and $^{40}Ar/^{39}Ar$ geochronology of the Crucero Supergroup, Puno Department, SE Peru. J South Am Earth Sci 10(3):223– 245. https://doi.org/10.1016/S0895-9811(97)00023-0

Sauzéat L, Rudnick RL, Chauvel C, Garçon M, Tang M (2015) New perspectives on the Li isotopic composition of the upper continental crust and its weathering signature. Earth Planet Sci Lett 428:181–192. https://doi.org/10.1016/j.epsl.2015.07.032

Savage D, Walker C, Arthur R, Rochelle C, Oda C, Takase H (2007) Alteration of bentonite by hyperalkaline fluids: A review of the role of secondary minerals. Phys Chem Earth 32(1-7):287–297. https://doi.org/10.1016/j.pce.2005.08.048

Schlumberger Corporation (2002) Oilfield glossary http://www.glossary.oilfield.slb.com. Accessed 26 May 2024

Segovia-More MK (2024) Mineralogy of the lithium-rich tuff in the Macusani Volcanic Field, Cordillera Oriental, southern Peru. Undergraduated thesis, Pontificia Universidad Católica del Perú, Facultad de Ciencias e Ingeniería, Lima, Peru. https://tesis.pucp.edu.pe/repositorio/handle/20.500.12404/13060

Segovia-More MK, Torró L, Villanova-De-Benavent C, Ramírez-Briones JS, Vallance JFV, Monier L, Laurent O, Salvi S, Baby PJF, Proenza JA (2023) High-resolution mineralogy of Lithium-rich Tuff from the Macusani Volcanic Field, Puno, Peru. Proceedings of the 17th SGA Biennial Meeting, pp 96-99

Sempere T, Acosta H, Carlotto V (2004) Estratigrafía del Mesozoico y Paleógeno al norte del Lago Titicaca. Sociedad Geológica del Perú, Publicación Especial 5:81-103

Sempere T, Carlier G, Soler P, Fornari M, Carlotto V, Jacay J, Arispe O, Néraudeau D, Cárdenas J, Rosas S, Jiménez N (2002) Late Permian-Middle Jurassic lithospheric thinning in Peru and Bolivia, and its bearing on Andean-age tectonics. Tectonophysics 345(1-4):153–181. https://doi.org/10.1016/S0040-1951(01)00211-6

Shanghai Metals Market (2025) Cesium Carbonate（Cs_2CO_3≥99%） Price, USD/kg. https://www.metal.com/Other-Minor-Metals/202012250002. Accessed 1 August 2025

Shekarchi M, Ahmadi B, Azarhomayun F, Shafei B, Kioumarsi M (2023) Natural zeolite as a supplementary cementitious material. Constr Build Mater 409:133766. https://doi.org/10.1016/j.conbuildmat.2023.133766

Sherry HS (1969) The ion-exchange properties of the zeolites. In: Marinsky JA (ed) Ion exchange. Marcel Dekker, New York, pp 89-133

Singh DN, Kolay PK (2002) Simulation of ash water interaction and its influence on ash characteristics. Prog Energy Combust Sci 28(3):267–299. https://doi.org/10.1016/S0360-1285(01)00018-1

Smith JV (1984) Definition of a zeolite. Zeolites 4(4):309–310. https://doi.org/10.1016/0144-2449(84)90003-4

Spikings R, Reitsma MJ, Boekhout F, Mišković A, Ulianov A, Chiaradia M, Gerde A, Schaltegger U (2016) Characterization of Triassic rifting in Peru and implications for the early disassembly of western Pangaea. Gondwana Res 35:124–143. https://doi.org/10.1016/j.gr.2016.02.008

Suliman TA, Hong H, Hassan MA, Yong L, Liu C, Yunusa A, Salim A, Algeo TJ (2025) Constraints of groundwater and hydrothermal activity on formation of zeolites in alkaline basalts (Gedaref, eastern Sudan). Ore Geol Rev 185:106784. https://doi.org/10.1016/j.oregeorev.2025.106784

Surdam RC (1977) Zeolites in closed hydrologic system. In: Mumpton FA (ed) Mineralogy and Geology of Natural Zeolites. Mineralogical Society of America, Washington DC, pp 65-91

Tomascak PB, Magna T, Dohmen R (2016) Advances in Lithium Isotope Geochemistry. Springer, Switzerland. https://doi.org/10.1007/978-3-319-01430-2

Torró L, Ramirez-Briones JS, Sanandres-Flores MK, Monnier L, Villanova-de-Benavent C, Zanetti KA, Konrad K, Vallance J, Laurent O, Salvi S, Baby P, Proenza JA, Bachmann O, Nieto F (2025) Lithium mica clasts document magmatic evolution prior to eruption in the Macusani Volcanic Field in Peru. Sci Rep 15(1):13023. https://doi.org/10.1038/s41598-025-96173-6

Trading Economics (2023) Lithium. https://tradingeconomics.com/commodity/lithium. Accessed 27 May 2024

Trading Economics (2025) Lithium. https://tradingeconomics.com/commodity/lithium. Accessed 19 August Trading Economics (2025) Lithium 2025

Trueman D, Downing B, Richards T (2020) Cesium Deposits. Explore 188:5–12 https://doi.org/10.70499/wqni7190

Tschernich RW (1992) Zeolites of the World. Geoscience Press, Phoenix

Ullrich TD (2006) Report on $^{40}Ar/^{39}Ar$ geochronological analysis: Unpublished report to Bear Creek Mining, 12 pp

United States Geological Survey (2025). Mineral Commodity Summaries 2025. https://doi.org/10.3133/mcs2025

Valencia J, Arroyo G (1985) Geochemical aspects of the uranium occurrences of Macusani, Puno (Peru). International Atomic Energy Agency, Uranium Deposits in Volcanic Rocks, Proceedings of a Technical Committee Meeting, pp 275–288

Watari, T, Nansai, K, Nakajima K (2020) Review of critical metal dynamics to 2050 for 48 elements. Resour Conserv Recycl 155:104669. https://doi.org/10.1016/j.resconrec.2019.104669

Weisenberger T, Selbekk RS (2009) Multi-stage zeolite facies mineralization in the Hvalfjördur area, Iceland. Int J Earth Sci 98(5):985–999. https://doi.org/10.1007/s00531-007-0296-6

White DE, Fournier RO, Muffler LJP, Truesdell AH (1975) Physical results of research drilling in thermal areas of Yellowstone National Park, Wyoming. US Geological Survey Professional Paper 892

Wohletz K, Heiken G (1992) Volcanology and geothermal energy. University of California Press, Berkeley

Wörner G, Schildgen TF, Reich M (2018) The Central Andes: Elements of an extreme land. Elements 14(4):225–230. https://doi.org/10.2138/gselements.14.4.225

APPENDICES

Appendix A: List of samples

Sample	Unit	DDH	Depth (m)	Geographical coordinates*		Field description
				Latitude - S	Longitude - W	
2021-MAC-026	Lithium Rich Tuff	-	-	14º 00' 6.546"	82º 40' 47.260"	White fine-grained tuff hosting clasts.
2021-MAC-053	Lithium Rich Tuff	PCHAC-32-TNW	Approx. 115.00	14º 00' 14.930"	82º 40' 58.285"	Disaggregated material, rich in clay minerals. Li-rich.
2023-MAC-001	Upper Breccia	PCHAC-14-TW	10.40	13º 59' 56.098"	82º 40' 33.521"	Defined as “single mineral” by the company.
2023-MAC-002	Lower Breccia	PCHAC-14-TW	90.30	13º 59' 56.088"	82º 40' 35.048"	Defined as “single mineral” by the company.
2023-MAC-005	Lower Breccia	PCHAC-14-TW	96.90	13º 59' 56.087"	82º 40' 35.174"	Oxidized sample, with brown tarnish and possible veins filled with well crystallized white and brown minerals.
2023-MAC-006	Lower Breccia	PCHAC-14-TW	104.70	13º 59' 56.086"	82º 40' 35.323"	Fine grain, light weight.
2023-MAC-007	Lower Breccia	PCHAC-14-TW	222.10	13º 59' 56.070"	82º 40' 37.567"	Fine-grained, disintegrable material with brownish tarnish.
2023-MAC-008	Lower Breccia	PCHAC-14-TW	225.50	13º 59' 56.070"	82º 40' 37.632"	Fine-grained, disintegrable material with brownish tarnish.
2023-MAC-009	Lower Breccia	PCHAC-14-TW	229.00	13º 59' 56.070"	82º 40' 37.699"	Samples with irregular to anastomosing alternation of black and white levels but with apple-green levels.
2023-MAC-011	Lower Breccia	PCHAC-14-TW	237.30	13º 59' 56.068"	82º 40' 37.857"	Surface oxidized, whitish. Very fine-grained.
2023-MAC-012	Lower Breccia	PCHAC-14-TW	323.30	13º 59' 56.057"	82º 40' 39.501"	Defined as “single mineral” by the company.
2023-MAC-013	Lower Breccia	PCHAC-33-TV	172.80	14º 00' 0.587"	82º 40' 43.152"	White fine-grained sample, apple green material fills the space between the white material.
2023-MAC-014	Lower Breccia	PCHAC-33-TV	249.00	14º 0' 0.587"	82º 40' 43.152"	Sample of banded texture with millimetric quartz grains.
2023-MAC-015	Lower Breccia	PCHAC-33-TV	250.50	14º 0' 0.587"	82º 40' 43.152"	Banded texture? Possible unidirectional solidification texture (UST). Alternation with grey levels.
2023-MAC-016	Lower Breccia	PCHAC-33-TV	258.10	14º 0' 0.587"	82º 40' 43.152"	Crackle breccia.
2023-MAC-017	Lower Breccia	PCHAC-33-TV	280.30	14º 0' 0.587"	82º 40' 43.152"	Yellow material with black dots up to 2mm alternating with greenish gray material.
2023-MAC-018	Lower Breccia	PCHAC-33-TV	281.00	14º 0' 0.587"	82º 40' 43.152"	>9,000 ppm-Cs, defined as “single mineral” by the company.

Sample	Unit	DDH	Depth (m)	Geographical coordinates*		Field description
				Latitude - S	Longitude - W	
2023-MAC-020	Lithium Rich Tuff	PCHAC-12-TW	46.70	14º 0' 10.866"	82º 40' 38.954"	White “earthy” sample.
2023-MAC-021	Lower Breccia	PCHAC-33-TW	193.00	14º 0' 0.562"	82º 40' 46.84"	Fine white with dark brown tarnish from alteration/weathering. Engineer Geologist (Henry) tells us that the brown tarnish forms within hours of cutting the samples.
2023-MAC-022	Lower Breccia	PCHAC-33-TW	201.50	14º 0' 0.561"	82º 40' 47.003"	Fine white with dark brown tarnish.
2023-MAC-023	Lower Breccia	PCHAC-33-TW	212.90	14º 0' 0.559"	82º 40' 47.221"	Fine white with dark brown.
2023-MAC-024	Lower Breccia	PCHAC-33-TW	221.70	14º 0' 0.558"	82º 40' 47.389"	Fine white with dark brown tarnish.
2023-MAC-025	Lower Breccia	PCHAC-33-TW	232.50	14º 0' 0.556"	82º 40' 47.595"	Banded texture with brownish tarnish.

***** *Coordinates for DDH samples refer to the location of DDH collars.*

Appendix B: Macroscopic description of the surface and drill core samples

2021-MAC-026

Hard, whitish rock with fine layers and grayish nodules. The layers are irregular, sometimes wavy, and the nodules are scattered or clustered in certain bands. It also contains small matrix-supported biotite crystal clasts.

2021-MAC-053

Disaggregated, soft, and clayey rock exhibits a white color. It contains small biotite and quartz fragments supported by the clayey matrix. Most original minerals in this rock have been obliterated.

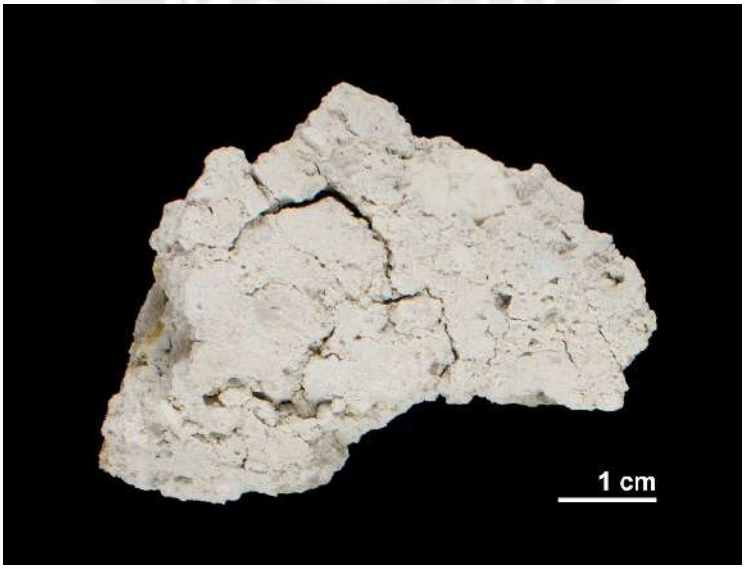

2023-MAC-001

White rock, hard and consolidated, with a smooth surface, adheres easily to the tongue. It contains small lithic fragments, quartz, and biotite crystal clasts, which are randomly distributed within a clayey matrix.

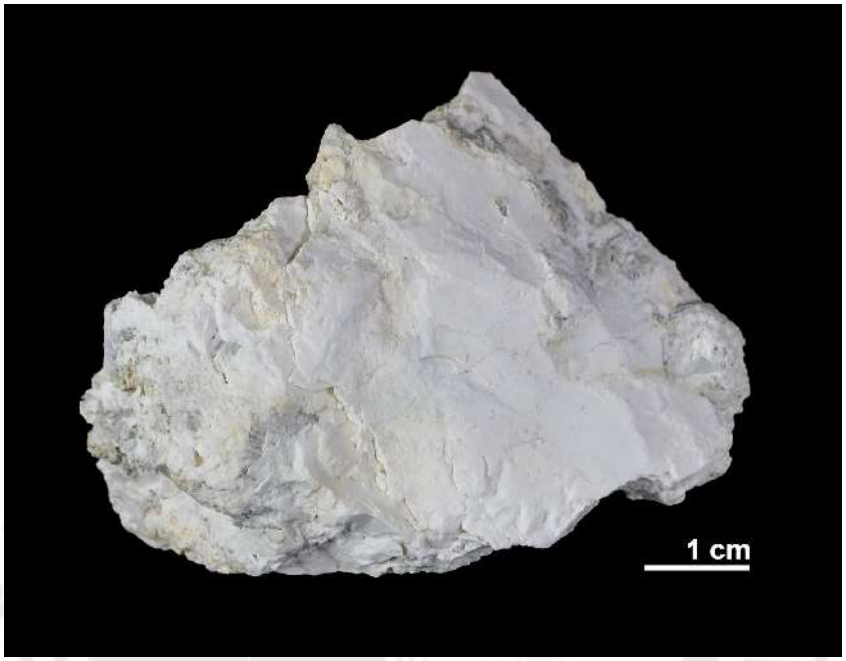

2023-MAC-002

Hard, white rock with brown surface patinas. It contains small lithic fragments, quartz, and biotite supported in a very fine-grained matrix.

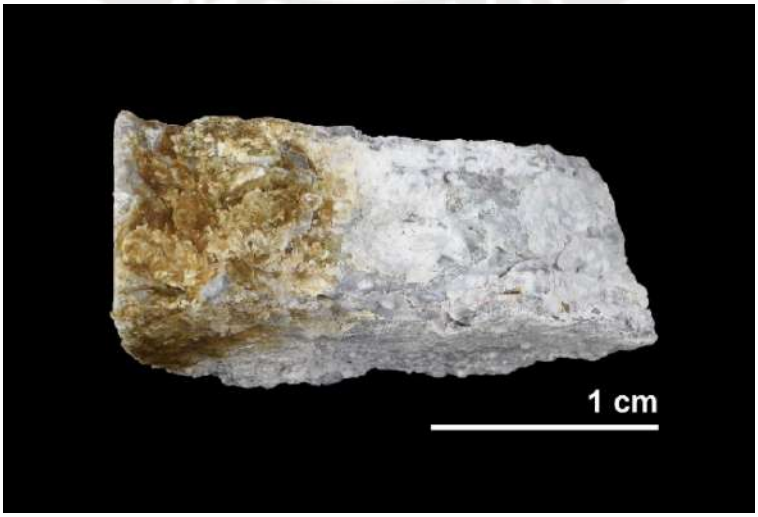

2023-MAC-005

Soft, lightweight, white rock with an altered surface forming brown-yellow patinas. It contains small lithic fragments, quartz, and biotite crystal clasts supported in a very fine-grained matrix.

2023-MAC-006

Soft, white rock with dark brown patina on surface. It contains small lithic fragments, quartz, and biotite crystal clasts supported in a very fine-grained matrix.

2023-MAC-007

Soft, lightweight, white rock with an altered surface forming brown patinas. It contains small quartz and biotite clasts supported in a very fine-grained matrix.

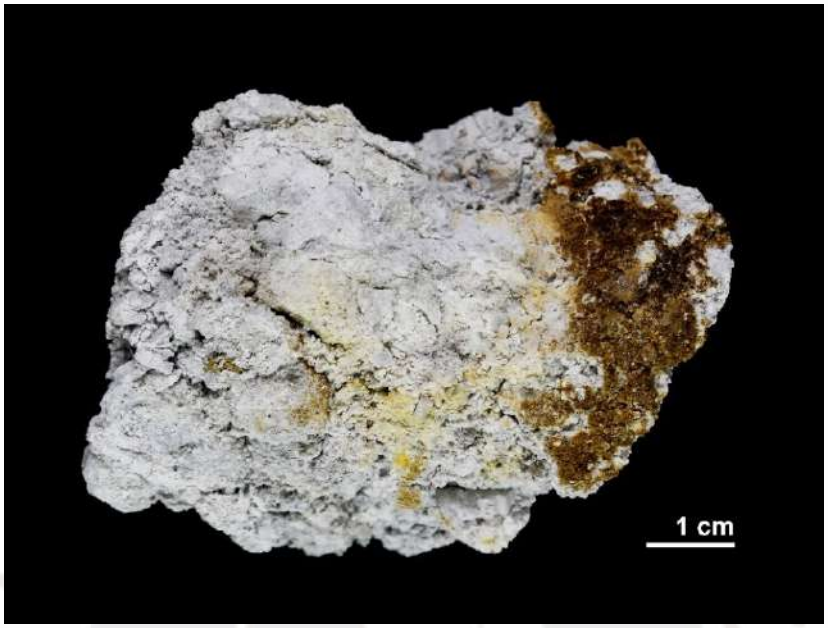

2023-MAC-008

Hard, slightly heavy, white rock with an altered surface forming brown patinas. It contains small lithic fragments, quartz, and biotite clasts supported in a very fine-grained matrix.

2023-MAC-009

The rock is hard and dense, exhibiting alternating white and black bands. The white bands show yellow patinas. The bands are planar to anastomosed.

2023-MAC-011

The rock is moderately lightweight, white, and displays an altered surface with dark brown patinas. It contains small lithic fragments, quartz, and biotite crystal clasts embedded in a soft, slightly rough whitish clayey matrix.

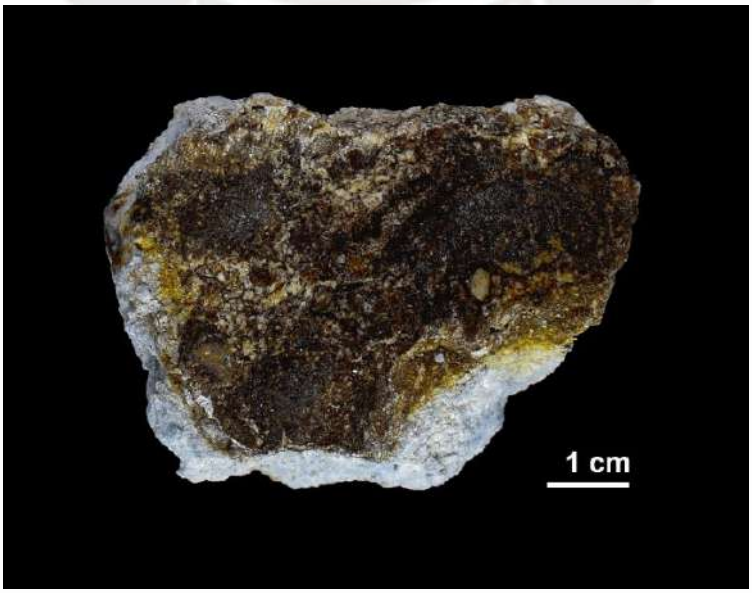

2023-MAC-012

The rock is soft, low-density, and medium-hard, with a white, fine-grained, and clayey matrix containing scattered dark brown, subhedral mica (biotite) crystal clasts and quartz.

2023-MAC-013

A soft, moderately dense, and white rock displaying surface alteration with brown patinas. The sample consists of small lithic fragments and biotite crystal clasts that are supported in a fine-grained and clayey matrix.

2023-MAC-014

Hard, and dense white rock with brown weathering surfaces. Its composition consists of subrounded lithic fragments, rounded gray amorphous quartz grains, brown biotite flakes, and volcanic glass. The rock displays a banded texture, characterized by alternating layers of glass-rich material that form a distinct blocky pattern.

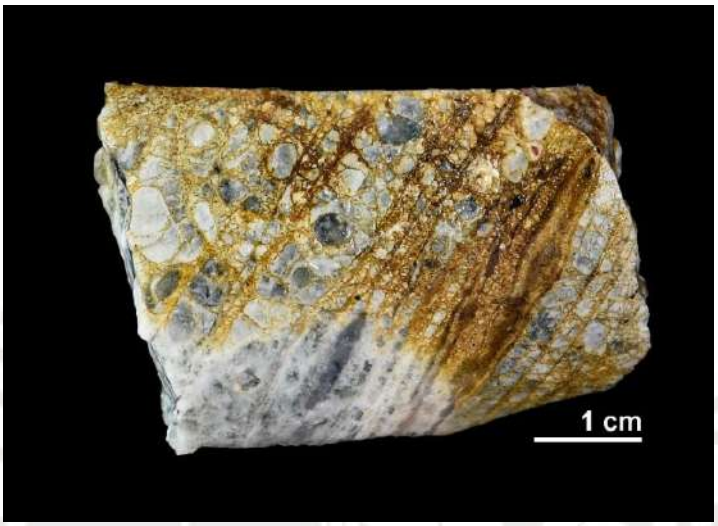

2023-MAC-015

Fine-grained gray material with a pinkish tint in sharp contact with a very fine-grained whitish and hard host rock; the acute triangular ends of the gray material may suggest textures formed by unidirectional solidification. It also contains small matrix-supported biotite crystal clasts.

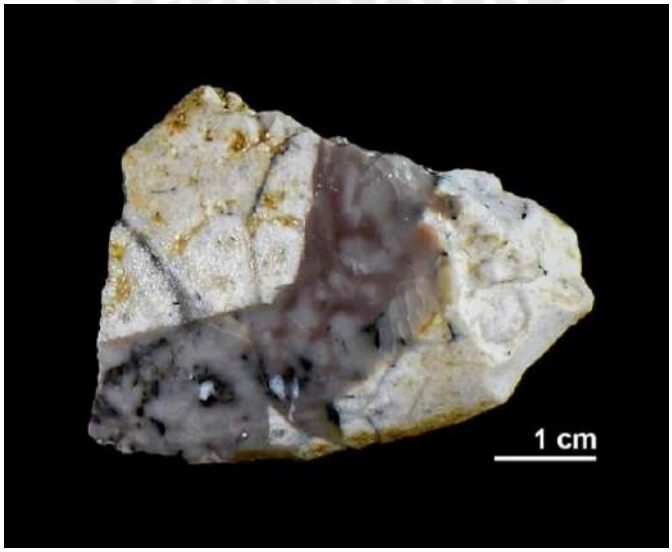

2023-MAC-016

Brecciated rock (white-grey) with yellow-brown weathering surfaces. Its composition includes lithic fragments, rounded white clasts, quartz, biotite, and dispersed iridescent black fine-grained material.

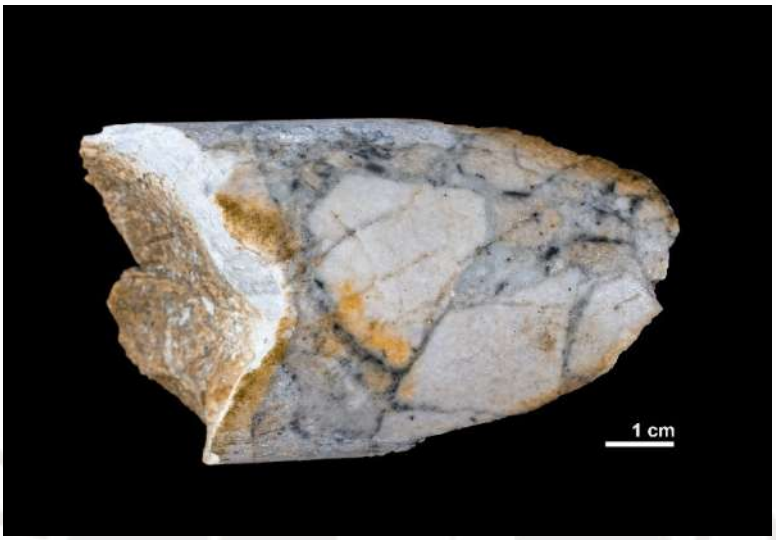

2023-MAC-017A

Soft to the touch, low density, white rock with an altered surface in the form of light-yellow patinas. It contains small lithic fragments, quartz, and biotite clasts, which are supported by a clayey matrix.

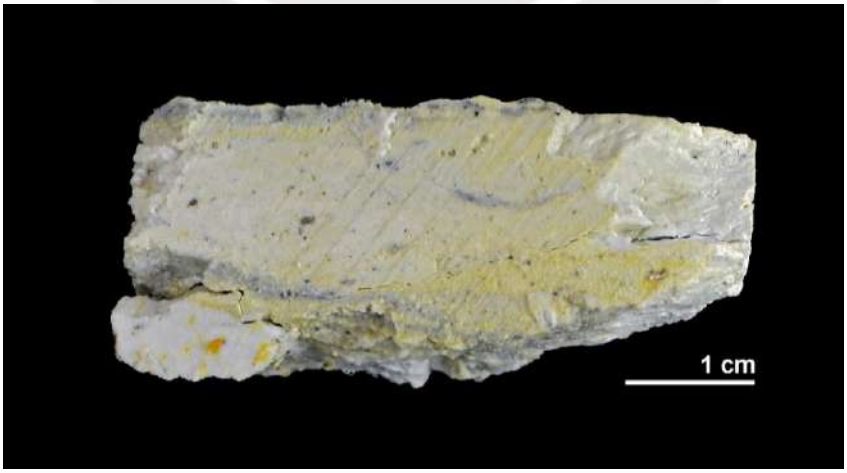

2023-MAC-017B

Hard, dense grey rock with brown surface patinas. Its brecciated texture comprises dark grey subrounded to rounded clasts embedded in a whitish matrix.

2023-MAC-018

A hard rock with high specific gravity and low hardness, containing rounded whitish clayey clasts (up to 1 cm) within a grayish matrix, along with brown biotite and chlorite. The sample displays a brecciated texture, with clasts ranging from rounded to angular in shape, embedded in a very fine-grained, dark gray matrix.

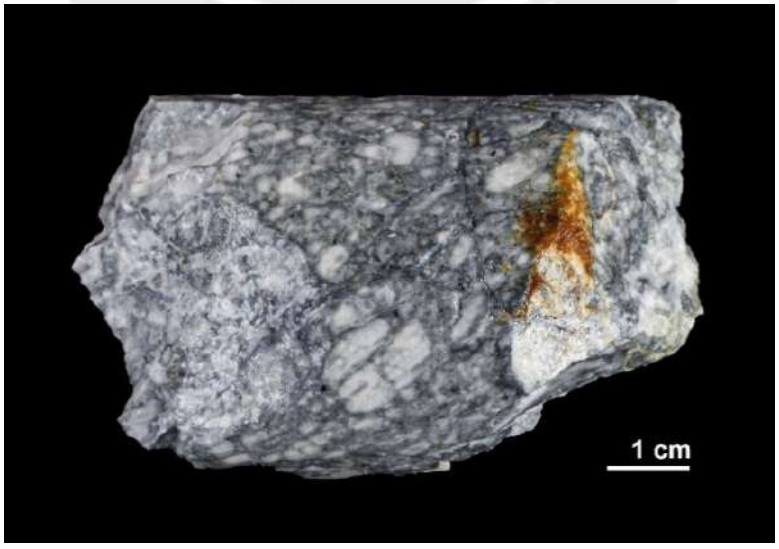

2023-MAC-020

Rough to the touch, medium-density, white rock with an altered surface showing brown patinas. The fresh surface contains small lithic fragments, quartz, and biotite supported in a very fine-grained matrix.

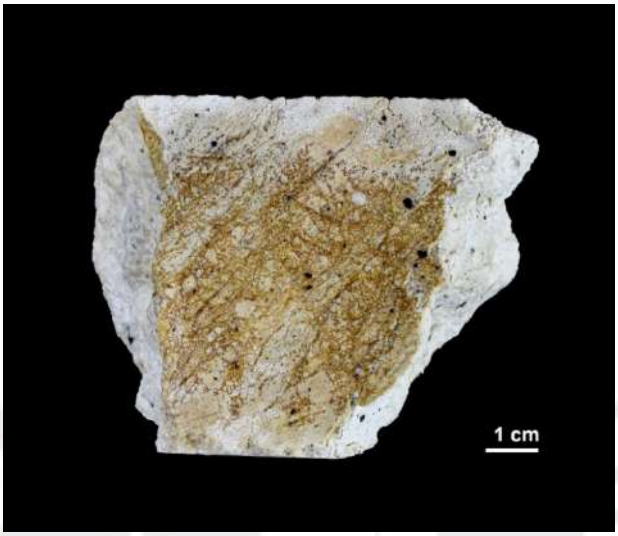

2023-MAC-021

Rough to the touch, low-density white rock with an altered surface showing dark brown patinas. It contains small, matrix-supported lithic fragments, clays, quartz, and medium-sized biotite crystal clasts.

2023-MAC-022

Soft, low-density white rock with an altered surface in the form of dark brown patinas. It contains biotite crystal clasts.

2023-MAC-023

Soft to the touch, low-density white rock with an altered surface showing a brown tarnish. It contains small lithic fragments and brown biotite clasts embedded in a very fine-grained matrix.

2023-MAC-024

Soft, low-density, white rock with an altered surface showing brown and yellow tarnish. It contains small lithic fragments and biotite crystal clasts supported in a clayey matrix.

2023-MAC-025

Soft to the touch, it adheres easily to the tongue, with a low density and an altered surface in the form of brown patinas. It contains clay, quartz, and micaceous biotite.

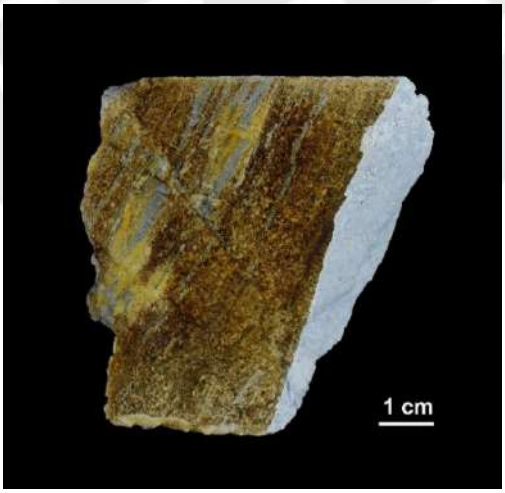

Appendix C: XRD results

2021-MAC-026

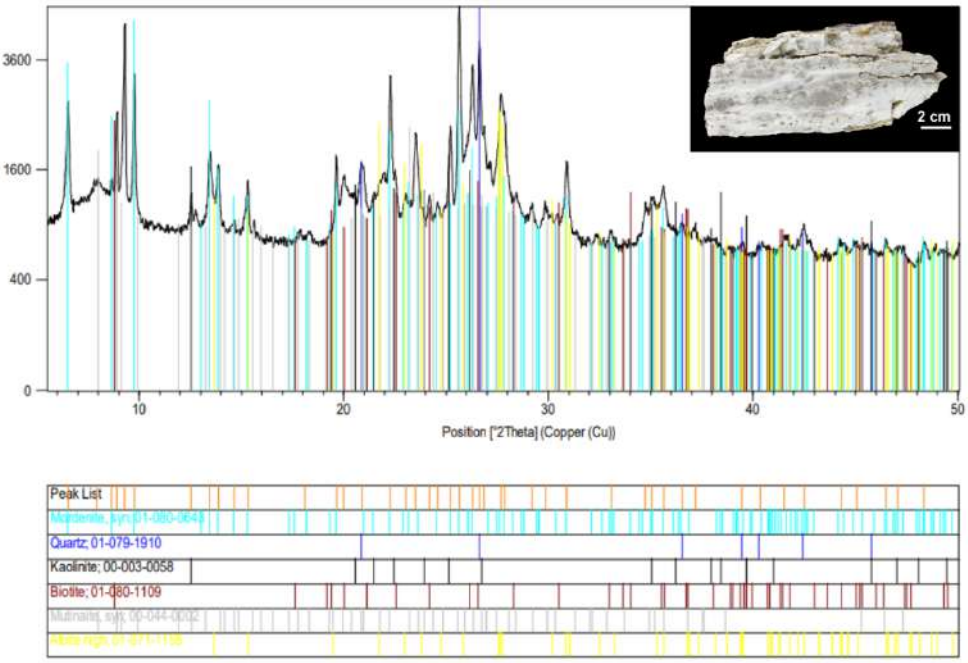

2021-MAC-053

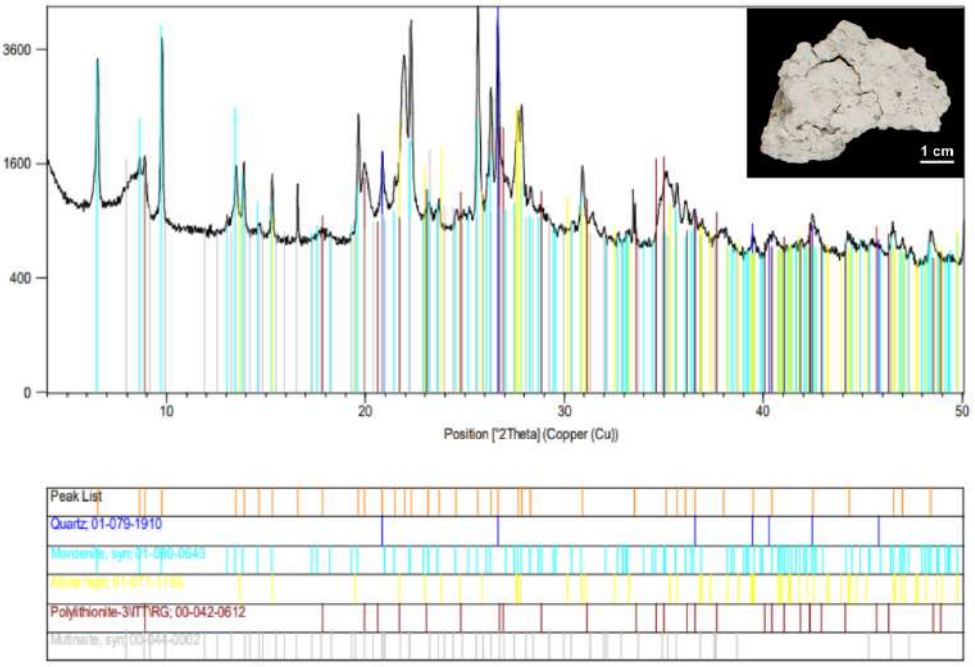

2023-MAC-001

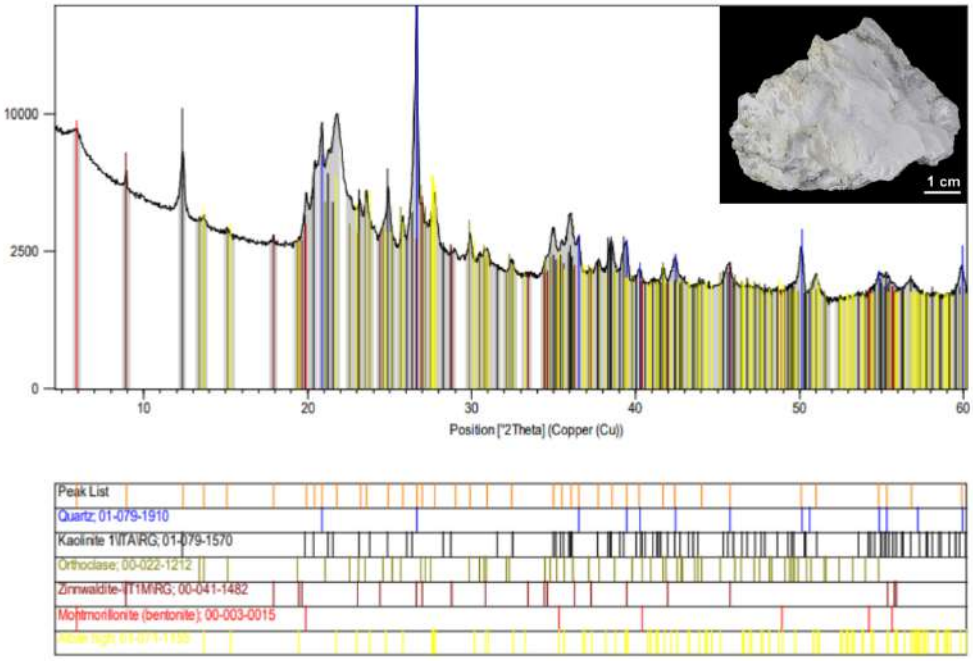

2023-MAC-002

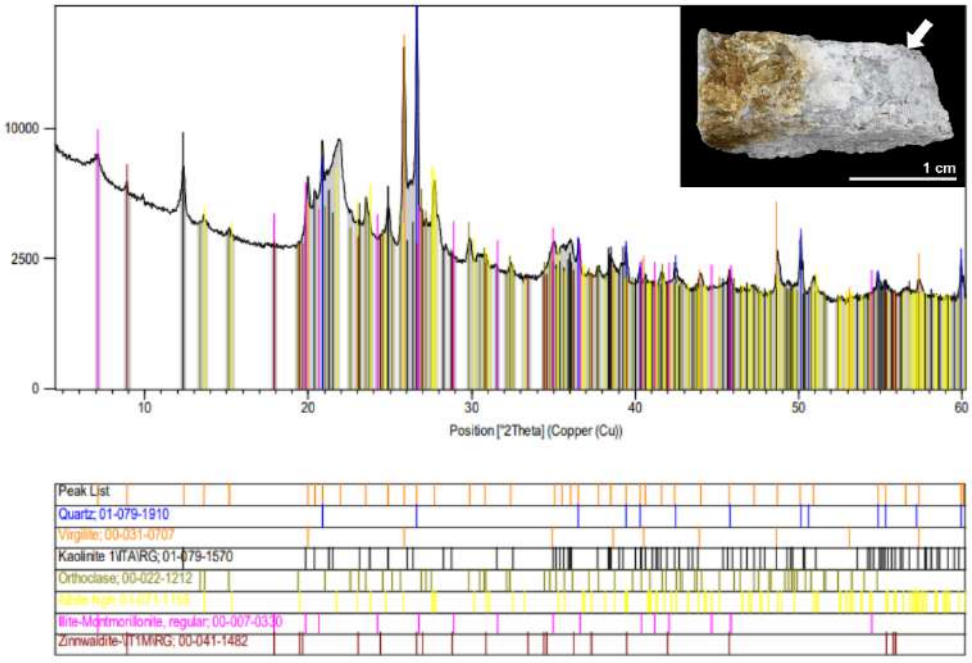

2023-MAC-005A

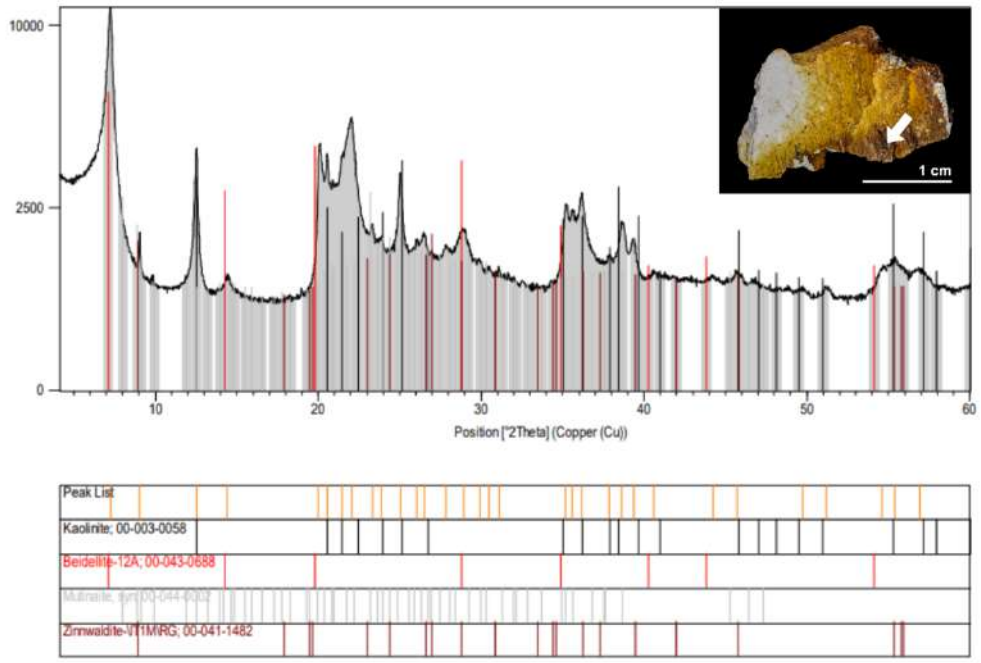

2023-MAC-005B

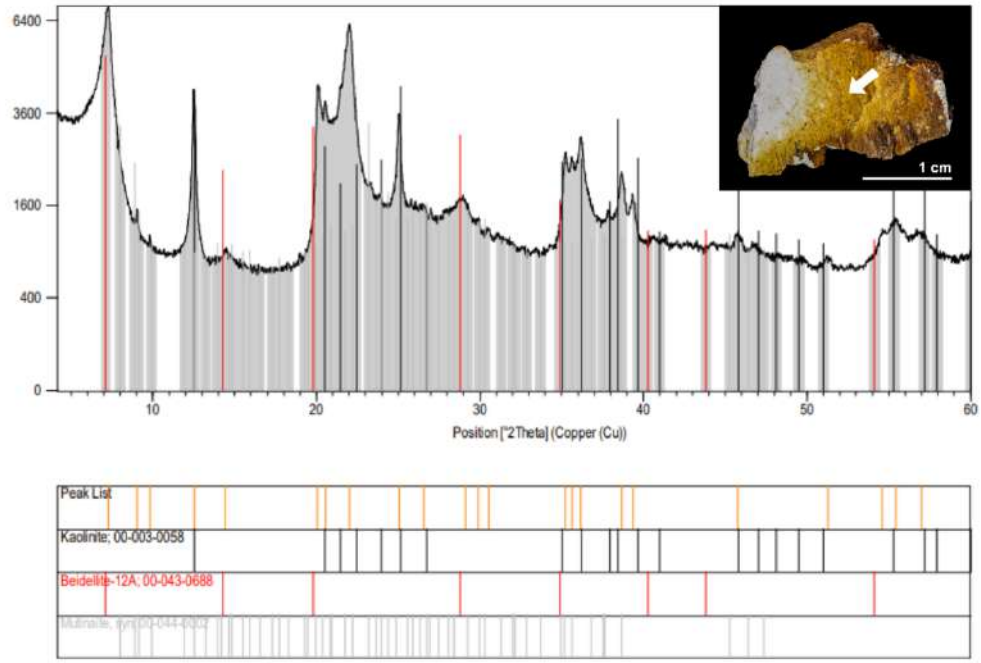

2023-MAC-005C

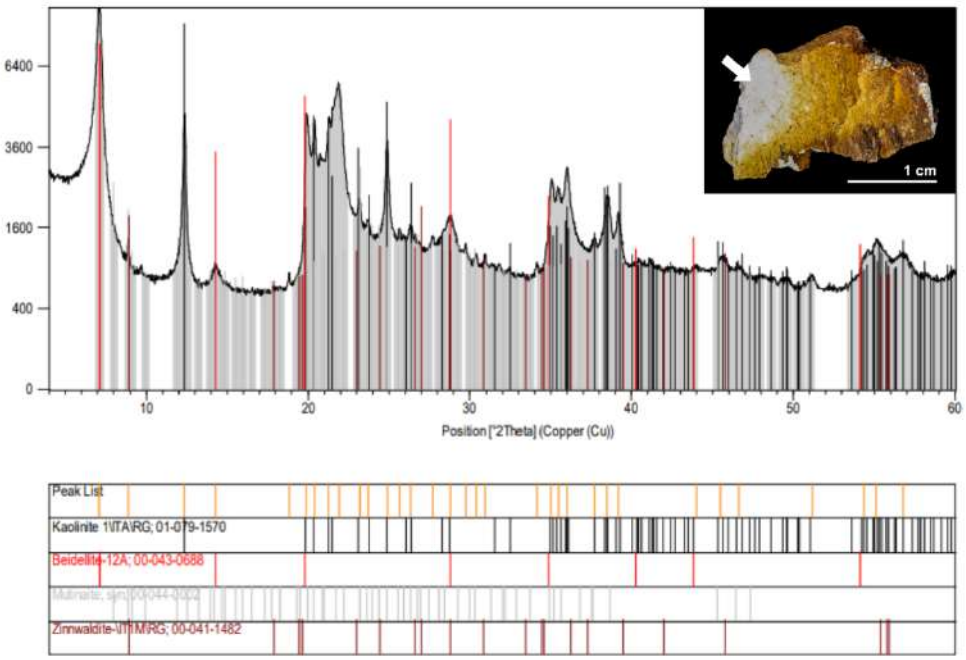

2023-MAC-006A

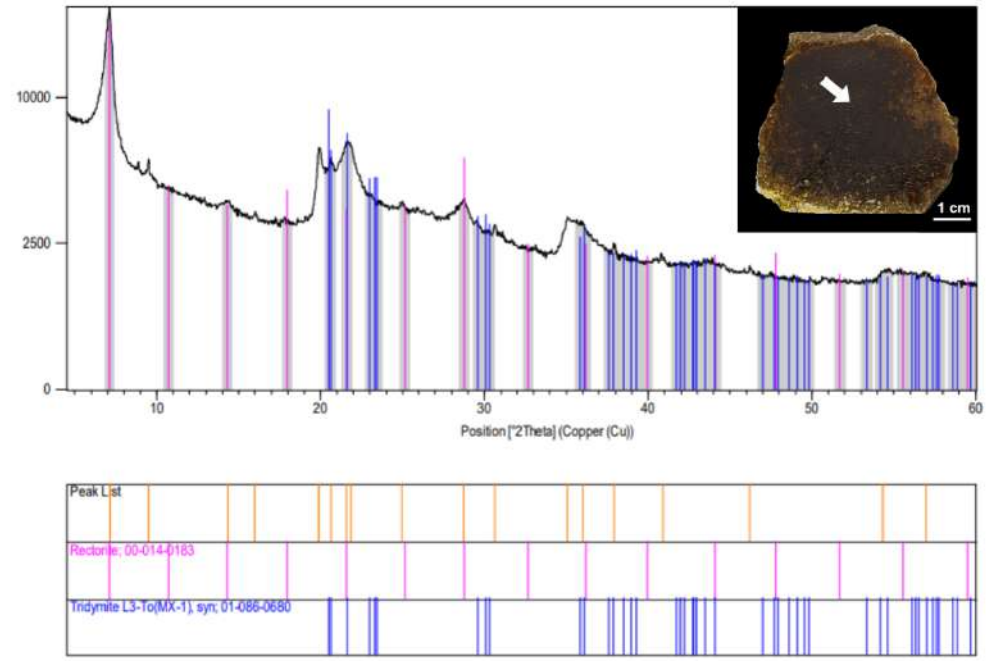

2023-MAC-006B

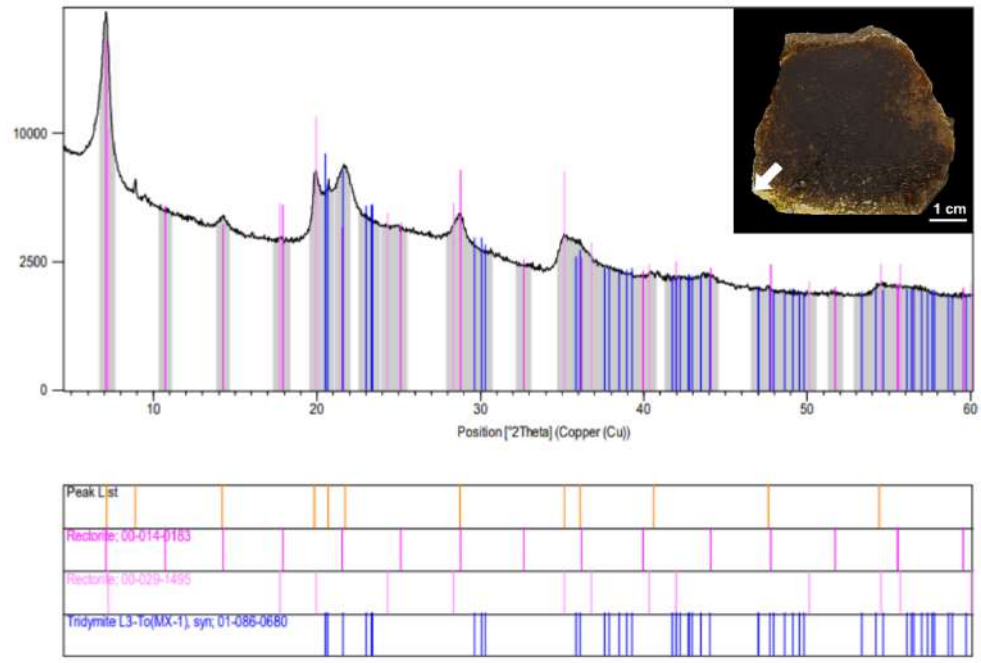

2023-MAC-007A

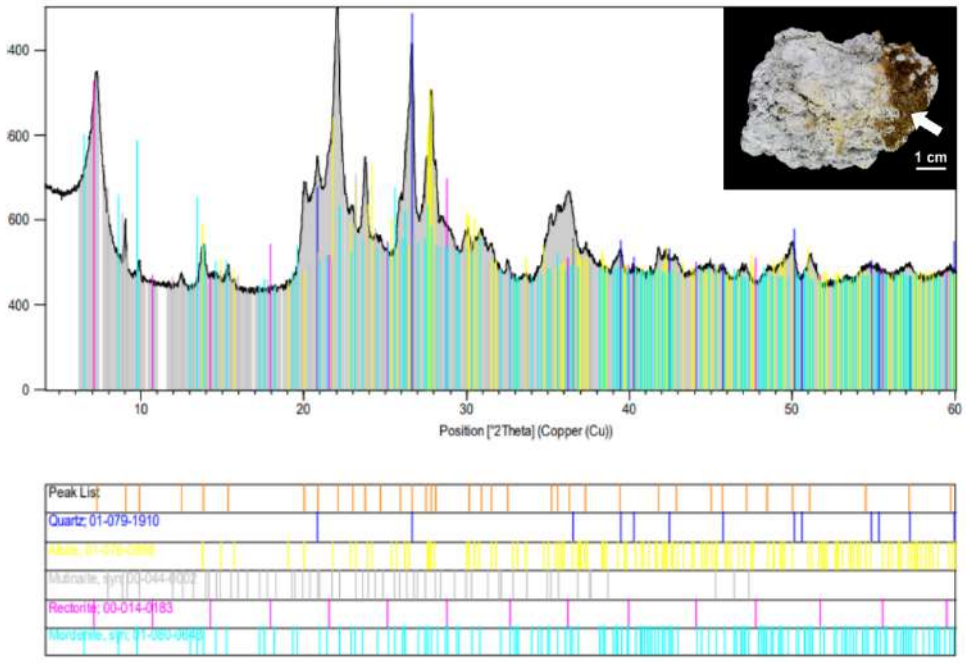

2023-MAC-007B

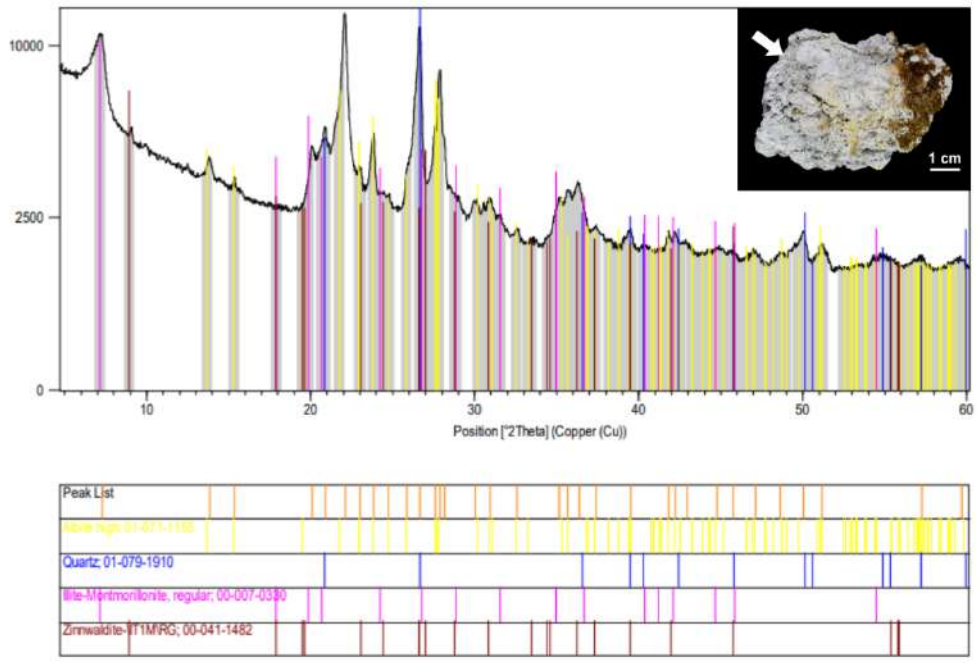

2023-MAC-008A

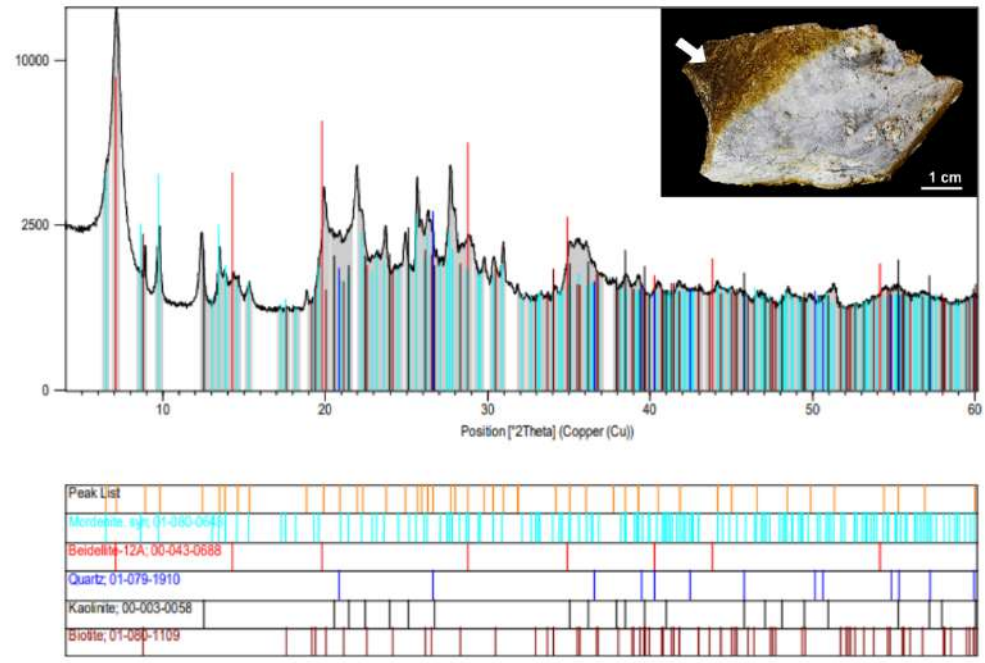

2023-MAC-008B

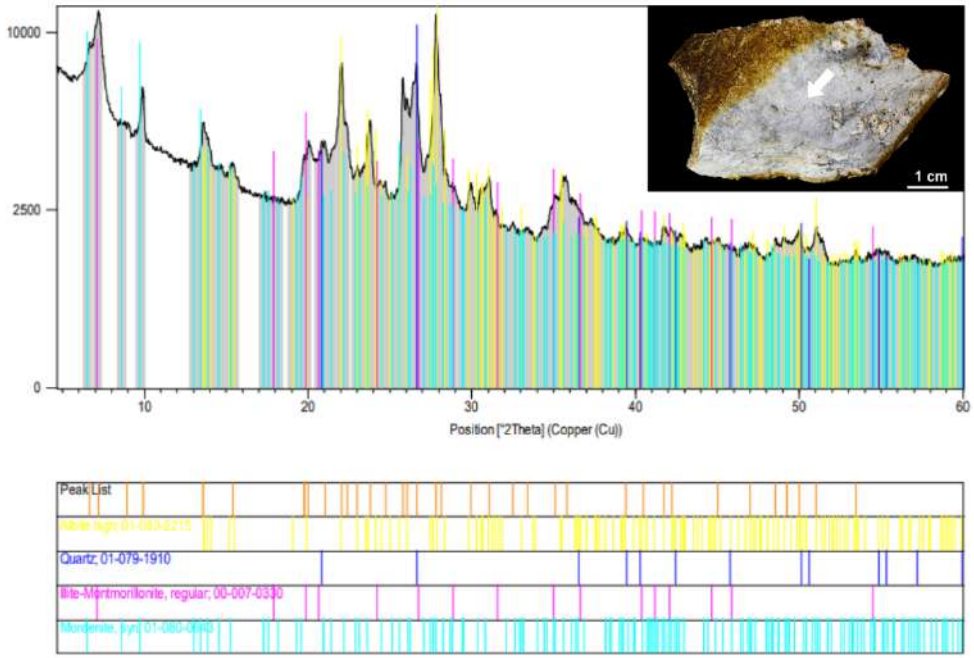

2023-MAC-009

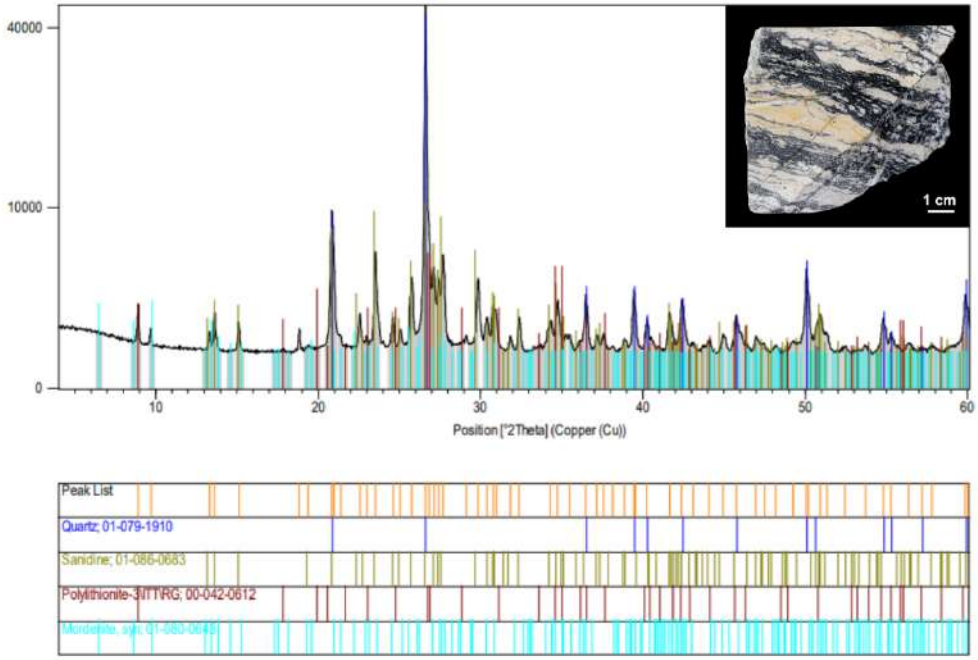

2023-MAC-011A

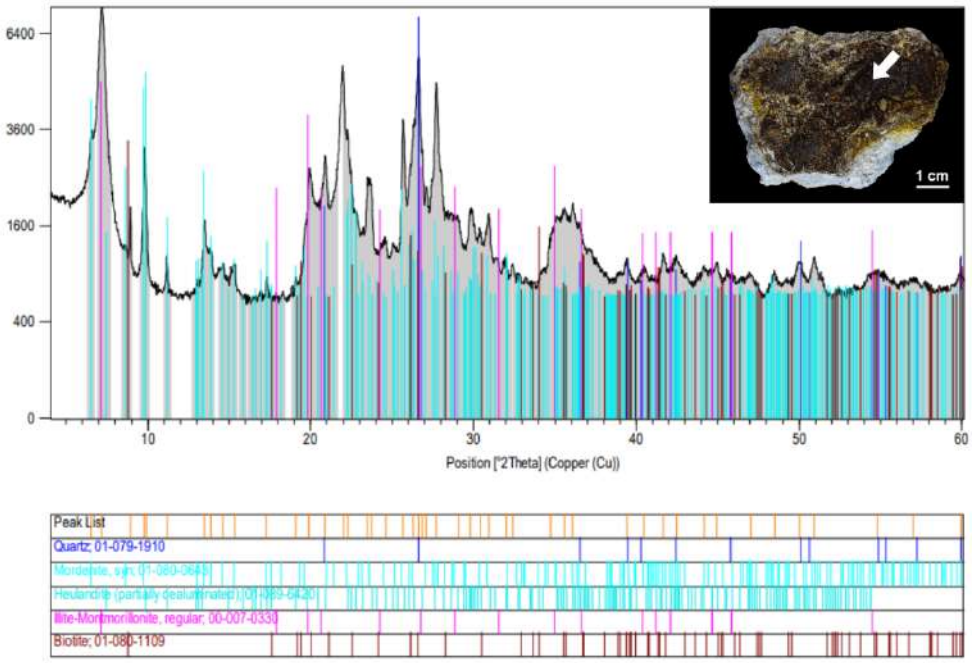

2023-MAC-011B

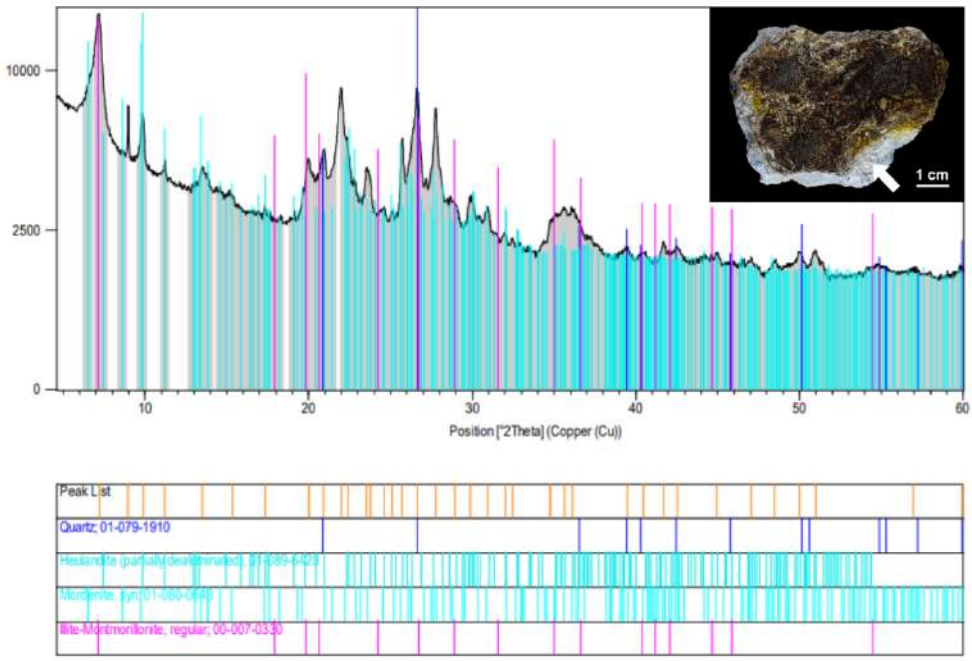

2023-MAC-012

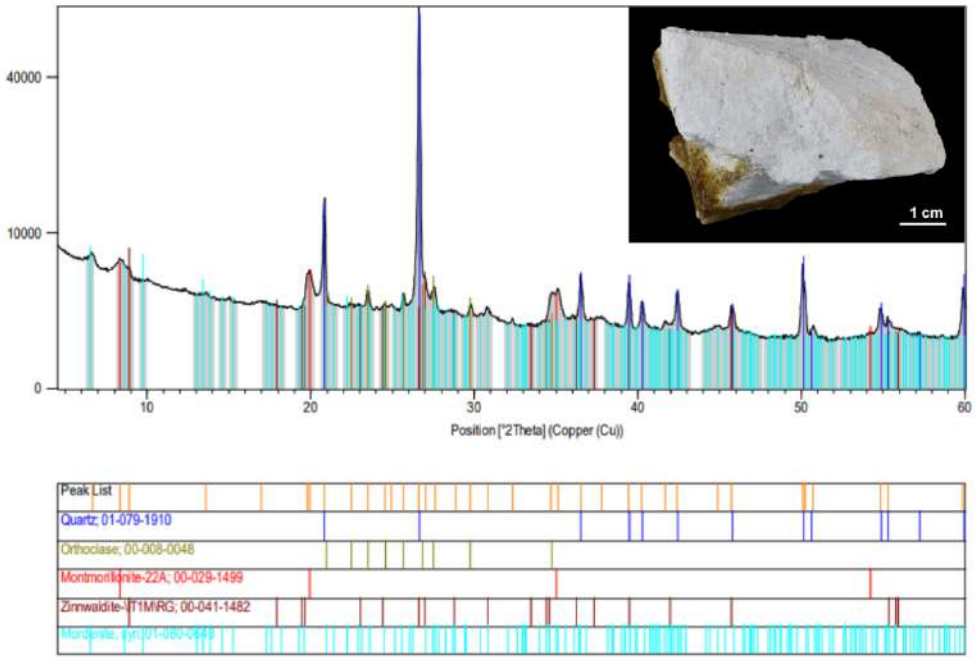

2023-MAC-013A

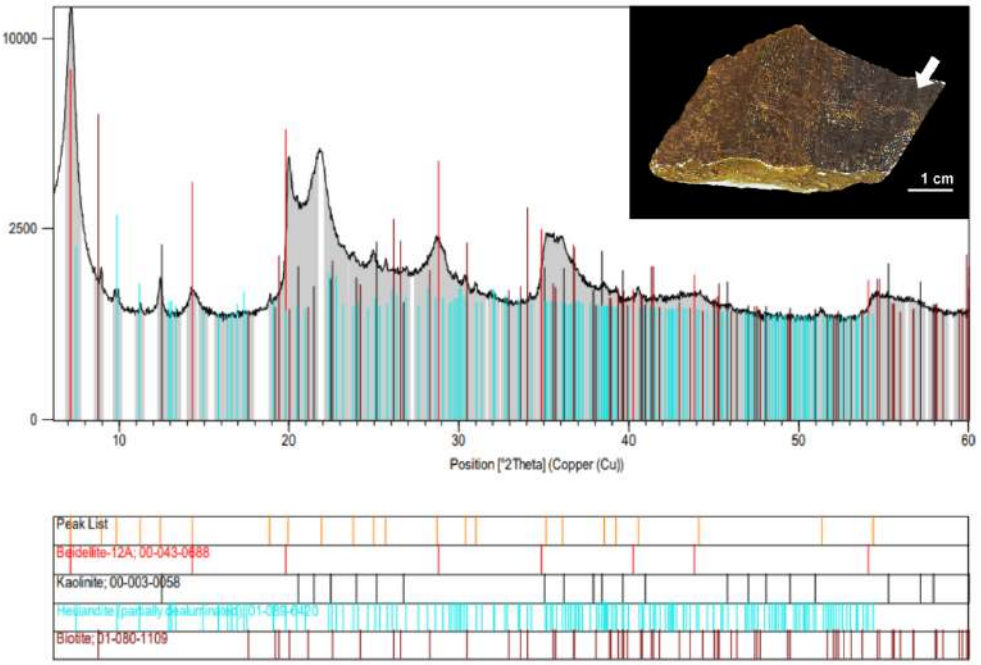

2023-MAC-013B

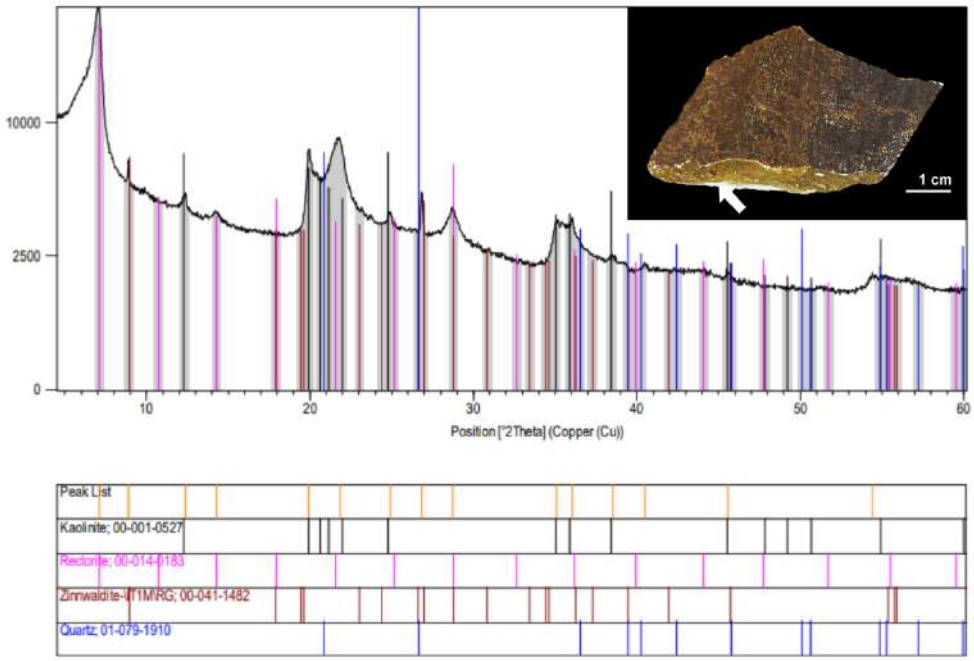

2023-MAC-014

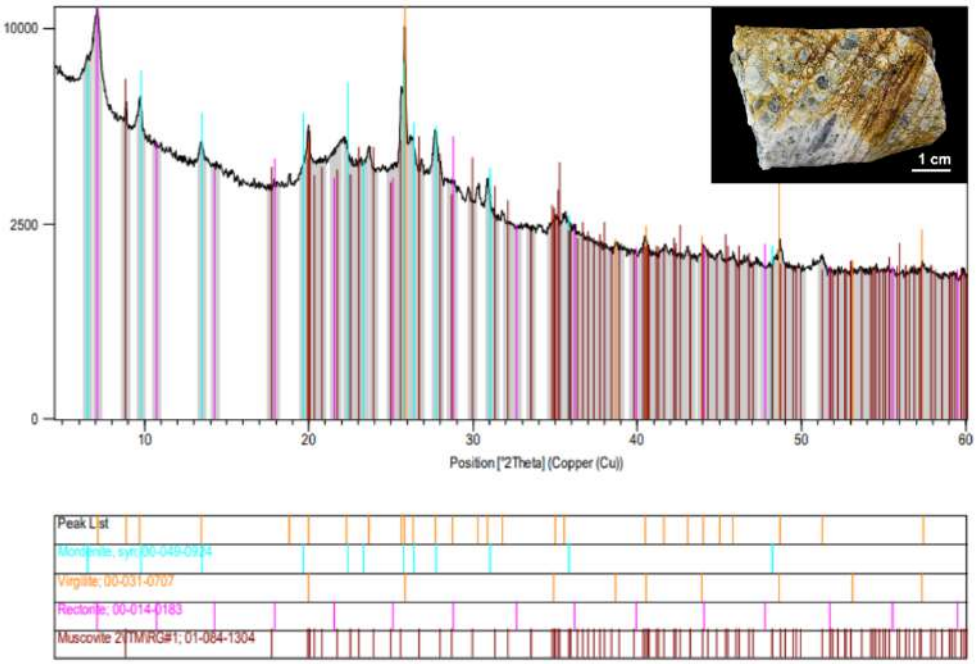

2023-MAC-015A

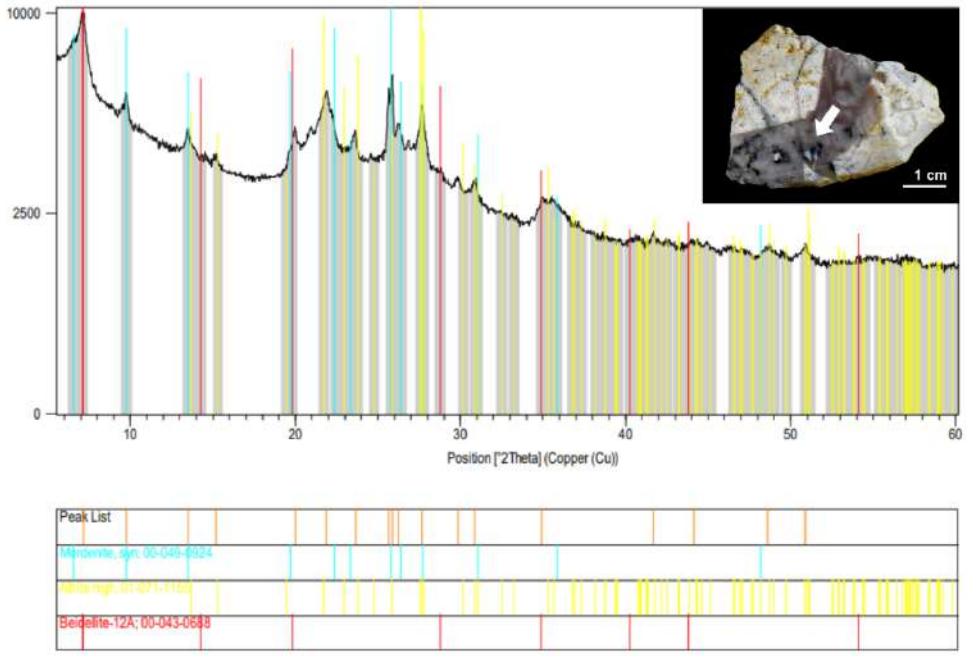

2023-MAC-015B

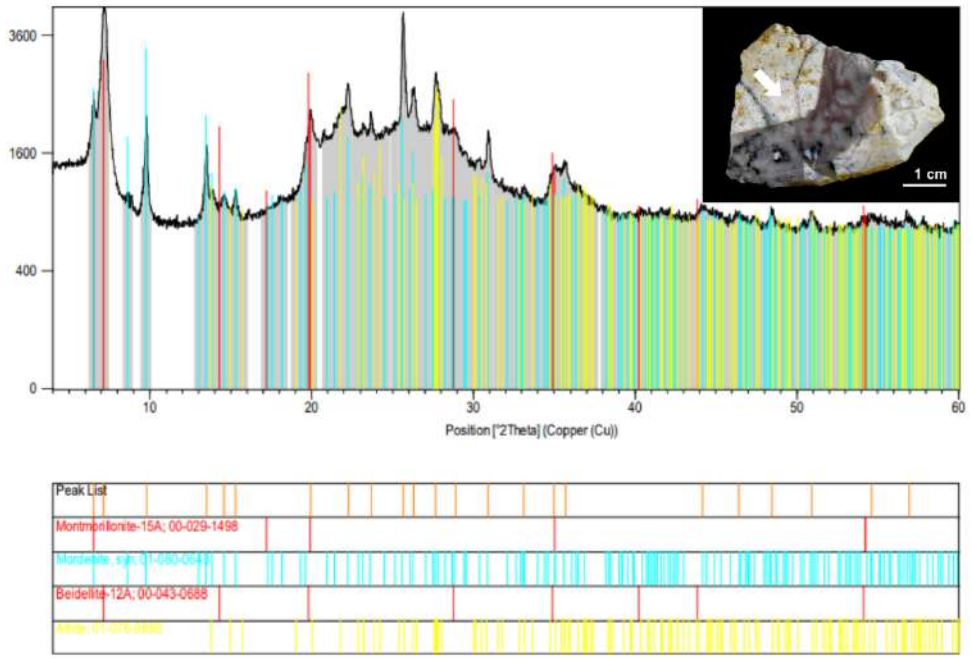

2023-MAC-016

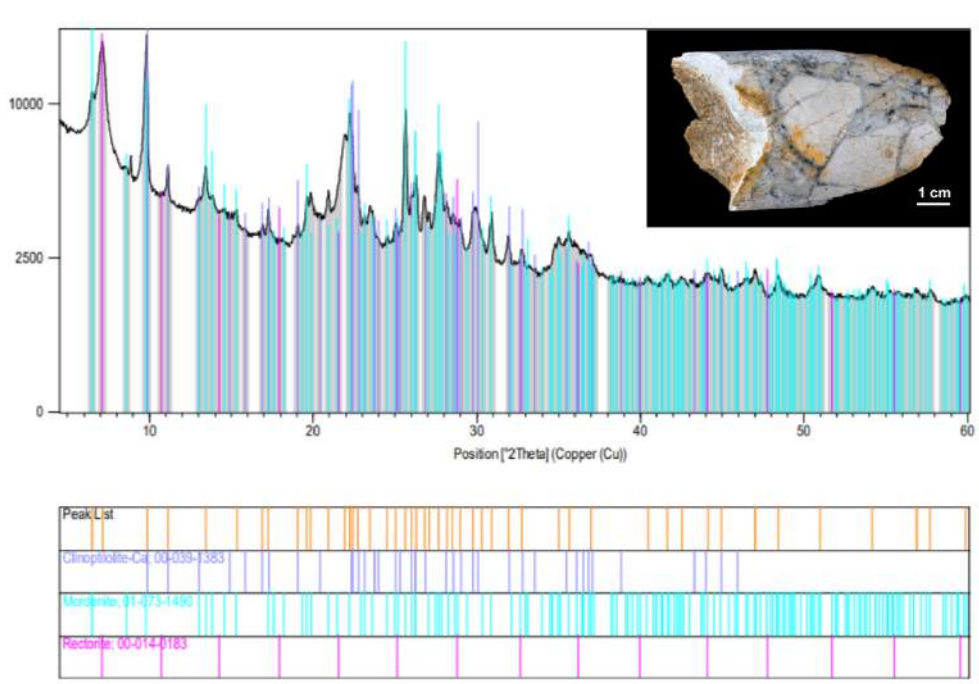

2023-MAC-017A

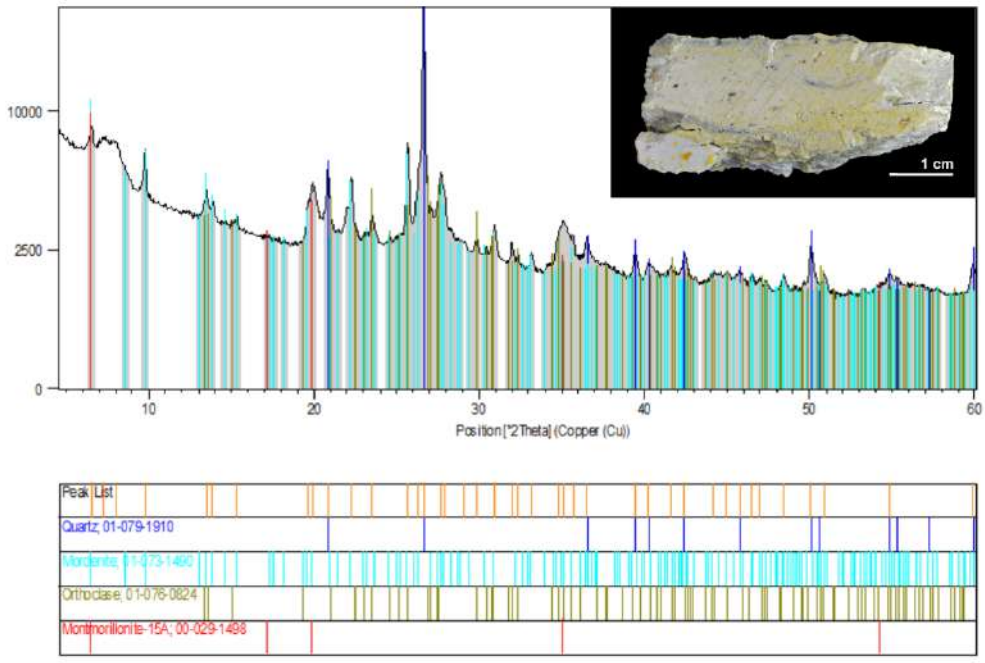

2023-MAC-017B

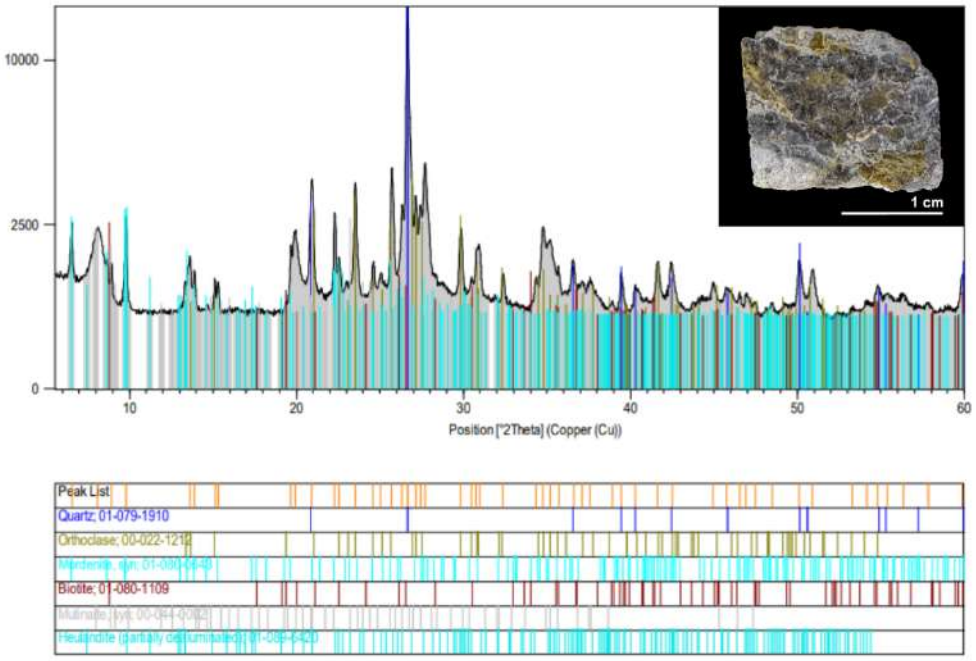

2023-MAC-018

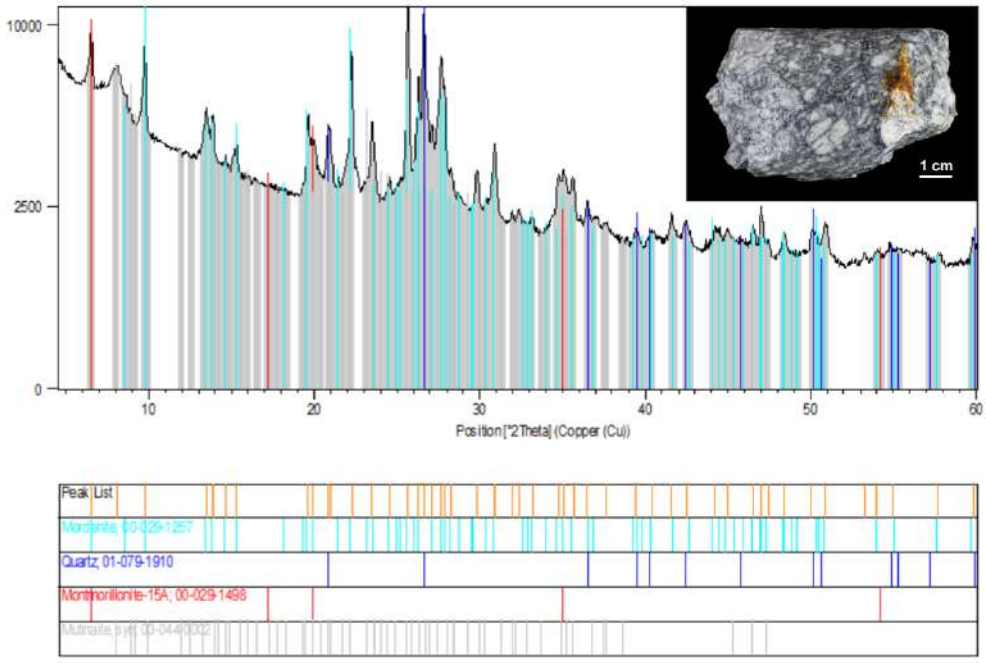

2023-MAC-020

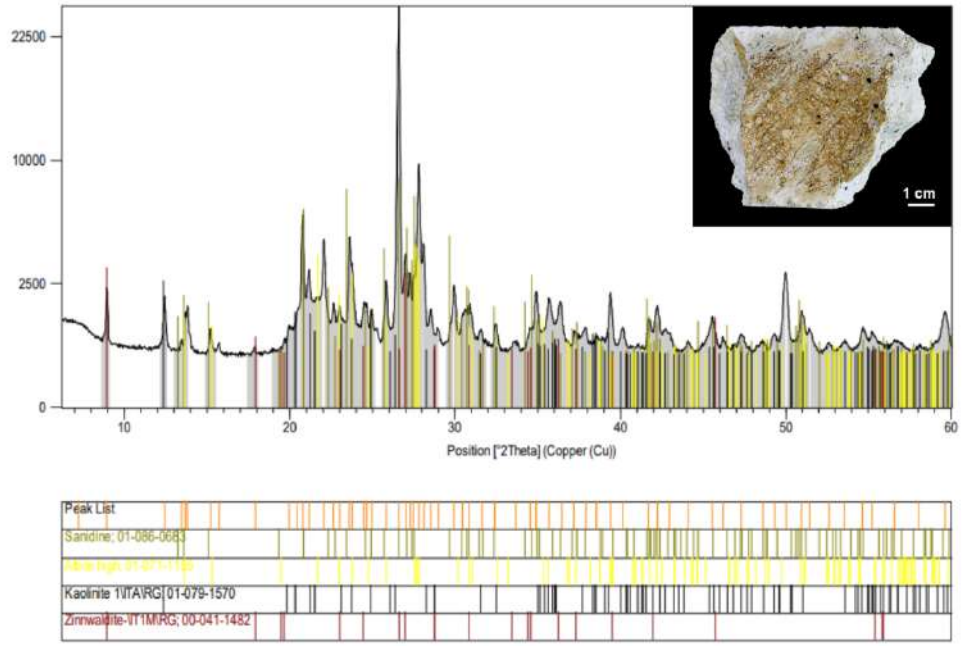

2023-MAC-021A

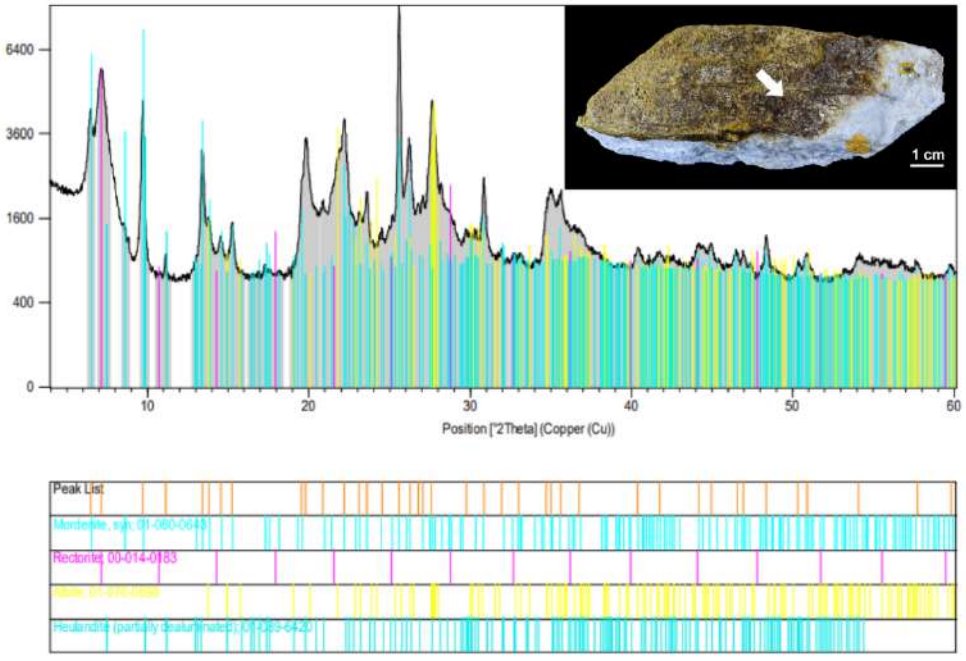

2023-MAC-021B

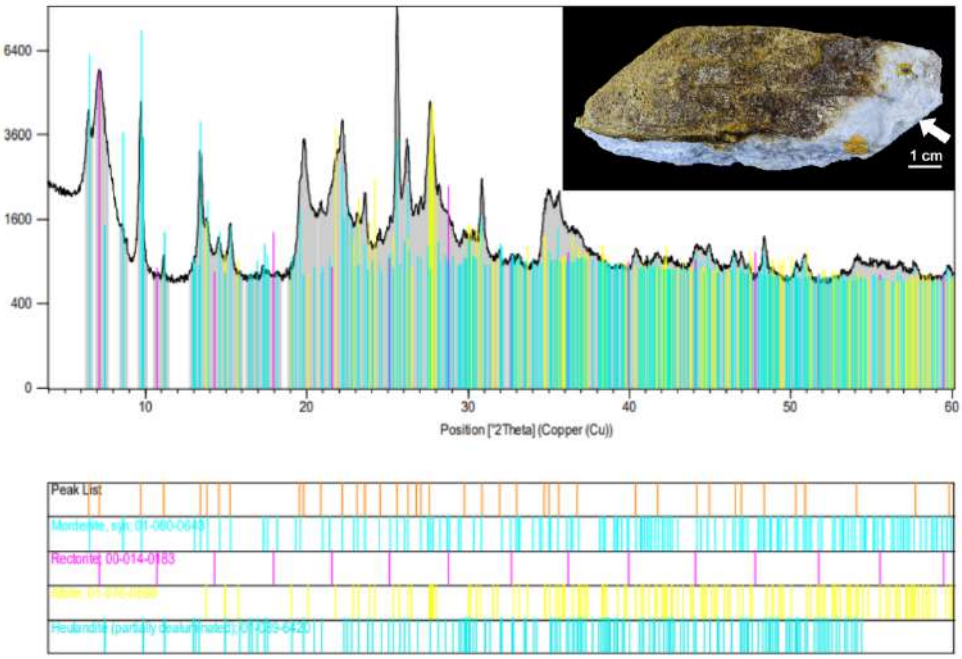

2023-MAC-022A

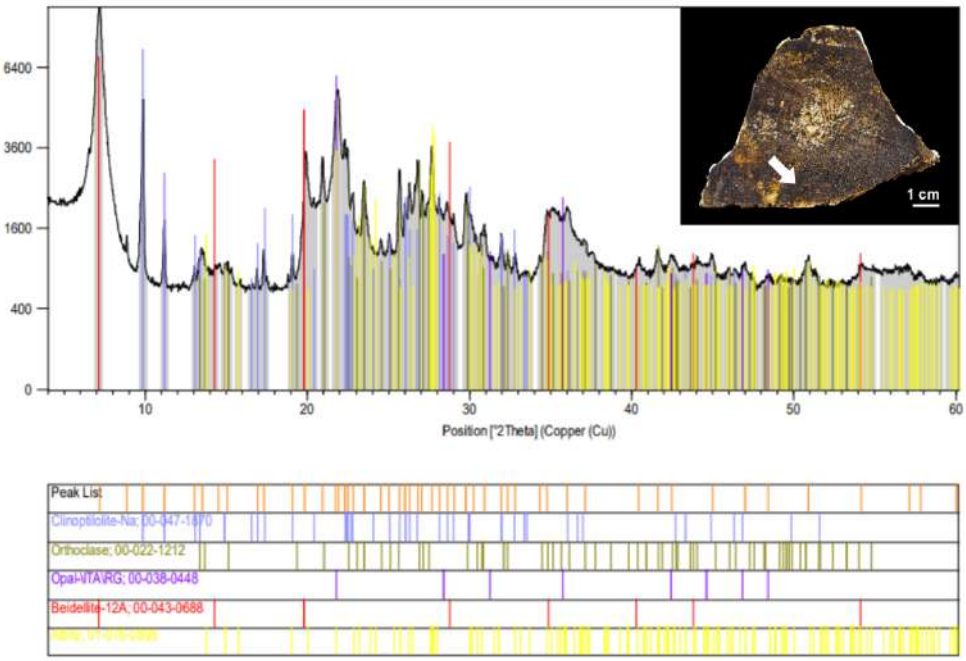

2023-MAC-022B

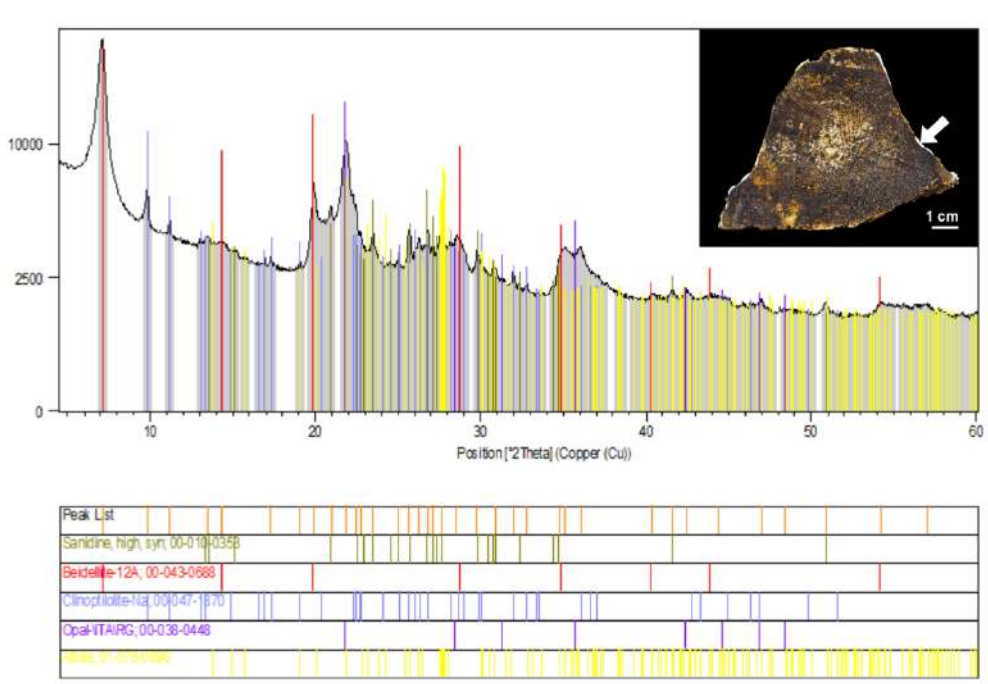

2023-MAC-023A

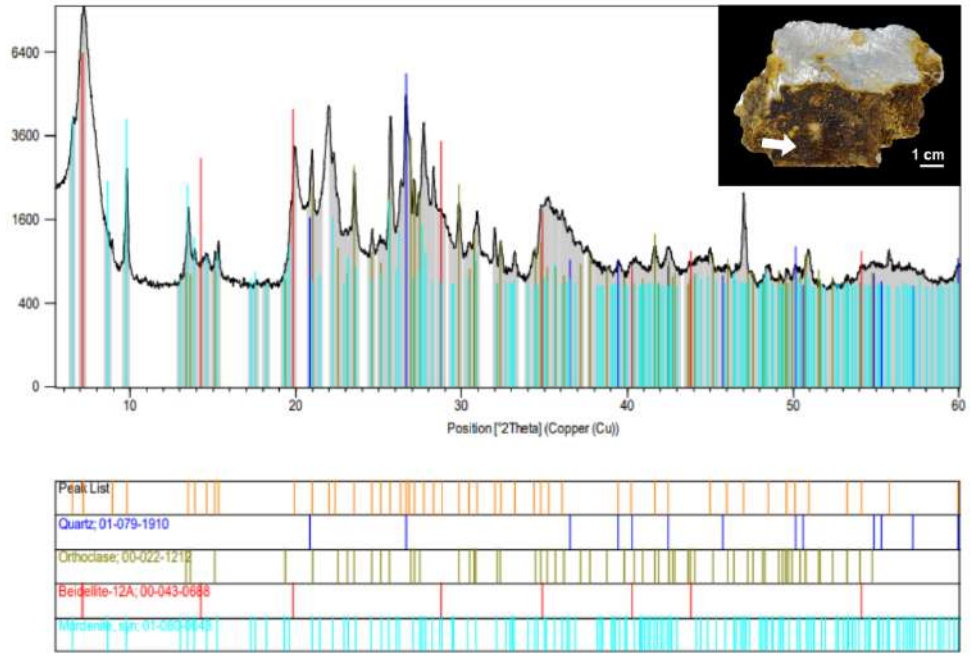

2023-MAC-023B

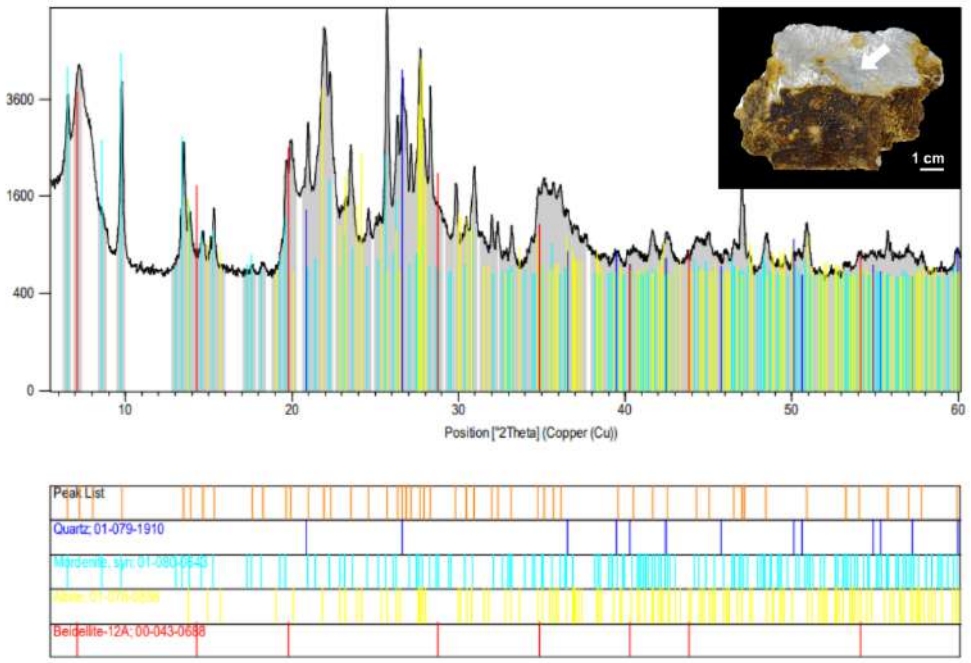

2023-MAC-024A

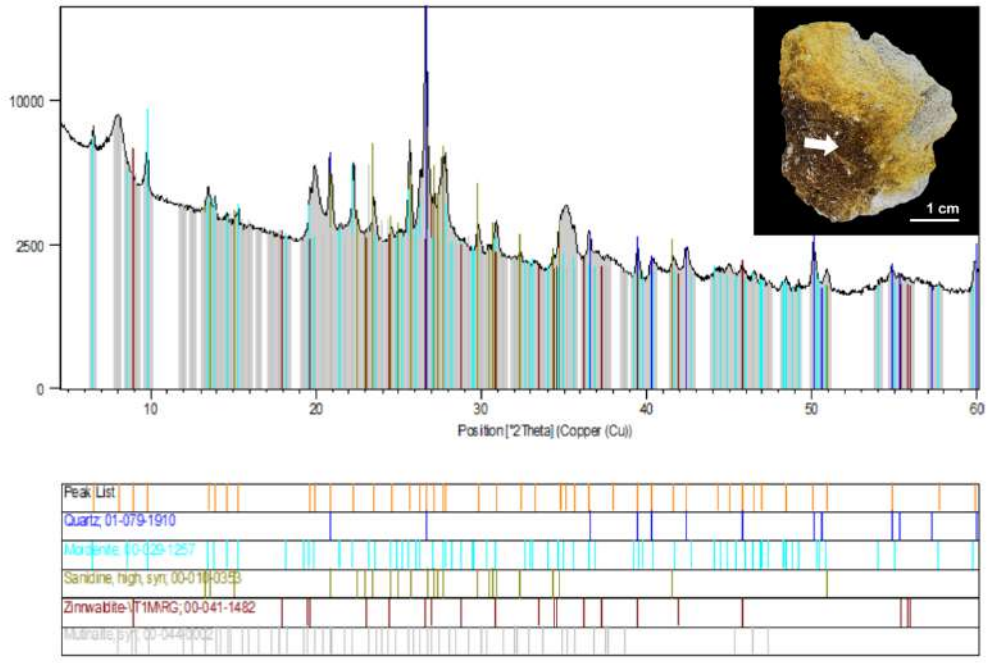

2023-MAC-024B

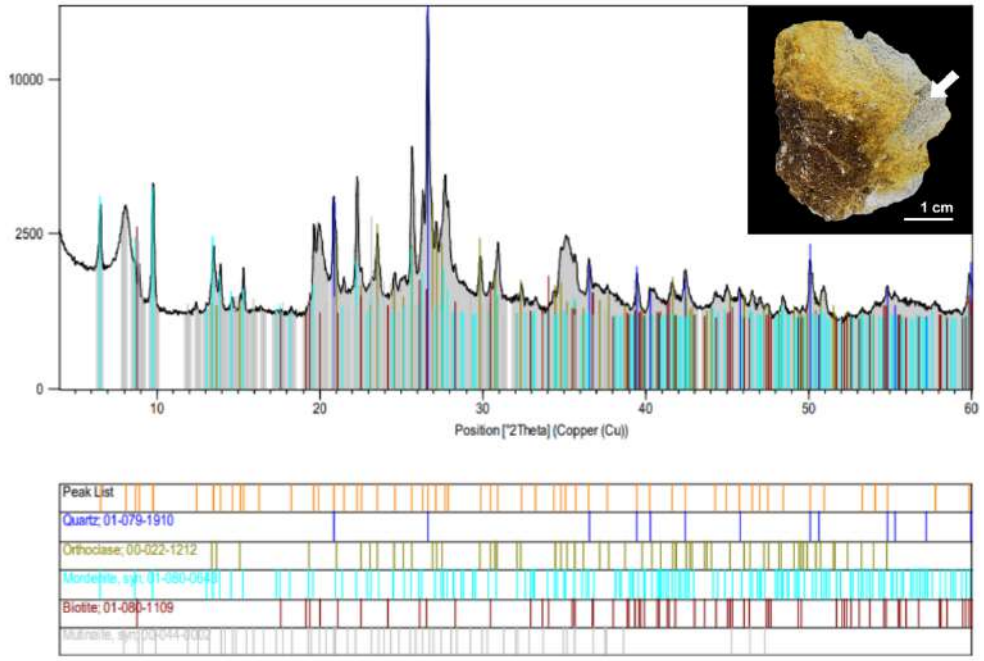

2023-MAC-025

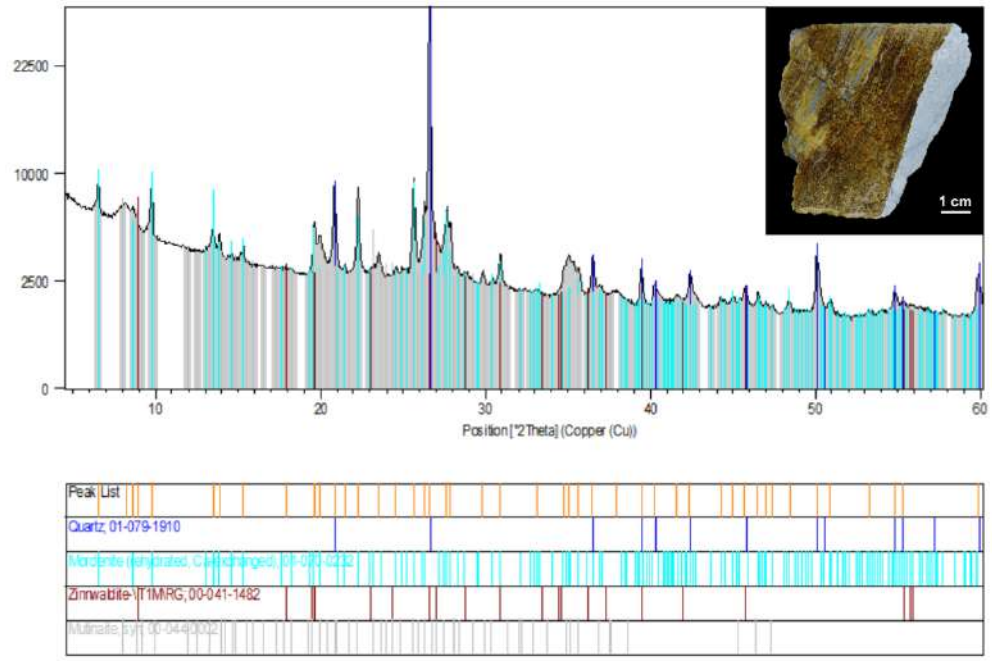

Appendix D: Microscopic descriptions

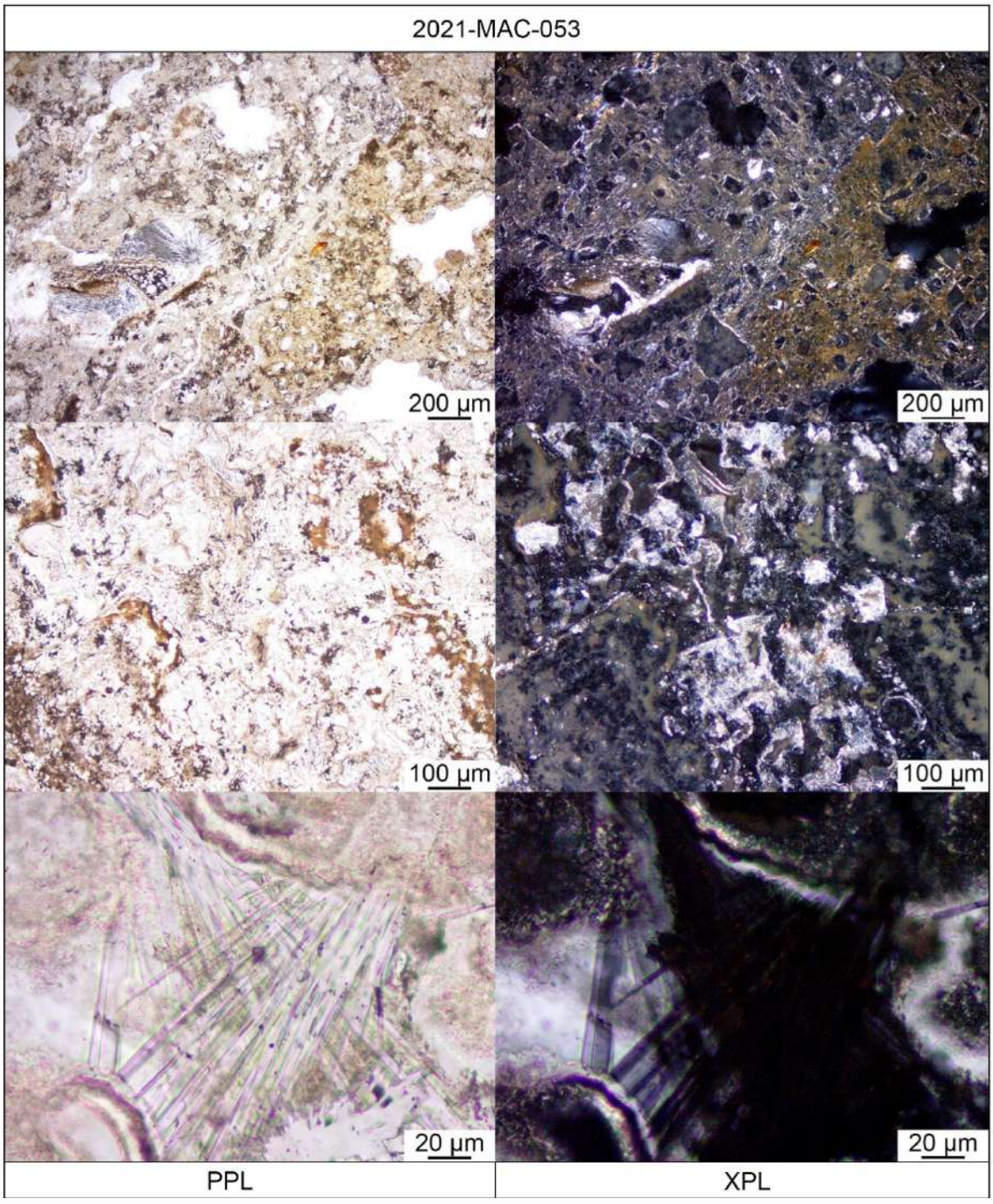

TEXTURAL DESCRIPTION:

The sample exhibits a brecciated texture composed of subrounded to angular clasts of volcanic glass. These clasts have been partially replaced by a fine-grained matrix of clays, silica, and zeolites, resulting in the appearance of volcanic glass "islands." The zeolites occur as radial acicular aggregates that infill cavities and interstitial spaces within the matrix.

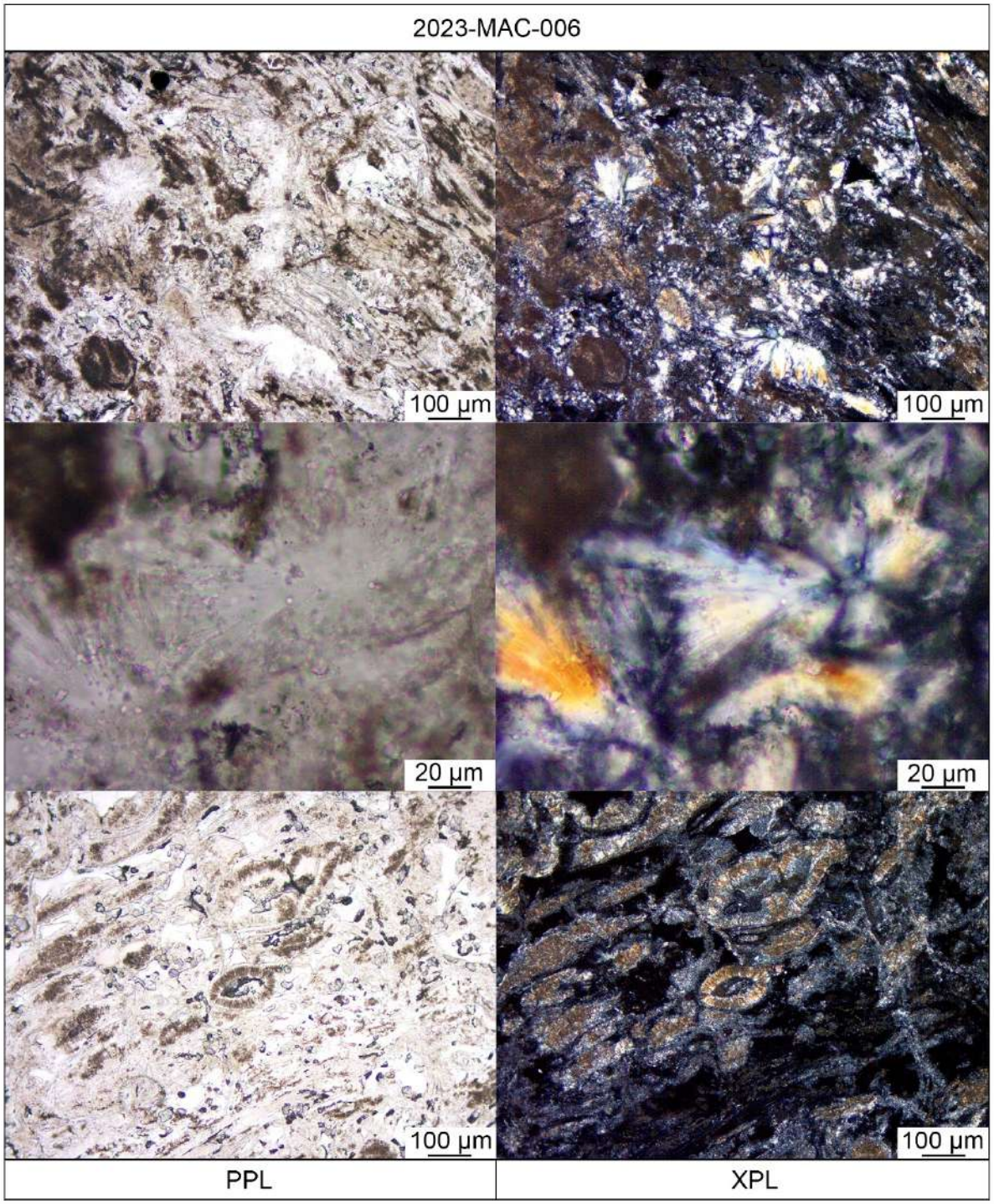

TEXTURAL DESCRIPTION:

The sample exhibits a brecciated texture composed of rounded to subangular clasts of volcanic glass embedded in a fine-grained matrix. Spherules of radiating zeolite show Brewster crosses.

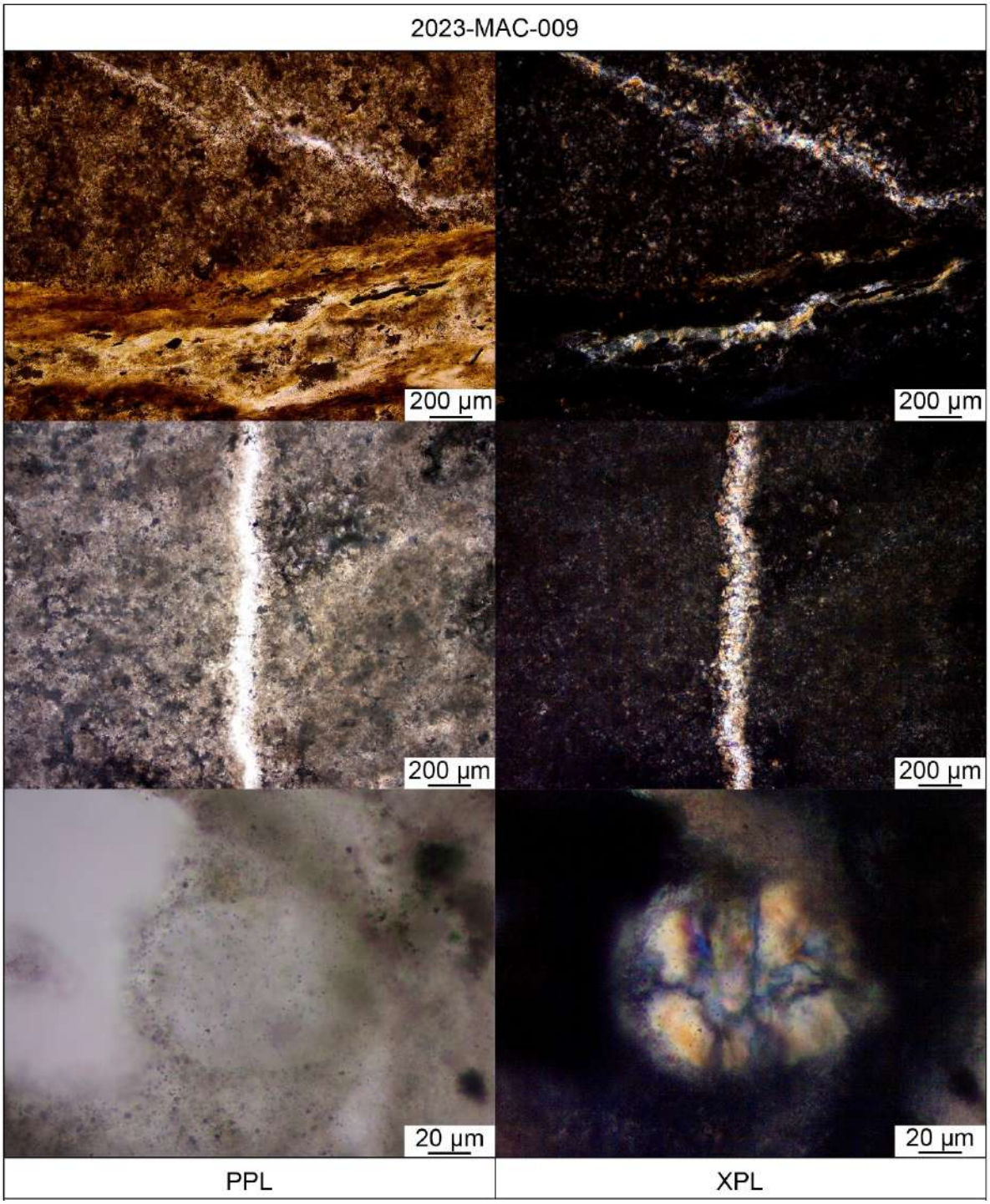

TEXTURAL DESCRIPTION:

The sample exhibits a brecciated texture. It presents irregular micro-veins regularly distributed throughout the altered matrix. These micro-veins are filled, in part, with subhedral zeolite radial aggregates.

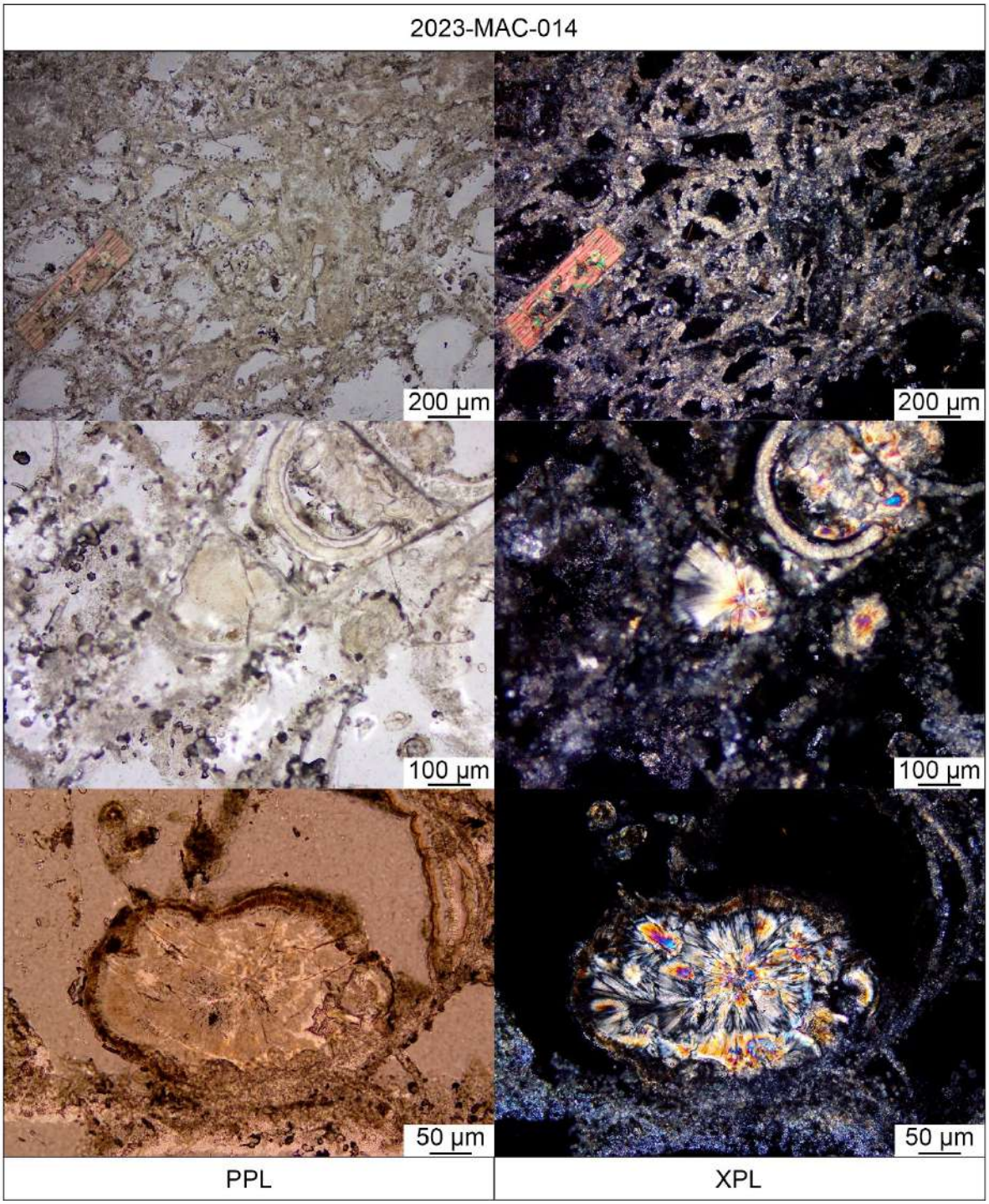

TEXTURAL DESCRIPTION:

The sample exhibits a brecciated texture composed of rounded to subangular clasts of volcanic glass embedded in a fine-grained groundmass of silica, clays, and zeolites. Small cavities (amygdales) within the matrix are filled with radial aggregates of zeolite crystals, and some show a rim of smectites. A subhedral mica crystal with a cariated outline is observed.

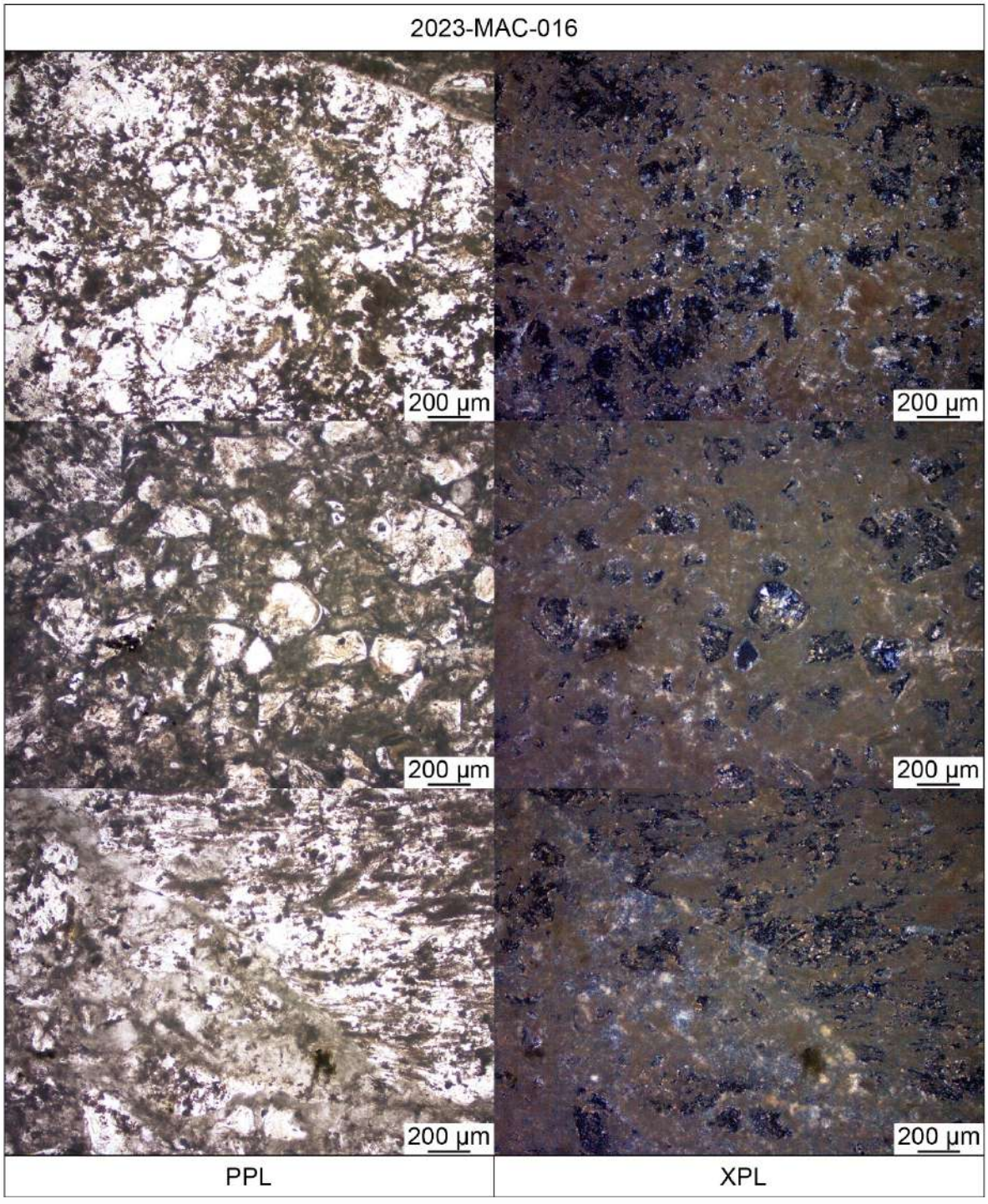

TEXTURAL DESCRIPTION:

The sample has a brecciated texture composed of subangular clasts embedded in a fine-grained groundmass. The matrix shows a high abundance of zeolites in some areas.

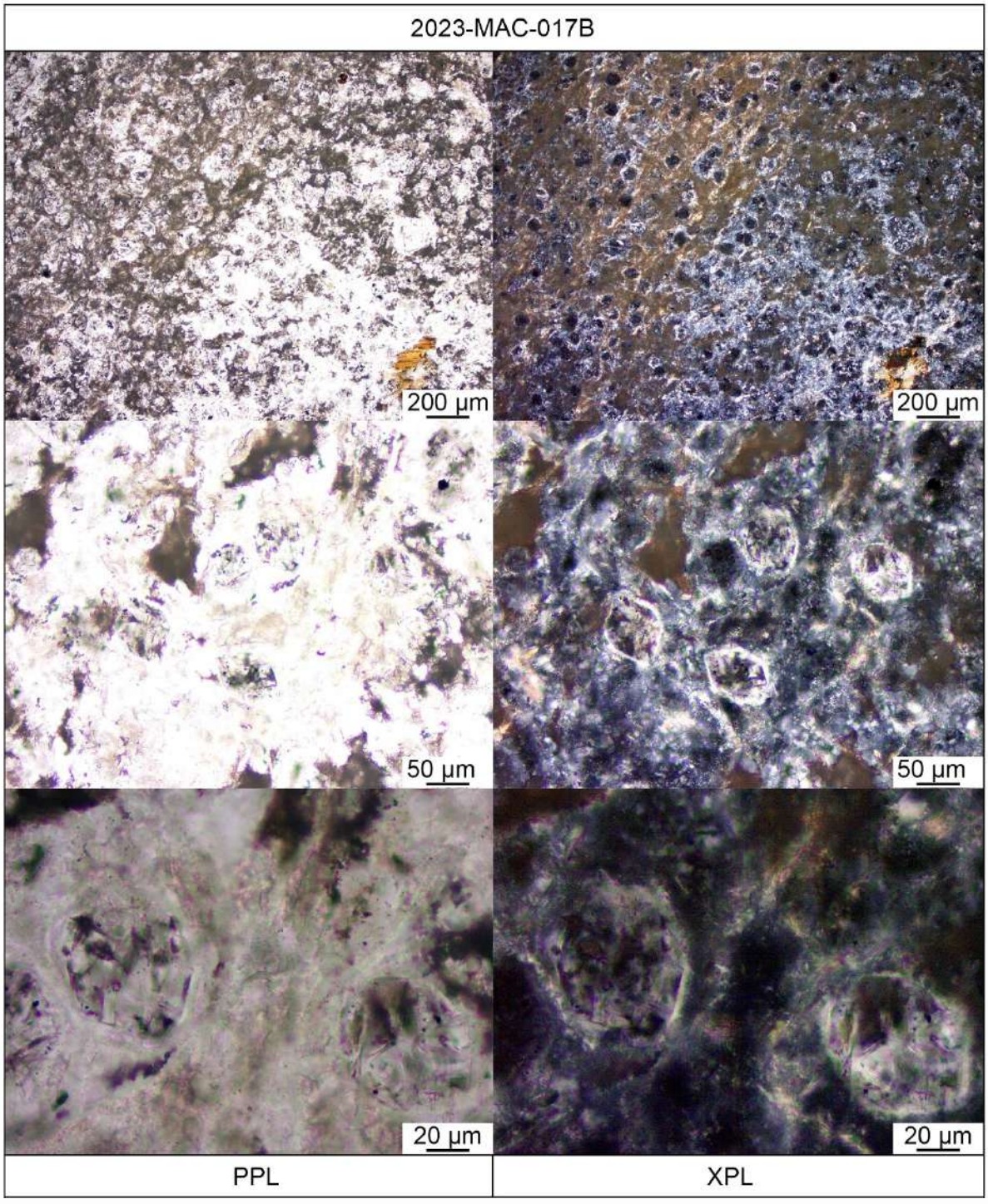

TEXTURAL DESCRIPTION:

The volcanic rock exhibits a brecciated texture. It comprises euhedral zeolite crystals displaying pseudo rhombododecahedra and pseudo trapezohedral faces. Anhedral mica crystals are also present.

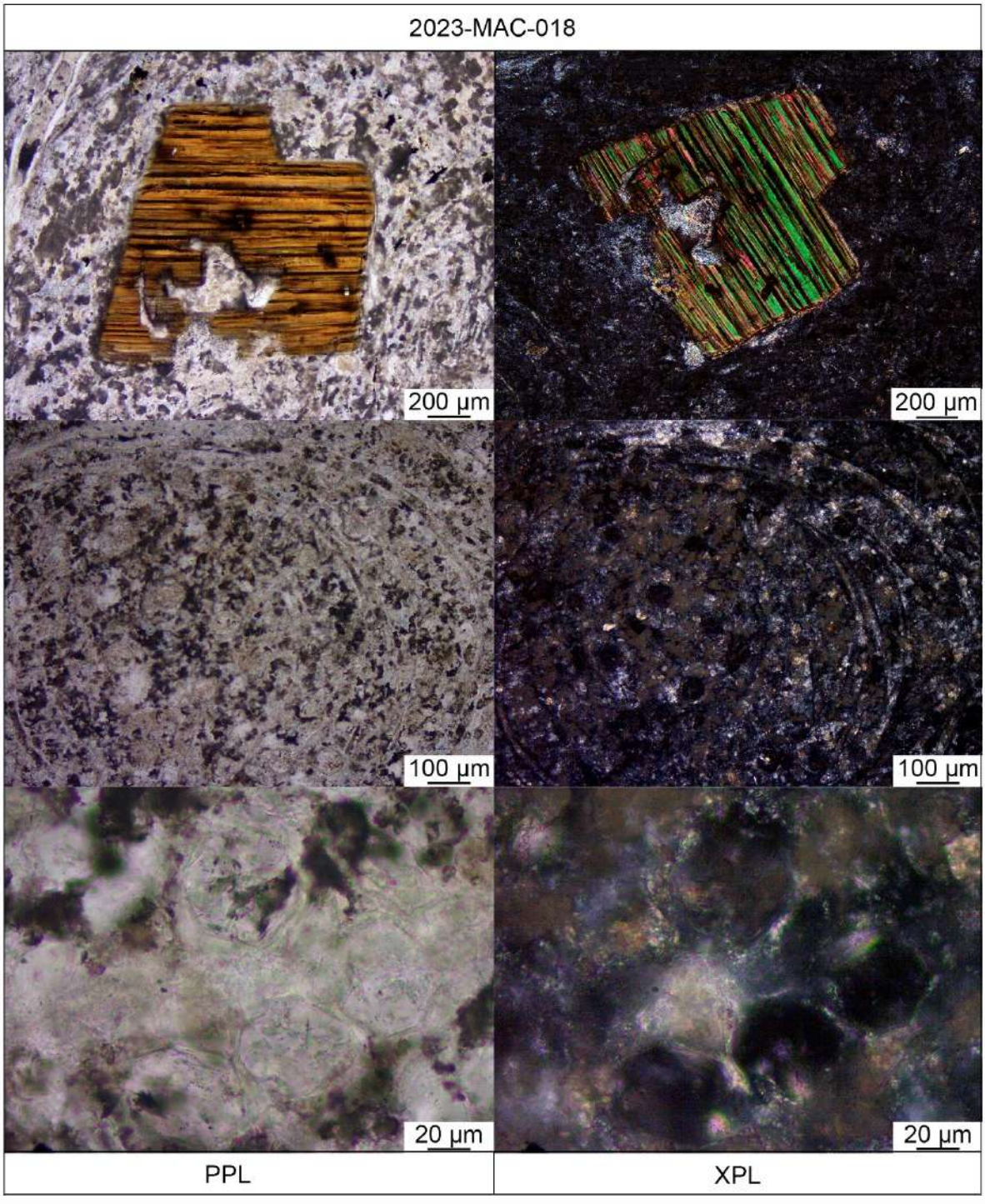

TEXTURAL DESCRIPTION:

The sample exhibits glass clasts with internal perlitic textures. The clasts are embedded in a fine-grained matrix composed of silica and clays. Possible idiomorphic pseudo rhombododecahedra zeolite crystals are observed occupying cavities in the matrix. Additionally, a subhedral mica crystal with a cariated outlines up to 0.5 mm in size are also present.

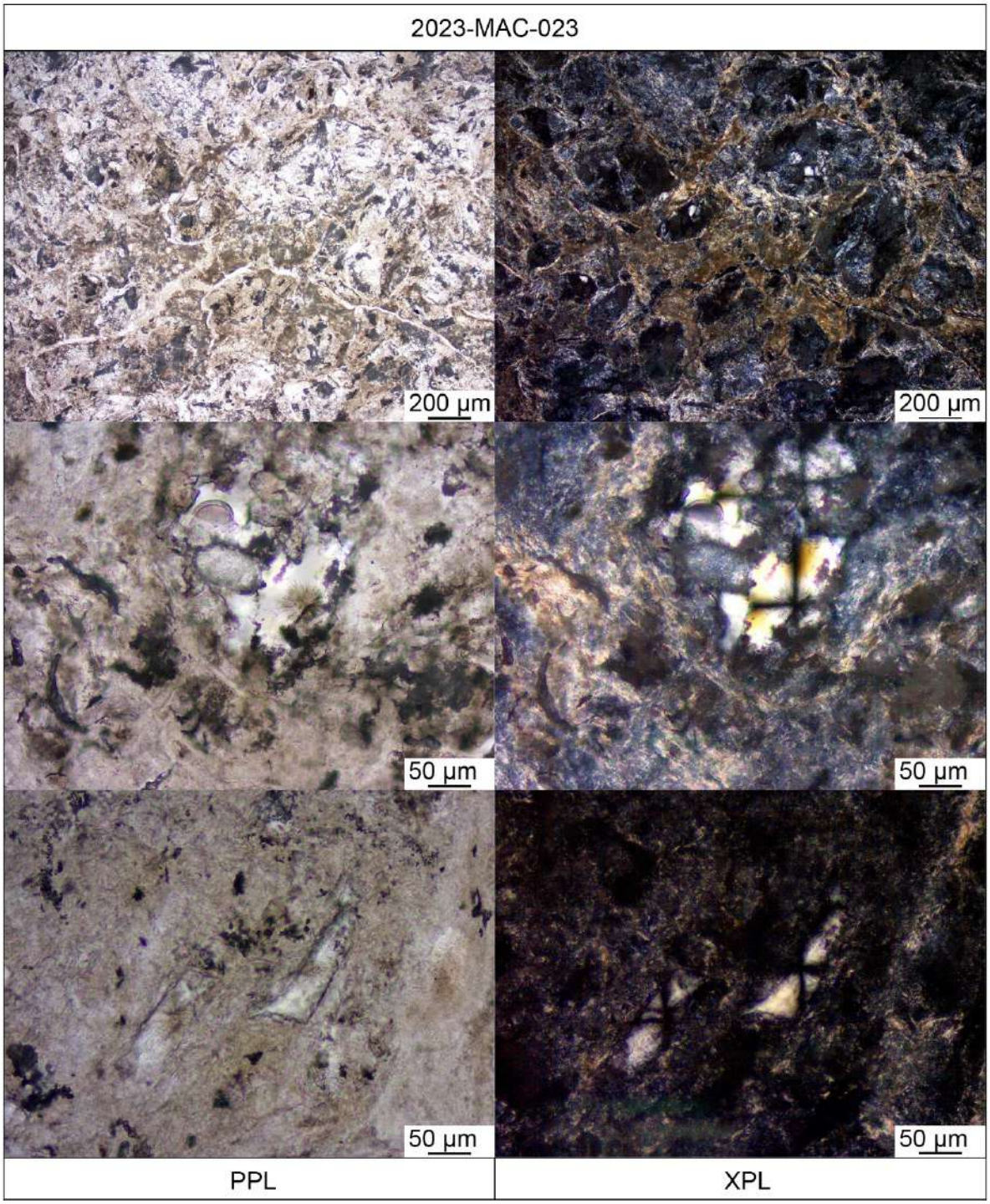

TEXTURAL DESCRIPTION:

The sample exhibits a conspicuous brecciated texture. The matrix is fine-grained and composed of silica, clays, and sparce brown micas. Spherules of radiating zeolite showing Brewster crosses are common. Isolated clasts of volcanic glass are preserved as relics, resulting from the progressive replacement of the original glass by zeolites.

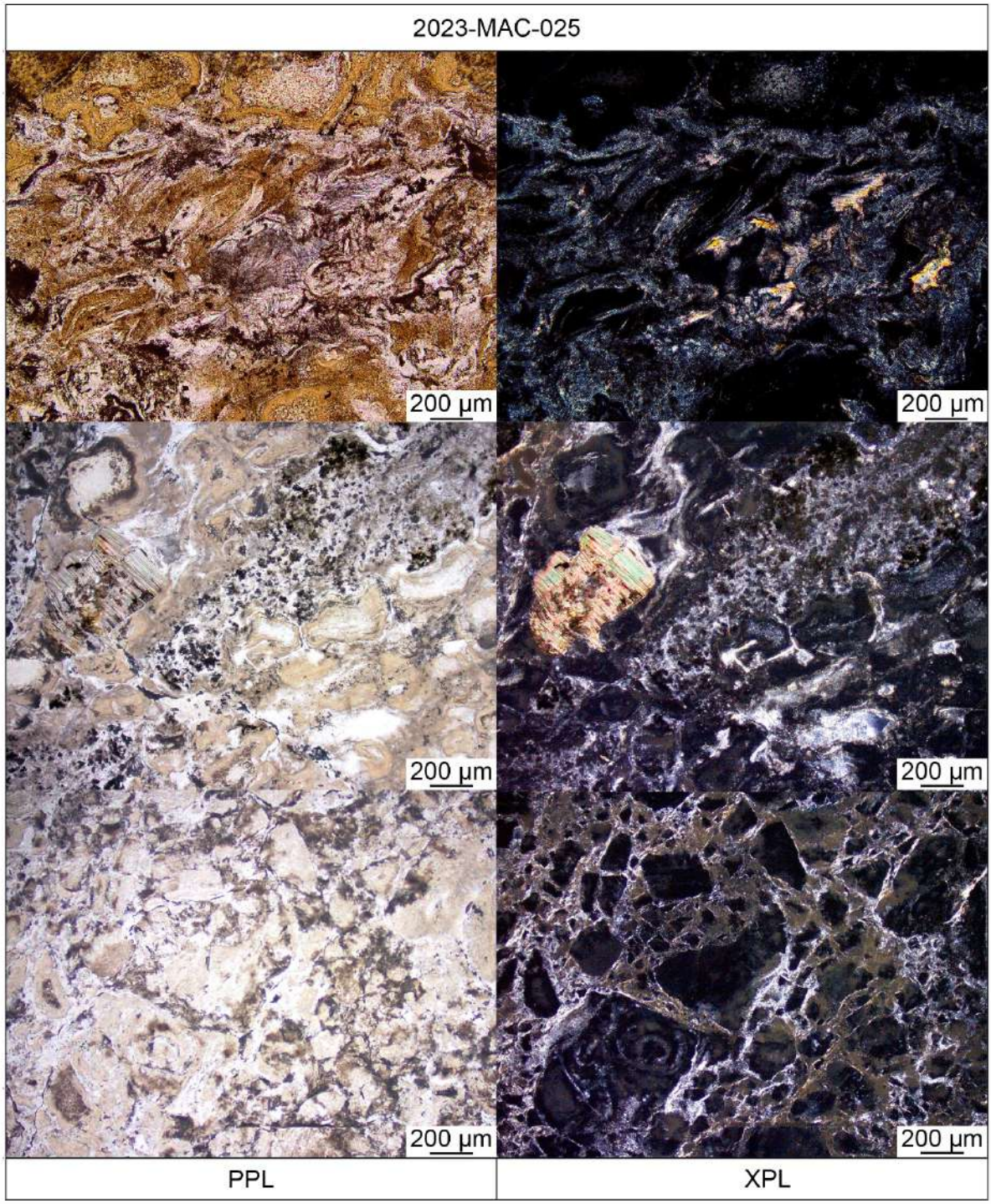

TEXTURAL DESCRIPTION:

The sample exhibits a brecciated texture composed of rounded to subrounded clasts, with some angular fragments. In some instances, volcanic glass clasts display concentric internal structures (perlitic texture) that were replaced by silica, clays, and zeolites. Euhedral to subhedral mica crystals are also present within the matrix and are variably altered to an Fe-rich, very fine-grained material, probably zeolites and clays.